



Technische Universität München
TUM School of Natural Sciences

Structural and functional characterization of GID/CTLH E3 ubiquitin ligases

Dawafuti Sherpa

Vollständiger Abdruck der von der TUM School of Natural Sciences der
Technischen Universität München zur Erlangung des akademischen
Grades einer **Doktorin der Naturwissenschaften (Dr. rer. nat.)**

genehmigten Dissertation.

Vorsitzender: Priv.-Doz. Dr. Gerd Gemmecker

Prüferinnen der Dissertation:

1. Hon.- Prof. Brenda A. Schulman, Ph.D.
2. Prof. Dr. Michael Sattler
3. Prof. Daniel Finley, Ph.D.

Die Dissertation wurde am 29.08.2022 bei der Technischen Universität
München eingereicht und durch die TUM School of Natural Sciences
am 30.11.2022 angenommen.

Acknowledgements

I am more than grateful to have joined the Schulman lab and scientifically, this has been the most enlightening time of my life so far. Brenda is the most enthusiastic and passionate mentor/scientist I have ever met, and I have always seen her keen and invested on everyone's progress in the lab. She has taught me valuable skills in science and life, immensely supported me throughout, and I am forever thankful for having her as my mentor. Even in years to come, I will cherish the memories of this lab.

I consider Bay 2 as my home-away-from-home and all the members of Bay 2 (including past members) bring joy in my work life. I am particularly thankful to have Jakub as my project partner and bench partner. I will definitely always remember all our night plunging sessions, our intense paper writing days, our everyday scientific coffee discussions, our scratching head moments and ultimate joyous successes.

Life as a Ph.D. student without Sepp and Rajan in the lab would be unimaginable. I am extremely thankful for everything they have done and taught me over the years. I also cannot think of the lab without Arno's coffee break and routine scientific and non-scientific discussions. Also, thank you Arno for all the mentoring and support. The biggest strength of our lab are the technicians and I am super thankful that they keep the lab running happily. Special thanks go to Susanne for taking care of insect cells of which I have ordered plenty, and the Susanne and Sabine in the kitchen for making our lab life easier.

I am lucky to have found colleagues like Khee, Basti, Kirby who are also amazing friends, who have constantly supported and guided me over the years. Thank you, guys for motivating me, keeping me updated and for keeping me sane. Also, I am happy to have received guidance and support from Randy and David in my early days in this lab. The Schulman lab members, including all who have come and gone over the last five years are very close to my heart, and it's been a super fun ride with you all! Additionally, I would also like to thank Khee, Christine, Arno, Ishi and Laura for giving me feedback on my thesis. I am also grateful to have amazing collaborators from the Mann Department (Ozge and Fynn), Sattler lab (Grzegorz) in TUM, Sidhu lab in University of Toronto. It was also an amazing learning experience to have very talented master students, Melissa and Max, during my Ph.D. Special thanks also to Gary for teaching and guidance with Michaelis-Menten kinetics. I am also thankful to Marianne for helping me with administrative work. The MPIB cryo EM facility managers Daniel Bollschweiler, Tillman Schäfer, similarly Jerome Basquin and the MPIB crystal facility team, and Stephan Ubel, Stefan Pettera from the MPIB biochemistry core facility have been an amazing support all these years.

None of this would have been possible without my family - my parents who gave their all and truly trusted me all the time; my siblings who gave me hope when there was none, joy when there was tears and motivation to challenge my limits when I was stuck. Without them my path in life would not have been this fun, adventurous and gratifying. **I love you guys!!!**

Table of contents

List of Publications	1
Abstract	2
1. Introduction	3
1.1. Protein degradation pathways	3
1.2. The ubiquitin system	4
1.3. E3 ligases and substrate recognition	5
1.4. GID/CTLH E3 ubiquitin ligase	7
1.5. Structural and functional composition of GID/CTLH subunits	8
1.5.1. The substrate receptors	8
1.5.2. The scaffolding subunits	9
1.5.3. The catalytic subunits	9
1.5.4. Additional subunits	10
1.6. Regulation by GID/CTLH E3 ligases	11
1.6.1. GID substrate regulation in yeast	11
1.6.2. Regulation by mammalian CTLH	12
1.6.3. Regulation by other CTLH	12
1.7. Aims of the study	13
2. Publications	14
2.1. GID E3 ligase supramolecular chelate assembly configures multipronged ubiquitin targeting of an oligomeric metabolic enzyme (Sherpa and Chrustowicz, et al. Molecular Cell. 2021)	14
2.2. Multifaceted N-degron recognition and ubiquitylation by GID/CTLH E3 ligases (Chrustowicz and Sherpa, et al. Journal of Molecular Biology. 2021)	44
3. Discussion	67
4. Methods	70
4.1. Cloning and plasmids preparation	70
4.2. Protein expression and purification for biochemistry and structural studies	70
4.3. Purification of endogenous yeast GID for cryo EM	71

4.4. Sortase mediated fluorescent labeling of substrates	71
4.5. ¹⁵ N labelling of hGID4 for NMR	72
4.6. In vitro biochemical assays with yeast GID complex	72
4.6.1. Multi-turnover ubiquitylation assays	72
4.6.2. Ubiquitin discharge assay	73
4.6.3. Competition assay	73
4.6.4. Assay for target lysine site determination	73
4.6.5. Determination of Michealis-Menten kinetics for Fbp1 ubiquitylation by GID E3	73
4.7. Size exclusion chromatography for characterization of GID complex assembly	74
4.8. Size exclusion chromatography-Multi angle light scattering (SEC-MALS)	74
4.9. Fbp1 enzyme activity assay	74
4.10. Fluorescence polarization (FP) assays	75
4.11. Peptide spot array binding assay	76
4.12. Isothermal titration calorimetry (ITC) binding assays	76
4.13. Yeast substrate degradation assays	76
4.14. Cryo EM sample preparation and data collection	77
4.14.1. Cryo EM data processing	78
4.14.2. Model building and refinement	78
4.15. X-ray crystallography and data processing	79
5. References	80

List of Publications

* Indicates equal contribution

Differential UBE2H-CTLH E2-E3 ubiquitylation modules regulate erythroid maturation, *eLife*, 2022

Dawafuti Sherpa*, Judith Müller*, Özge Karayel*, Peng Xu*, Yu Yao, Jakub Chrustowicz, Karthik V. Gottemukkala, Christine Baumann, Annette Gross, Oliver Czarnecki, Wei Zhang, Jun Gu, Johan Nilvebrant, Sachdev S. Sidhu, Peter J. Murray, Matthias Mann, Mitchell J. Weiss, Brenda A. Schulman, and Arno F. Alpi

Cryo-EM structures of Gid12-bound GID E3 reveal steric blockade as a mechanism inhibiting substrate ubiquitylation, *Nature Communications*, 2022

Shuai Qiao, Chia-Wei Lee*, **Dawafuti Sherpa***, Jakub Chrustowicz*, Jingdong Cheng, Maximilian Duennebacke, Barbara Steigenberger, Ozge Karayel, Tung Vu, Susanne von Gronau, Matthias Mann, Florian Wilfling, Brenda A. Schulman

A GID E3 ligase assembly ubiquitinates an Rsp5 E3 adaptor and regulates plasma membrane transporters, *EMBO Reports*, 2022

Christine R. Langlois, Viola Beier, Ozge Karayel, Jakub Chrustowicz, **Dawafuti Sherpa**, Matthias Mann, Brenda A. Schulman

How the ends signal the end: regulation by E3 ubiquitin ligases recognizing protein termini, *Molecular Cell*, 2022

Dawafuti Sherpa*, Jakub Chrustowicz*, Brenda A. Schulman

Multifaceted N-degron recognition and ubiquitylation by GID/CTLH E3 ligases, *Journal of Molecular Biology*, 2021

Jakub Chrustowicz*, **Dawafuti Sherpa***, Joan Teyra, Mun Siong Loke, Grzegorz Popowicz, Jerome Basquin, Michael Sattler, J. Rajan Prabu, Sachdev S. Sidhu, Brenda A. Schulman

GID E3 ligase supramolecular chelate assembly configures multipronged ubiquitin targeting of an oligomeric metabolic enzyme, *Molecular Cell*, 2021

Dawafuti Sherpa*, Jakub Chrustowicz*, Shuai Qiao, Christine R. Langlois, Laura A. Hehl, Karthik Varma Gottemukkala, Fynn M. Hansen, Ozge Karayel, Susanne von Gronau, J. Rajan Prabu, Matthias Mann, Arno F. Alpi, Brenda A. Schulman

Interconversion between Anticipatory and Active GID E3 Ubiquitin Ligase Conformations via Metabolically Driven Substrate Receptor Assembly, *Molecular Cell*

Shuai Qiao, Christine R. Langlois*, Jakub Chrustowicz*, **Dawafuti Sherpa***, Ozge Karayel, Fynn M. Hansen, Viola Beier, Susanne von Gronau, Daniel Bollschweiler, Tillman Schäfer, Arno F. Alpi, Matthias Mann, J. Rajan Prabu, Brenda A. Schulman

Abstract

Proteins are constantly turned over in the crowded cellular milieu to maintain homeostasis. One crucial factor that plays a role in maintaining protein quality control is the protein degradation machinery such as the ubiquitin-proteasome system (UPS). The major players in this system are the E3 ubiquitin ligases that rely on a cascade of E1 (ubiquitin-activating) and E2 (ubiquitin-conjugating) enzymes to specifically and efficiently target diverse proteins for ubiquitylation, regulating nearly all biological processes. We know very little of how E3 ubiquitin ligases are configured to match various protein features including different folds, oligomeric states and post-translational modifications. By studying the GID/CTLH E3 ligase, we answer some of these fundamental questions. We discovered that the GID complex employs a higher-order assembly mechanism as a strategy for efficiently targeting one of its oligomeric substrates, the tetrameric gluconeogenic enzyme Fbp1. Additionally, we elucidated how the pliable nature of the substrate receptors of GID complex allows for a variety of substrate degrons to bind. Moreover, we show that these structural and biochemical features are conserved in its human ortholog, the CTLH complex.

Zusammenfassung

Proteine müssen in dem überfüllten zellulären Milieu ständig umgewandelt werden, um die Homöostase aufrechtzuerhalten. Ein entscheidender Faktor, der bei der Aufrechterhaltung der Qualitätskontrolle von Proteinen eine Rolle spielt, ist die Maschinerie für den Proteinabbau wie das Ubiquitin-Proteasom-System (UPS). Die wichtigsten Akteure in diesem System sind die E3 Ubiquitinligasen, die sich auf eine Kaskade von E1 (Ubiquitin-aktivierenden) und E2 (Ubiquitin-konjugierenden) Enzymen stützen, um verschiedene Proteine, die nahezu alle biologischen Prozesse regulieren, spezifisch und effizient zur Ubiquitylierung auszuwählen. Wir wissen nur sehr wenig darüber, wie E3 Ubiquitinligasen konfiguriert sind, um verschiedenen Proteineigenschaften zu entsprechen, einschließlich verschiedener Faltungen, oligomeren Zustände und posttranslationaler Modifikationen. Durch die Untersuchung der GID/CTLH E3 Ligasen können wir einige dieser grundlegenden Fragen beantworten. Wir entdeckten, dass der GID-Komplex einen Mechanismus höherer Ordnung für den Zusammenbau einsetzt, um eines seiner oligomeren Substrate, das tetramerische glukoneogene Enzym Fbp1, effizient anzusprechen. Darüber hinaus konnten wir aufklären, wie die flexible Natur der Substratrezeptoren des GID-Komplexes die Bindung einer Vielzahl von Substrat-Degronen ermöglicht. Darüber hinaus zeigen wir, dass diese strukturellen und biochemischen Merkmale in seinem menschlichen Ortholog, dem CTLH-Komplex, konserviert sind.

1. Introduction

Cellular information in all living organisms flows from nucleic acids to proteins, as stated by the central dogma, through biological processes of transcription and translation. The end product of this process - proteins - can be extremely diverse in their structural and functional aspects. Additional protein modifications occur either during or after the process of ribosomal protein translation. The translation process itself is facilitated by many other proteins that function as enzymes, working in coordination with the ribosomes to decorate these proteins with their signature features. Proteins, which are the main workhorses of the cell, execute majority of cellular functions and maintain metabolic pathways to keep the cellular factory running. Moreover, they also serve as chromatin remodelers and transcriptional regulators [1], thus impacting every part of the cellular system.

The functional diversity in proteins is derived from their distinct folds, various oligomeric states, and through different post-translational modifications (PTMs) that they inherit during or after translation. Although the number of proteins in human compared to other organisms such as drosophila or mice is not extremely different, humans possess higher complexity in the cellular and organismal level functionalities. Several factors like multiple splicing variants of mRNA or the distinct PTMs that act as a signal for activating or repressing numerous cellular processes additionally supplement diversity to the protein families. Furthermore, constant protein turnover is crucial for maintaining metabolic regulation, and disturbances in this process due to environmental change or stress can be detrimental. Cells have multiple levels of protein quality control including i) factors responsible for proper protein synthesis via ribosomes and its associated proteins [2], ii) systems ensuring its proper folding and translocation at the right cellular compartments [3, 4] iii) degradation machineries such as the autophagy-lysosomal system and ubiquitin-proteasome system (UPS) for removal of unnecessary or surplus proteins [5-8].

1.1. Protein degradation pathways

The earliest described protein degradation pathway involves the autophagy-lysosomal degradation, observed upon nutritional deprivation, to degrade endocytosed proteins. Autophagy encompasses not only removal of misfolded or aggregated proteins but also removal of whole organelles and intracellular pathogens to maintain cellular homeostasis. Key players of this pathway are the evolutionarily conserved ATG (Autophagy Related Gene) and related family of proteins, which are involved in formation of double-membrane autophagosome leading to lysosomal fusion and degradation of autophagic contents [9].

In addition, there are non-lysosomal ATP-dependent proteolytic pathway whose existence was first noted in late 1970s, where they first characterized the function of a 76 amino acid protein ubiquitin (previously named APF1 for ATP-dependent protein activation factor-1) in rabbit reticulocytes [10-12]. Biochemical studies led by Hershko, Ciechanover and Varshavsky during 1970s and 1980s led to not only the discovery of ubiquitin but also the first components of ubiquitin transfer machineries [13]. Consecutively, 26S proteasome was discovered as the proteolytic factor responsible for degrading the ubiquitin conjugated proteins [14, 15]. Seminal works from several scientists led to discovery of the first genes of ubiquitin system [16-19], to discovery of the first degradation signals [20] and identification of the first physiological

substrates of the ubiquitin system [21] and this was progressively followed up by many others over the years, thereby establishing the involvement of ubiquitin biology in nearly all cellular pathways including cell cycle, DNA repair, protein synthesis, transcriptional regulation and stress responses [22].

1.2. The ubiquitin system

Ubiquitin is encoded by 4 different genes in yeasts (UBI1-3 are produced as fusion to ribosomal proteins and UBI4 as polyubiquitin cassette) [19], and in higher eukaryotes it is produced either as a fusion to ribosomal proteins (encoded by UBA52 and RPS27A) or as polyubiquitin cassettes (encoded by UBB or UBC) [23]. Ubiquitin conjugation happens majorly on a lysine residue of protein substrates, but there is increasing evidence that its transfer can also occur on other substrate residues like serine, cysteine or even onto other molecules such as lipids and sugars [24]. Moreover, ubiquitin can be linked via its C-terminus to the amino terminus (N-terminal Met1) or to any of the seven lysines (K6, K11, K23, K29, K33, K48, K63) of another ubiquitin molecule contributing to various homotypic or heterotypic ubiquitin chains. Each ubiquitin chain type and pattern together form the ubiquitin code, eliciting specific downstream proteolytic and non-proteolytic pathways [25]. Furthermore, ubiquitin can itself be modified by PTMs like phosphorylation, acetylation, phosphoribosylation and glutamine deamidation for regulating downstream signaling pathways [26].

Ubiquitin transfer is catalyzed in three main steps (Fig. 1) – First, the ATP/ magnesium ion dependent step of ubiquitin transfer to E1 (ubiquitin-activating enzyme) takes place by formation of a ubiquitin-AMP adduct followed by subsequent transfer of ubiquitin, whereby its C-terminal glycine forms a covalent thioester bond with the E1's catalytic cysteine. In human, there are 2 E1s (UBA1 and its homologue UBA6, which is only specific for a few E2s). Second, ubiquitin is transferred to the catalytic cysteine of the E2 (ubiquitin-conjugating enzyme) by a transthioylation reaction forming a new thioester bond between the C-terminal glycine of ubiquitin and the catalytic cysteine of the E2 – more than 40 E2s exist in human. Third step of ubiquitin transfer involves the E3 ubiquitin ligase, which catalyzes both substrate recruitment and ubiquitin transfer from the E2's catalytic cysteine to the substrate, thus catalyzing the formation of an isopeptide bond between the C-terminus of ubiquitin and the ϵ -amino group of the substrate lysine or a terminal amino group of the substrate – more than 600 E3s exist in human. Moreover, there are deubiquitylating enzymes (DUBs) acting as opposing elements that catalyze the ubiquitin cleavage, and other proteins harboring ubiquitin recognition domains for further regulation. In addition, there are other significant players involved in the protein degradation pathway that function downstream of the ubiquitin transfer system - Cdc48/p97 system with its cofactors that extract and unfold the polyubiquitinated proteins when necessary, and the giant proteolytic hub - “the proteasome” with its associated proteins that ultimately degrade polyubiquitinated substrates. Over the years exemplary papers illustrating the details of the ubiquitin system have evolved. These include studies elucidating ubiquitin transfer through the individual steps of E1-E2-E3 cascade [27-30], ubiquitin transfer from E3s onto substrates [31, 32], ubiquitin recognition by DUBs [33-35], polyubiquitin extraction by Cdc48 and proteasomal recognition of polyubiquitylated substrates [36-40], all of which allow us to gaze into possibly more accurate pictures of these complex processes.

HECT E3 ligase members have a unique feature of first transferring ubiquitin from the E2 catalytic cysteine to the E3 catalytic cysteine via a transthioylation reaction to form a thioester intermediate followed by ubiquitin transfer on to the substrate. There are nearly 30 HECT E3 ligases and they all have a characteristic N-terminal substrate binding domain and a C-terminal HECT domain, which is composed of an N-terminal lobe that binds E2~Ub and a C-terminal lobe that harbors the catalytic cysteine [54]. Unlike RING E3s where the E2 determines ubiquitin chain specificity, the HECT domain of the HECT E3s determines the chain type to allow processive polyubiquitination. Recent structures of the full-length HECT E3s, such as HUWE1, have provided some glimpses of multiple open and closed conformations, and added to our understanding of its substrate recruitment and how regulation by HECT E3 occurs [55].

RBR E3 ligases which are a hybrid of both RING and HECT E3s encompass two predicted RING finger domains, RING1 and RING2 (also called Rcat), and an in-between RING (IBR) domain that binds zinc. There are 10 or more RBR E3s known so far. Most RBRs are autoinhibited on their own and need to undergo conformational changes for activation [56]. The most well characterized members of this family of E3 ligases include PARKIN, LUBAC, and Ariadne family RBRs.

Although there is constant turnover of the cellular proteome, we have superfluous proteins in the cell compared to the E3 ligases that can ubiquitylate them. How do these limited number of E3 ligases target the vast proteome remains a major question in the field. E3s have attained various strategies to tackle this problem. These include using multiple interchangeable substrate receptors, or forming diverse assemblies ranging from multi-subunit higher order assemblies to cooperative E3-E3 assemblies (Fig. 2) [57-60]. There are specific sequences or structural features within the substrate that are recognized by the substrate binding domains or subunits of the E3s. Distinct domain folds like the UBR-box, beta-barrel, beta propeller or helical repeats have been evolved within the E3 ligases to selectively recognize distinct substrate features [8]. Each substrate receptor or substrate-binding domain specifically recognizes a motif, or so-called a "degron" (for degradation signals) within the substrate. These degrons are usually short linear sequence motifs that are disordered. In some cases, degrons can be ordered regions with characteristic 3-dimensional folds and sometimes they are further decorated with PTMs for recognition. Furthermore, they are categorized into terminal degrons, those that are occurring or proteolytically-generated at the N- or C- terminus, or internal degrons, those residing in the internal protein sequence. The pioneering studies from Varshavsky and colleagues over years have thoroughly defined the landscape of N-terminal degrons [20, 61, 62]. So far, all 20 amino acid residues have been classified into specific degron group following their recognition through Arg/N-degron, Ac/N-degron, Pro/N-degron, Gly/N-degron, fMet/N-degron pathways. Moreover, the recent discoveries of the C-degron pathways have greatly expanded the field of terminal degronome [63].

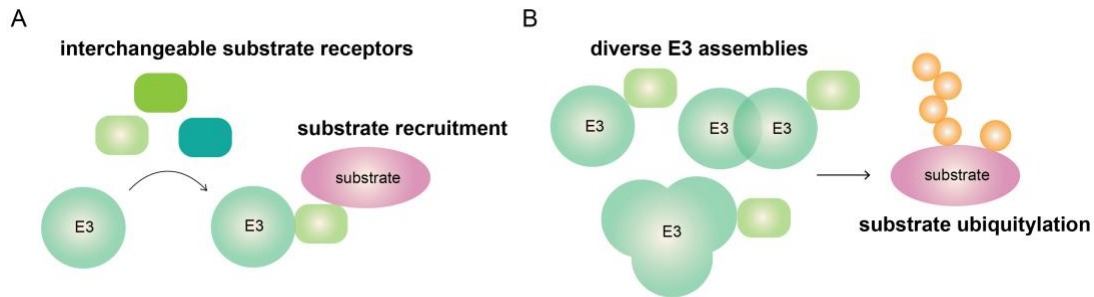


Figure 2. Strategies of E3 ligases for diverse substrate targeting.

(A) Some E3 ligases can allow binding of multiple swappable substrate receptors to bind variety of substrate degrons, and/or (B) form diverse mono, di or multi-meric assemblies to catalyze substrate ubiquitylation.

1.4. GID/CTLH E3 ubiquitin ligase

Many substrates of E3 ligases include metabolic enzymes which are oligomeric by nature. However, the regulation of these oligomeric metabolic enzymes by ubiquitylation machineries are not well studied. One of the early identified homotetrameric metabolic enzyme is the budding yeast fructose-1,6-bisphosphatase (Fbp1), which is involved in the glycolysis and gluconeogenic pathways. The yeast Fbp1 is the first identified target of a glucose-dependent, catabolite inactivation process in eukaryotes [64]. When yeasts are switched from carbon-starved to carbon-rich conditions, the gluconeogenic process is impeded through processes that terminate Fbp1 synthesis and activity. This also induces ubiquitin-mediated degradation of Fbp1 by the GID (Glucose-Induced Degradation deficient) E3 ligase [65]. Depending on the length of starvation, Fbp1 degradation in yeast can occur in either the proteasome (for up to 24 hours starvation) or the vacuole (for 1-3 days of starvation) [64-68]. Thus, early GID genes were also named as “VID” for vacuolar import and degradation. Numerous studies from the group of Dieter Wolf identified components of the multi-subunit GID E3 ligase complex which targets gluconeogenic enzymes for proteasomal degradation following glucose replenishment [65, 67-69]. Later studies have suggested that the function of GID is not limited to only regulation of glucose metabolism but it also acts as a responsive system during different environmental stresses [70-74]. All components of the yeast GID complex are evolutionarily conserved in higher eukaryotes including drosophila, and mammals, where they are known by the nomenclature “CTLH”, named so due to the presence of multiple CTLH (C-terminal to LisH) domain-containing subunits (Fig. 3) [75-77]. Unlike its yeast ortholog, the mammalian CTLH E3 does not target any gluconeogenic enzymes, rather it has been linked to crucial biological processes such as erythropoiesis, embryogenesis, metabolism, cell division [78].

A

Yeast GID	Human CTLH	Functional modules
Gid1	RANBP9/RANBP10	substrate-receptor scaffolding subunits (SRS)
Gid8	TWA1	
Gid5	ARMC8	
Gid4/10/11	hGid4	substrate-receptor
Gid2	RMND5A/5B	catalytic subunits (CAT)
Gid9	MAEA	
Gid7	WDR26, MKLN1	
moh1	YPEL5	
Gid12	-	

Figure 3. The GID and CTLH E3 ligase subunits.

(A) Majority of the yeast GID subunits are evolutionarily conserved in humans, where they collectively form the CTLH complex.

1.5. Structural and functional composition of GID/CTLH subunits

1.5.1. The substrate receptors

The minimal active core of the GID/CTLH E3 entails a catalytic module and a substrate receptor scaffolding (SRS) module, and in yeast GID, the SRS module accommodates multiple stress-induced interchangeable substrate receptors (Fig. 4) [74]. The first identified substrate recognition component of GID is Gid4, which is specifically upregulated during recovery from glucose starvation [68, 79]. Gid4 recognizes N-terminal proline together with a few downstream residues in the gluconeogenic substrates of GID, thus following the Pro/N-degron pathway (Fig. 4A) [79]. In addition, distinct environmental perturbations, such as heat shock, osmotic stress, as well as carbon, nitrogen, and amino acid starvation induce expression of two other GID substrate receptors – Gid10 and Gid11 (Fig. 4B and 4C) [71, 73, 74]. Gid10 recognizes Pro/N-degron substrate Art2 [80], and Gid11 recognizes substrates with N-terminal threonine [71]. These discoveries of novel substrate receptors and their extended specificity significantly widen the realm of potential GID substrates.

The molecular basis of N-degron recognition by GID/CTLH E3 was revealed from several crystal structures of human Gid4 (hGid4) and yeast Gid10 bound to various Pro/N- and non-Pro/N-peptides [80-84]. Both Gid4 and Gid10 adopt an 8-stranded anti-parallel β -barrel fold with a deep degron-binding tunnel harboring flexible loops at its entrance that establish contacts with the downstream degron residues [81]. Unlike Gid4 and Gid10, the newly identified Gid11 is a predicted seven-bladed β -propeller but the mechanistic details of its interaction with the GID complex and its substrate degrons remain to be determined. Interestingly, fly [85] and human CTLH E3s [86] have been implicated to target substrates lacking Pro/N-degrons through Gid4-independent mechanism, raising the possibility for existence of additional substrate receptors and other non-proline/N-substrate degrons of GID/CTLH.


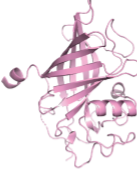
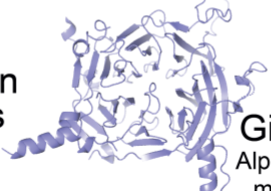
	induction condition	substrate receptor	substrates	degron type
A	glucose recovery	 Gid4 PDB:7NS3	Fbp1 Mdh2 Icl1 Pck1	Pro/N-degron
B	heat/osmotic stress/nitrogen starvation	 Gid10 PDB:7QQY	Art2	Pro/N-degron
C	ethanol starvation and other stress conditions	 Gid11 AlphaFold model	Phm8 Gpm3 Yor283w Cpa1 Blm10	Thr/N-degron

Figure 4. Regulation by substrate receptors of the GID E3 ligase.

The expression of the three substrate receptors of GID, Gid4, Gid10 and Gid11, rely on the environmental stimuli. (A) Gid4 is upregulated during glucose recovery to target Pro/N-degron gluconeogenic substrates; (B) Gid10 is upregulated during heat, osmotic shock or nitrogen starvation conditions to target Pro/N-degron substrate Art2; (C) Gid11 is upregulated during ethanol starvation and other environmental stresses targets Thr/N-degron substrates.

1.5.2. The scaffolding subunits

GID core scaffold consist of subunits Gid1-Gid5-Gid8 in yeast which correspond to RanBP9/10-ARMC8a-TWA1 in human CTLH [74]. Gid1 (RANBP9/10) and Gid8(TWA1) have the characteristic LisH, CTLH, CRA motifs. In human, there are two paralogous subunits of Gid1 – RANBP9 and RANBP10, which have minor differences at the N-terminus. RANBP9 has poly-proline and polyglutamine rich sequences at the N-terminus whereas RANBP10 has a much shorter N-terminus without these sequence repeats. Additionally, Gid1(RANBP9/RANBP10) have the SPRY domain with its characteristic two antiparallel beta sheets and helical segments at each end. Gid8(TWA1) is a small protein acting as a crucial scaffolding hub that connects multiple Gid subunits. Gid5(ARMC8) is the only scaffolding protein that lacks LisH-CTLH-CRA motifs but instead forms a super helical structure of armadillo repeats engaging Gid1(RANBP9/RANBP10), Gid8(TWA1) and the substrate receptor Gid4 (hGid4)/Gid10/Gid11 [71, 74]. In human, there are two isoforms of ARMC8 known in literature - ARMC8 α , which is the full-length form that binds Gid4, and the shorter ARMC8 β , which does not have the hGid4 binding interface but still can stably bind other CTLH subunits.

1.5.3. The catalytic subunits

The catalytic module of the GID/CTLH is composed of heterodimeric Gid2 (RMND5A) and Gid9 (MAEA) subunits that are intricately intertwined forming a T-shaped structure [69, 74].

Gid2 (RMND5A), the active RING subunit and Gid9 (MAEA), accessory RING-like subunit function similarly to other heterodimeric RING E3s such as BRCA1/BARD1. Unlike the canonical RING domains which have two zinc ions coordinated by cysteine and histidine residues in a cross-braced manner, GID has degenerated RING domains [69].

The RING domain of GID/CTLH binds its E2 conjugating partner - Ubc8 (UBE2H), also annotated as Gid3 in yeast, which catalyzes K11 and K48 linked ubiquitin chain formation on the substrates [74, 87]. Ubc8 (UBE2H) possess a highly acidic and serine rich C-terminus similar to yeast CDC34 pointing perhaps towards a potential function of this tail [88]. Moreover, other promiscuous E2 like UBE2D2 has been shown to work with GID/CTLH to ubiquitylate substrates *in vitro* [89].

1.5.4. Additional subunits

Gid7 is a WD40-repeat containing subunit, which forms a seven-bladed beta-propeller domain. Despite lack of structural and functional characterization of yeast Gid7 in the past, it was known that it is required for degradation of the gluconeogenic substrate Fbp1 [65, 67, 68]. In human, two orthologues of Gid7 have been proposed - WDR26, whose domain architecture is analogous to Gid7, and MKLN1, which has instead a six-bladed kelch-repeat domain [76, 77]. Additionally, MKLN1 also has a discoidin domain at the N-terminus. The discoidin domain can bind proteins, lipids, galactose and collagen, but its interactors in association with the CTLH complex is yet known [90]. Many kelch- and WD40-repeat containing domains are known to facilitate protein-protein interactions but this still needs to be explored for GID/CTLH E3. WDR26, however, has been recently proposed as a substrate receptor for targeting Hbp1 in human [86], although this still requires further validation.

There are also other proteins associated with GID/CTLH E3 that are not so well studied. One such protein is moh1 (YPEL5) [91]. YPEL5 is a very small protein whose function in human CTLH complex is so far not known. It has a predicted zinc-finger-like metal binding domain and has been shown to localize in centrosome and nucleolus suggesting potential function during cell division.

Another subunit, IFP1(also called YDL176W or Gid12) in yeast was recently shown to interact with Gid4 and Gid5 with an extended interface, thus remodeling the substrate binding pocket of Gid4 [92]. Gid12 is a seven-bladed β -propeller with a large hydrophobic surface on one side that interacts with Gid4. It also sterically blocks the ubiquitylation of target lysines on the oligomeric gluconeogenic substrates and the effect is most notable for Fbp1 in the context of Gid7-bound Chelator-GID complex. High throughput screening studies have linked Gid12 with actin patch formation during endocytosis [93], but whether this is related to GID function needs to be determined. Moreover, the ortholog of this yeast subunit in human is not known, yet it is likely that such a modulator of human CTLH perhaps could exist.

1.6. Regulation by GID/CTLH E3 ligases

1.6.1. GID substrate regulation in yeast

GID substrate regulation is most well studied in yeast. Although Fbp1 was the first identified substrate of GID, all the gluconeogenic substrates including malate dehydrogenase (Mdh2), isocitrate lyase (Icl1) and (phosphoenolpyruvate carboxykinase) Pck1 rely on GID for their degradation. Under carbon starvation conditions, a core but inactive multiprotein complex is assembled, which is composed of scaffolding subunits *Gid1*, *Gid5* and *Gid8*, and catalytic subunits *Gid2* and *Gid9* (Fig. 5) [74]. A switch from gluconeogenic to glycolytic conditions triggers production of the substrate receptor *Gid4* [68, 94], which then assembles with the inactive GID to form GID^{SR4} (SR stands for substrate receptor) complex that contains all the fundamental elements of a functional E3 ligase (Fig. 5). The substrate receptor *Gid4* recruits the gluconeogenic substrates via their N-terminal Pro/N-degrons for ubiquitylation [79, 84, 95]. Although for other gluconeogenic enzymes the Pro/N degrons are exposed upon cleavage of N-terminal Met1 by methionine aminopeptidases, *Pck1* requires additional action of another aminopeptidase, *Icp55*, to trim the N-terminal Ser2 [96]. Following the substrate binding and ubiquitylation, the substrate receptor *Gid4* also gets ubiquitylated and rapidly degraded [94]. Ubiquitin transfer is catalyzed by *Gid2*-*Gid9*, which together activate the cognate *Ubc8*-ubiquitin intermediate [87]. Although substrates like *Mdh2* are rapidly ubiquitylated by GID^{SR4}, *Fbp1* degradation *in vivo* depends on another protein, *Gid7* [65]. Furthermore, following ubiquitylation, ubiquitylated *Fbp1* requires *Cdc48* and its cofactors *Ufd1*-*Npl4* for degradation [97], potentially indication their function upstream of the proteasome for extracting and unfolding the ubiquitylated substrates (Fig. 5).

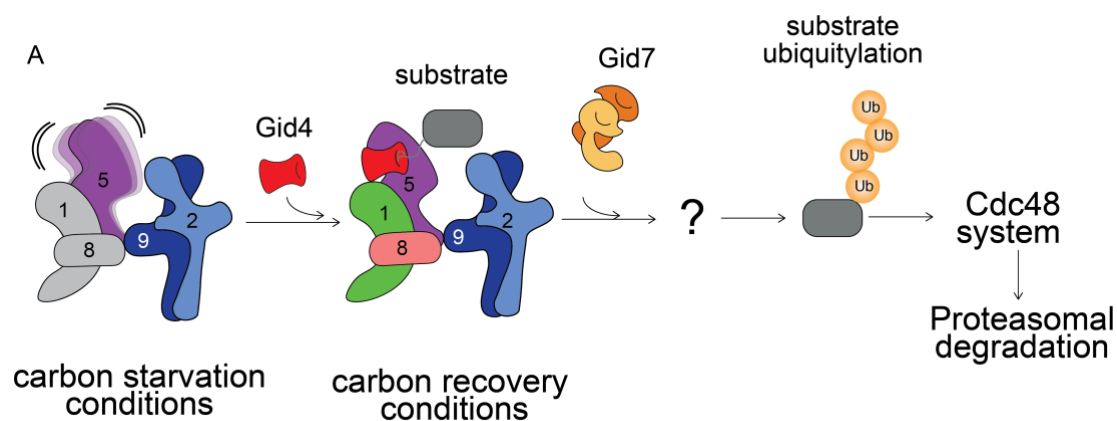


Figure 5. Regulation of gluconeogenic enzymes by the GID E3 ligase.

*(A) In yeast, substrate receptor *Gid4* is induced upon switch from carbon starvation to carbon recovery conditions. This activates the complex to bind different gluconeogenic substrates. Additionally, another subunit *Gid7* plays role in specific substrate degradation. Ubiquitylated substrates then pass through the *Cdc48* system and are ultimately targeted for proteasomal degradation.*

Under stress conditions such as heat shock, osmotic shock, nitrogen starvation or amino acid starvation, substrate receptor *Gid10* is induced, which recruits *Art2* via its N-terminal proline [80]. Ubiquitylation of *Art2* in turn affects its RSP5 dependent import of amino acid

transporters. Recently identified substrate receptor *Gid11* is induced during ethanol starvation and other stress conditions and it specifically targets substrates with Thr/N-degrons [71]. However, structural and functional validation of *Gid11* is required for further understanding.

1.6.2. Regulation by mammalian CTLH

The CTLH E3 substrate regulation in human is still unclear although numerous substrates of CTLH such as *Hbp1*, *lamin B2*, *AMPK*, *muskelin* have been proposed so far [77, 86, 89, 98, 99]. Additionally, the individual subunits of CTLH complex have been linked to numerous key biological functions (Fig. 6), including brain development (*WDR26*, *RANBP9*, *RMND5a*) [100-102], red blood cell development (*UBE2H*, *MAEA*, *WDR26*) [99, 103, 104], cell migration (*RANBP9*, *TWA1*) [105, 106], WNT pathway (*TWA1*, *WDR26*) [107, 108] and cell cycle regulation (*WDR26*) [77]. Mutations in human *WDR26* are also linked to a neurodevelopmental disorder called “Skraban-Deardorff syndrome” [102]. Although human *Gid4* binding pocket is structurally similar to yeast *Gid4*, substrates of human *Gid4* have not been identified yet. Humans also have two orthologs of *Gid7*, *WDR26* and *MKLN1*, which both associate with other subunits to form the CTLH complex, but how these orthologs of *Gid7* regulate the CTLH complex is not known.

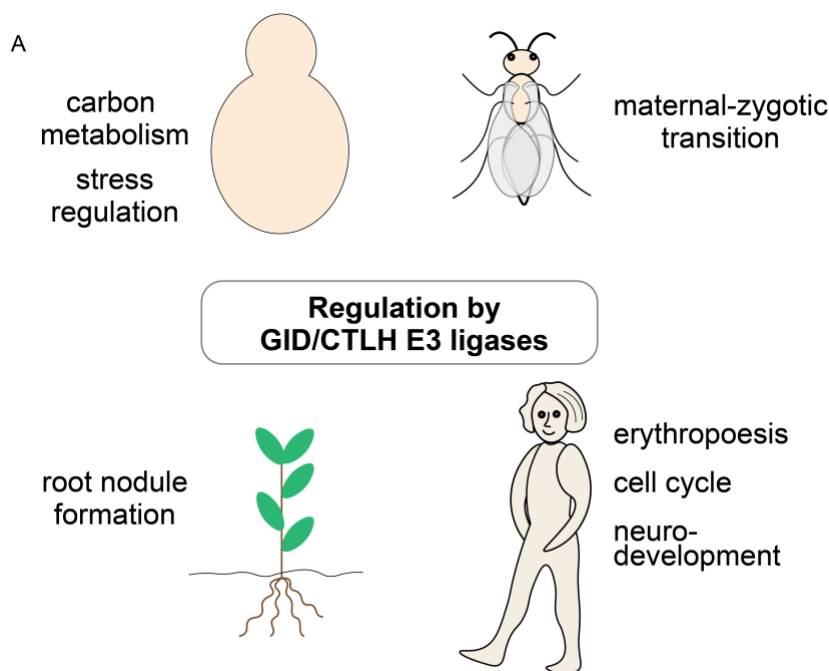


Figure 6. Overview GID and CTLH functions.

(A) The GID/CTLH family of E3 ligases are evolutionarily conserved and regulate diverse biological pathways in different organisms like yeast, drosophila, plant and human.

1.6.3. Regulation by other CTLH

In *drosophila*, the CTLH complex is linked to developmental control [85, 109]. Apart from *Gid4* and *ARMC8*, the orthologs of human CTLH subunits have been reported in *drosophila*. Moreover, the *drosophila* CTLH subunits are important for degradation of RNA binding proteins *MET31B*, *TRAL* and *Cup* during early stages of maternal to zygotic transition (Fig. 6).

In plants, in the *Lotus japonicus* family, a new CTLH domain-rich RING E3 ligase named SIE3, which is homologous to GID/CTLH family, has been identified. The E3 ligase is involved in regulation of root nodulation and rhizobial infection in plants (Fig. 6) [110].

1.7. Aims of this study

Numerous studies conducted over the past two decades identified the GID E3 ligase as the key machinery that leads to degradation of the gluconeogenic enzymes, namely Fbp1, Mdh2, Pck1 and Icl1, in yeast [65, 67-69]. Moreover, these substrates had different oligomeric states and their amino acid sequences were not similar. Additionally, the biochemical and mechanistic details of how these different substrates get recognized by a singular GID E3 ligase were not known. Therefore, reconstituting the GID complex components *in vitro*, dissecting their mechanisms through biochemical experiments and visualizing the structures of substrate receptors bound to different degrons were one of the first goals.

Previously, a study highlighting the regulation, structural assembly and mechanism of an active yeast GID^{SR4} complex, with Gid1, Gid2, Gid4, Gid5, Gid8 and Gid9, was published from our lab [74]. However, the structure did not include Gid7. We knew from previous studies from the lab of Dieter Wolf that Gid7 is necessary for glucose-induced degradation of Fbp1. Therefore, we asked how Gid7 facilitates such a regulation of Fbp1, despite the presence of an already competent E3 ligase system. So, validating the structural features of the GID complex with Gid7 by cryo EM and characterizing the specific functions carried out by Gid7 or its human orthologs WDR26 or MKLN1 were the central focus of my Ph.D.

The mammalian ortholog of the yeast GID complex, the CTLH E3 ligase has been implicated to function during erythropoiesis, cell cycle, neurodevelopment and numerous other biological processes. However, the substrate regulation by the CTLH complex is not sufficiently investigated. Therefore, it was also of interest to investigate the mechanistic and structural features of the human CTLH, particularly to answer if they were structurally analogous to yeast GID E3, which could in turn provide us some cues to understand its functional and substrate regulatory mechanisms.

2. Publications

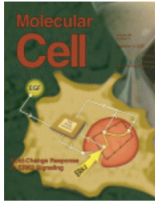
2.1. GID E3 ligase supramolecular chelate assembly configures multipronged ubiquitin targeting of an oligomeric metabolic enzyme. (Sherpa and Chrustowicz, et al. Molecular Cell, 2021)

This section includes my first co-first author paper that has been reprinted according to the permission from the Elsevier (licensed by Creative Commons). A brief summary and my contributions to this project are listed below.

Here, using a multidisciplinary approach that includes cryo-EM and structure-based functional studies, we have discovered that Gid7 transforms two fully functional multiprotein GID^{SR4} E3 ligase complexes into a higher-order assembly, which we term Chelator-GID^{SR4}. Chelator-GID^{SR4} encapsulates Fbp1 tetramer in its hollow center to allow for its efficient ubiquitylation. We have also answered how this complex is exquisitely tailored for targeting the oligomeric structure and function of the substrate Fbp1. Moreover, we also show that the key structural and mechanistic features of yeast Chelator-GID^{SR4} are preserved in the human CTLH E3 ligase. Overall, our study provides novel concepts for assembly of higher-order E3 ligases and how such an assembly mediates substrate regulation.

In particular, for this paper I contributed the following:

- preparation of experimental materials, planning of individual experiments, manuscript preparation
- *in vitro* biochemical assays (Fig. 1A, 1B, 1C, 1D, 4D, 5E, 5F, S1(A-D), S2A, S2B, S5 (assay for the target lysine site determination)), *in vivo* yeast degradation assays (Fig. 1F – Pck1 degradation assays, 5B, S1E), preparation of samples for cryo EM, model building for high resolution structures of Chelator-GID^{SR4} substrate receptor scaffolding (SRS) module (Fig.3, PDB ID: 7NS3) and catalytic (Cat) module (Fig.3, PDB ID: 7NS4), determination of low resolution cryo EM structures of GID^{SR4+} (Fig. 2B, EMD-12548), determination of endogenous Chelator-GID (Fig 2C, S2D, EMD-12538, EMD-12540), determination of human CTLH WDR26 (Fig. 6C, EMD-12545) , sample preparation, optimization and determination of Fbp1 crystal structure (Fig. 2D, 4C, 5C, S5C, PDB ID: 7NS5)



GID E3 ligase supramolecular chelate assembly configures multipronged ubiquitin targeting of an oligomeric metabolic enzyme

Author:

Dawafuti Sherpa, Jakub Chrustowicz, Shuai Qiao, Christine R. Langlois, Laura A. Hehl, Karthik Varma Gottemukkala, Fynn M. Hansen, Ozge Karayel, Susanne von Gronau, J. Rajan Prabu, Matthias Mann, Arno F. Alpi, Brenda A. Schulman

Publication: Molecular Cell

Publisher: Elsevier

Date: 3 June 2021

© 2021 The Author(s). Published by Elsevier Inc.

Journal Author Rights

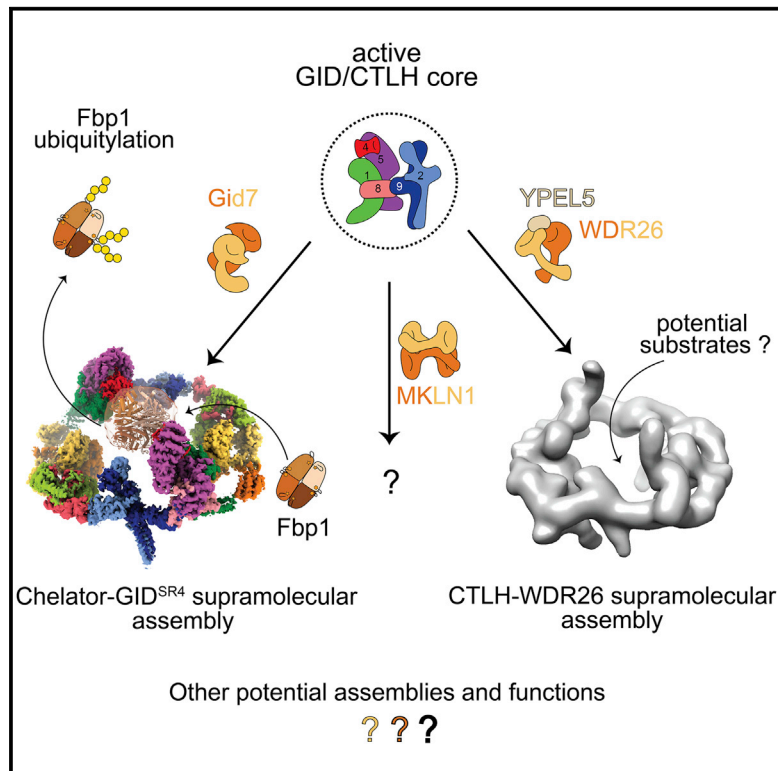
Please note that, as the author of this Elsevier article, you retain the right to include it in a thesis or dissertation, provided it is not published commercially. Permission is not required, but please ensure that you reference the journal as the original source. For more information on this and on your other retained rights, please visit: <https://www.elsevier.com/about/our-business/policies/copyright#Author-rights>

BACK

CLOSE WINDOW

GID E3 ligase supramolecular chelate assembly configures multipronged ubiquitin targeting of an oligomeric metabolic enzyme

Graphical abstract



Authors

Dawafuti Sherpa, Jakub Chrustowicz, Shuai Qiao, ..., Matthias Mann, Arno F. Alpi, Brenda A. Schulman

Correspondence

schulman@biochem.mpg.de

In brief

Structural, biochemical, and cellular data reveal supramolecular assembly of yeast GID E3 ligase. GID E3 forms a chelate-like structure tailored to target the oligomeric structure and metabolic function of the gluconeogenic enzyme substrate Fbp1. The orthologous human CTLH E3 contains a GID-like core assembly that forms a supramolecular chelate and utilizes a GID-like ubiquitin ligase mechanism.

Highlights

- GID E3 ligase assembly resembles a behemoth organometallic supramolecular chelate
- Multipronged targeting of oligomeric structure and metabolic function of substrate
- Yeast Gid7, human WDR26, and MKLN1 mediate supramolecular assembly of GID/CTLH E3s
- Human CTLH E3 structural and mechanistic features parallel yeast GID E3 ligase

Article

GID E3 ligase supramolecular chelate assembly configures multipronged ubiquitin targeting of an oligomeric metabolic enzyme

Dawafuti Sherpa,^{1,3} Jakub Chrustowicz,^{1,3} Shuai Qiao,¹ Christine R. Langlois,¹ Laura A. Hehl,¹ Karthik Varma Gottemukkala,¹ Fynn M. Hansen,² Ozge Karayel,² Susanne von Gronau,¹ J. Rajan Prabu,¹ Matthias Mann,² Arno F. Alpi,¹ and Brenda A. Schulman^{1,4,*}

¹Department of Molecular Machines and Signaling, Max Planck Institute of Biochemistry, Martinsried 82152, Germany

²Department of Proteomics and Signal Transduction, Max Planck Institute of Biochemistry, Martinsried 82152, Germany

³These authors contributed equally

⁴Lead contact

*Correspondence: schulman@biochem.mpg.de

<https://doi.org/10.1016/j.molcel.2021.03.025>

SUMMARY

How are E3 ubiquitin ligases configured to match substrate quaternary structures? Here, by studying the yeast GID complex (mutation of which causes deficiency in glucose-induced degradation of gluconeogenic enzymes), we discover supramolecular chelate assembly as an E3 ligase strategy for targeting an oligomeric substrate. Cryoelectron microscopy (cryo-EM) structures show that, to bind the tetrameric substrate fructose-1,6-bisphosphatase (Fbp1), two minimally functional GID E3s assemble into the 20-protein Chelator-GID^{SR4}, which resembles an organometallic supramolecular chelate. The Chelator-GID^{SR4} assembly avidly binds multiple Fbp1 degrons so that multiple Fbp1 protomers are simultaneously ubiquitylated at lysines near the allosteric and substrate binding sites. Importantly, key structural and biochemical features, including capacity for supramolecular assembly, are preserved in the human ortholog, the CTLH E3. Based on our integrative structural, biochemical, and cell biological data, we propose that higher-order E3 ligase assembly generally enables multipronged targeting, capable of simultaneously incapacitating multiple protomers and functionalities of oligomeric substrates.

INTRODUCTION

Cells rapidly adapt their metabolic pathways in response to nutrient availability (Tu and McKnight, 2006; Zaman et al., 2008; Zhu and Thompson, 2019). Shifts in metabolic enzyme activities are achieved by regulation at every conceivable level. Metabolite-responsive transcriptional programs activate pathways that maximally use available nutrients and repress those rendered unnecessary or counterproductive. For oligomeric enzymes, catalytic activities are subject to metabolite-mediated allosteric control (Koshland, 1963a, 1963b; Monod et al., 1963). In eukaryotes, undesired metabolic activities are often terminated by ubiquitin-mediated degradation (Nakatsukasa et al., 2015).

Degradation is typically controlled by recognition of proteins as substrates of E3 ubiquitin (Ub) ligases. However, little is known about whether or how E3 ligases are specifically tailored for oligomeric assemblies of metabolic enzymes. One of the first identified targets of nutrient-dependent degradation, budding yeast fructose-1,6-bisphosphatase (Fbp1), is an oligomer (Chiang and Schekman, 1991). Fbp1 is a gluconeogenic enzyme essential for yeast growth on non-fermentable carbon sources. A shift from gluconeogenic to glycolytic conditions renders gluconeogenesis

superfluous. Accordingly, Fbp1 activity and expression are curtailed (Gancedo, 1971; Schork et al., 1994a, 1994b, 1995). The switch to glycolytic conditions induces Ub-mediated degradation of Fbp1 and other gluconeogenic enzymes, including malate dehydrogenase (Mdh2) and phosphoenolpyruvate carboxylase (Pck1), mediated by the multiprotein E3 ligase termed "GID"; yeast mutants of Gid subunits are glucose-induced-degradation deficient (Braun et al., 2011; Chiang and Schekman, 1991; Hämmerle et al., 1998; Menssen et al., 2012; Regelmann et al., 2003; Santt et al., 2008; Schork et al., 1994b, 1995). Although the GID E3 is conserved across eukaryotes and regulates important physiology (Lampert et al., 2018; Liu et al., 2020; Liu and Pfirrmann, 2019; Salemi et al., 2017), its regulation and targets are best characterized in budding yeast.

Much like well-studied multiprotein E3 ligases, such as anaphase-promoting complex/cyclosome (APC/C) or cullin-RING ligases, GID is not a singular complex—a core catalytic and scaffolding assembly is modulated by other subunits (Barford, 2020; Karayel et al., 2020; Liu and Pfirrmann, 2019; Melnykov et al., 2019; Qiao et al., 2020; Rusnac and Zheng, 2020; Watson et al., 2019). The constituents of various GID assemblies and how they achieve regulation are beginning to emerge. Previous structural studies have elucidated the core assembly and

recapitulated some GID regulation (Qiao et al., 2020). Briefly, a core inactive complex, GID^{Ant}, contains the heterodimeric E3 ligase RING and RING-like subunits (Gid2 and Gid9) and scaffold subunits (Gid1, Gid5, and Gid8). Coexpression of these subunits in insect cells enables purification of recombinant GID^{Ant} and systematic interrogation of GID functions. Within the GID^{Ant} scaffold, Gid5 can bind the structurally homologous, interchangeable substrate-binding receptors Gid4 and Gid10 (Karayel et al., 2020; Melnykov et al., 2019; Qiao et al., 2020). Of these, the molecular basis of substrate binding by Gid4 is well understood: glucose-induced incorporation of Gid4 into the GID E3 enables recognition of substrate “Pro/N-degron” motifs depending on an N-terminal proline (Chen et al., 2017; Dong et al., 2018; Hämmerle et al., 1998; Regelmann et al., 2003; Santt et al., 2008). Indeed, *in vitro*, adding Gid4 transforms GID^{Ant} into an active GID^{SR4} complex that collaborates with the cognate E2, Ubc8 (also known as Gid3) to ubiquitylate Mdh2, as explained by a structure of GID^{SR4} (Qiao et al., 2020). Mutations probing the GID^{SR4} structure also showed that this assembly is required for glucose-induced Fbp1 degradation *in vivo* (Qiao et al., 2020).

Perplexingly, despite the crucial role of Fbp1 in regulating gluconeogenesis, its ubiquitylation has not been reconstituted *in vitro* using defined GID E3 ligase components. *In vivo*, Fbp1 degradation depends on another protein, Gid7, which associates with other Gid subunits (Menssen et al., 2012; Regelmann et al., 2003; Santt et al., 2008). Gid7 is evolutionarily conserved across eukaryotes. Mammals even have two orthologs, WDR26 and MKLN1, which are subunits of the “CTLH” complex that corresponds to the yeast GID E3 (Boldt et al., 2016; Francis et al., 2013; Kobayashi et al., 2007; Lampert et al., 2018; Liu and Pfirrmann, 2019; Salemi et al., 2017). The CTLH E3, named for the preponderance of CTLH domains (in Gid1, Gid2, Gid7, Gid8, and Gid9 and their orthologs), has intrinsic E3 ligase activity, although Pro/N-degron substrates have not yet been identified despite human Gid4 binding this motif (Cao et al., 2020; Dong et al., 2018; Lampert et al., 2018; Liu et al., 2020; Liu and Pfirrmann, 2019; Maitland et al., 2019; Zavortink et al., 2020).

Here we reconstitute a minimal GID E3 ligase active toward Fbp1 by combining GID^{SR4} and Gid7. Cryoelectron microscopy (cryo-EM) reveals its structure as a 20-protein supramolecular chelate E3 ligase assembly specifically tailored for Fbp1’s quaternary structure. Structural and biochemical data suggest that the human Gid7 orthologs likewise transform a GID^{SR4}-like E3 ligase core into higher-order assemblies. Our data reveal supramolecular chelate assembly of a pre-existing, functionally competent E3 ligase complex as a structural and functional principle to achieve multipronged Ub targeting tailored to an oligomeric substrate.

RESULTS

Reconstitution of Fbp1 ubiquitylation

Considering that the Gid7 protein, not visualized previously, is required for glucose-induced Fbp1 degradation *in vivo* (Regelmann et al., 2003), we tested its effect *in vitro*. Our assay setup probes modulation of the core recombinant GID^{Ant} assembly upon adding other purified components individually or in combination. First, adding Gid4 marginally stimulated Fbp1 ubiquityla-

tion despite substantially potentiating ubiquitylation of Mdh2, another canonical Pro/N-degron substrate, and Pck1, whose recognition by the GID E3 remains elusive (Figure 1A). However, adding Gid7 together with Gid4 substantially increased Fbp1 ubiquitylation. Comparing reactions with wild-type (WT) Ub or a Ub version lacking lysines (K0Ub) that cannot form polyUb chains indicated that adding Gid7 increases substrate consumption, the number of modified Fbp1 sites, and the number of Ubs in polyUb chains (Figures 1A and 1B). Second, the remarkable activation upon addition of Gid7 was specific to Fbp1; effects on Pck1 were negligible, and effects on Mdh2 were nuanced in increasing polyUb chain length while attenuating the amount of Mdh2 molecules consumed in the assay (Figure 1A). Third, adding Gid7 actually suppressed intrinsic GID E3 ligase activity, as shown by effects on Ub transfer from a pre-formed Ubc8~Ub intermediate to free lysine in solution (Figure S1A). Binding of Fbp1’s degron per se is insufficient to overcome this inhibition because Gid7 likewise subdued ubiquitylation of a model peptide substrate in which Fbp1’s degron sequence, PTLV, is connected to a lysine acceptor through an intervening flexible linker (Figure S1B).

To gain mechanistic insights, we quantified effects of including Gid7 in a chromatographically purified version of the E3 by performing enzyme kinetics. Compared with GID^{SR4}, a version of the E3 complex fully incorporating Gid7 displayed a relatively 10-fold lower Michaelis-Menten constant, K_m , for Fbp1 ubiquitylation and 10-fold increase in the reaction turnover number k_{cat} (Figures 1C, 1D, S1C, and S1D). Adding purified Gid7 to GID^{SR4} had similar effects (Figures 1C and S1C).

Consistent with the biochemical data, glucose-induced ubiquitylation of Fbp1 *in vivo* is impaired by Gid7 deletion (Figure 1E). To examine effects on degradation, we employed a promoter reference technique that monitors degradation of exogenously expressed proteins (here, C-terminally FLAG-tagged Fbp1, Mdh2, or Pck1) while normalizing for effects on expression (Chen et al., 2017; Oh et al., 2017). Our assay agreed with prior studies showing that glucose-induced degradation of Fbp1, Mdh2, and Pck1 depends on Gid4 (Chen et al., 2017; Qiao et al., 2020; Regelmann et al., 2003; Santt et al., 2008). However, Gid7 deletion substantially stabilized only Fbp1 (Figure 1F). This deficit in Fbp1 degradation upon Gid7 deletion was not rescued by Gid4 overexpression (Figure S1E). Also, quantitative mass spectrometry analyses of the yeast proteome confirmed that, of known gluconeogenic GID E3 substrates, Fbp1 was most affected by Gid7 deletion (Figure S1F).

A supramolecular Chelator-GID^{SR4} E3 assembly encapsulates the tetrameric Fbp1 substrate

To understand the mechanism of Fbp1 recognition by the GID E3, we purified an Fbp1-active recombinant complex and analyzed its structure by cryo-EM (Figures S2A and S4; Table S1). A 13-Å-resolution map of the assembly even without the substrate showed a remarkable GID E3 structure: an exterior oval supporting several inward-pointing globular domains. Strikingly, the longest exterior dimension of 305 Å is roughly comparable with that of a singly capped 26S proteasome, 1.3 times that of the multiprotein Fanconi anemia E3 ligase complex and 1.5 times that of APC/C (Figure 2A)

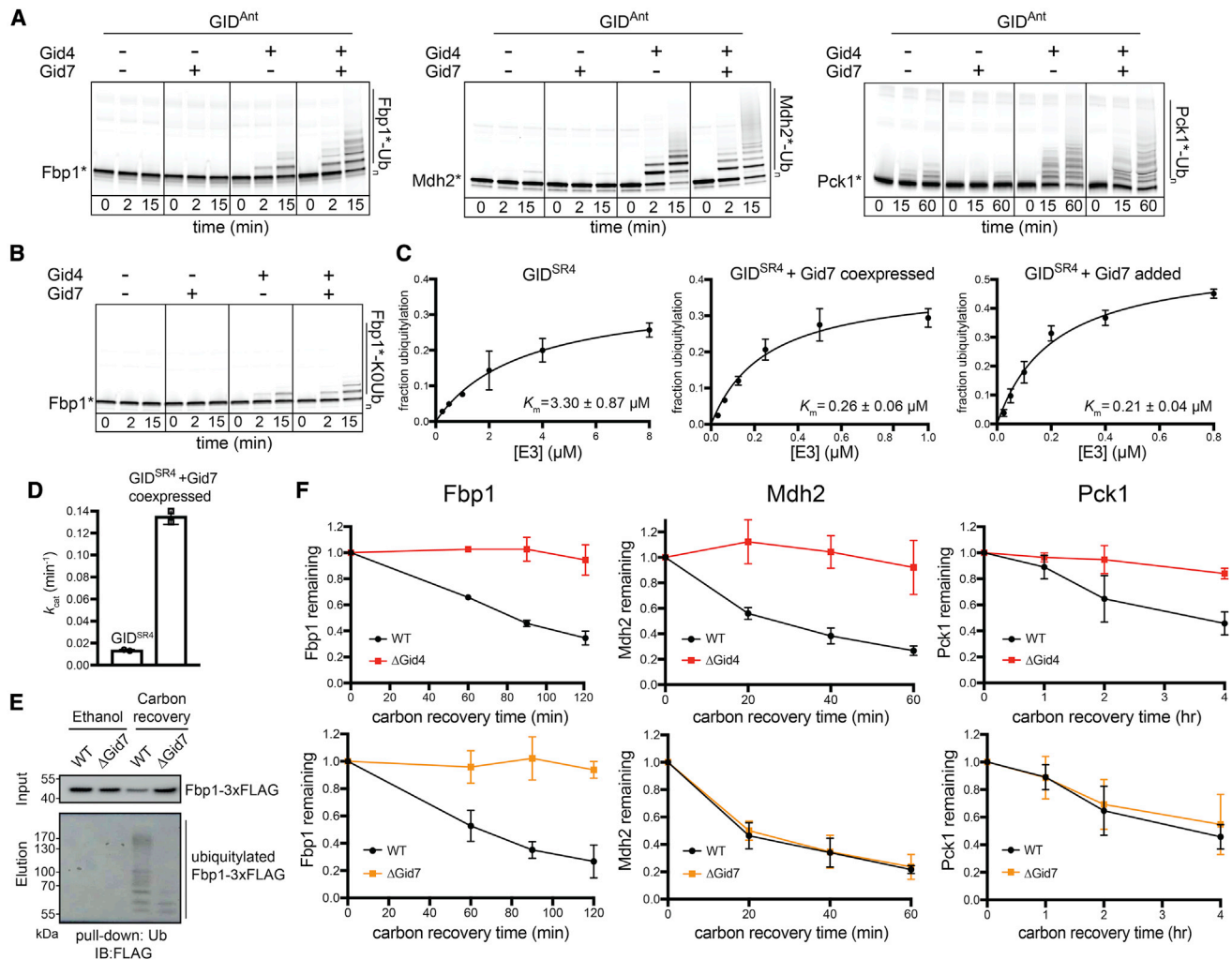


Figure 1. Fbp1 ubiquitylation and degradation require a distinct Gid7-containing GID E3 ligase

(A) Fluorescence scans of SDS-PAGE gels showing *in vitro* ubiquitylation assays. These assays test the roles of Gid4 and Gid7 in ubiquitylation of C-terminally fluorescently labeled Fbp1 (left), Mdh2 (center), and Pck1 (right). GID^{Ant} contains 2 protomers each of Gid1 and Gid8 and 1 of Gid2, Gid5, and Gid9. An asterisk indicates that substrates are fluorescently labeled.

(B) *In vitro* ubiquitylation assay as in (A) but performed with lysine-less Ub (K0Ub) to determine the number of Fbp1 ubiquitylation sites.

(C) Plots showing fraction of Fbp1 ubiquitylation as a function of concentration of GID^{SR4} (left) or its complex with Gid7 (center and right). K_m values were determined by fitting to the Michaelis-Menten equation. Error bars, SD ($n = 2$).

(D) Comparison of k_{cat} between GID^{SR4} and its complex with Gid7, determined from plots in Figure S1D. Error bars, SD ($n = 2$).

(E) Assessing *in vivo* ubiquitylation of Fbp1 (C-terminally 3×FLAG-tagged at the endogenous locus) under carbon starvation (ethanol) and after 2 h of carbon recovery in WT and Δ Gid7 yeast strains. Following capture of ubiquitylated proteins with TUBEs (tandem ubiquitin binding entities), Fbp1-3×FLAG was visualized by anti-FLAG immunoblotting.

(F) Glucose-induced degradation *in vivo* of exogenously expressed substrates Fbp1 (left), Mdh2 (center), and Pck1 (right), quantified using the promoter reference technique. Substrate levels were quantified as the ratio of substrate detected relative to the level after switching from carbon starvation to carbon recovery conditions in WT, Δ Gid4 (top panels), and Δ Gid7 (bottom panels) strains. Points represent mean, and error bars represent SD ($n \geq 3$).

See also Figure S1.

(Brown et al., 2016; Chen et al., 2016; Haselbach et al., 2017; Lander et al., 2012; Schweitzer et al., 2016; Shakeel et al., 2019; Wehmer et al., 2017). Unlike these compact assemblies, however, this GID complex displays a behemoth hollow center with interior edges of 270 and 130 Å in the longest and shortest dimensions, respectively—larger than a cullin-RING ligase ubiquitylating a substrate (Baek et al., 2020).

The organization of the oval GID assembly was gleaned from comparison with cryo-EM maps of subcomplexes (Figure 2B; Table S1). Two copies of the previously defined GID^{SR4} structure (Qiao et al., 2020) fit in the large assembly. An additional Gid1-Gid8 subcomplex can be observed bound to GID^{SR4}. These duplicated Gid1 and Gid8 protomers are components of recombinant GID^{Ant} used for biochemical assays (Qiao et al., 2020) but

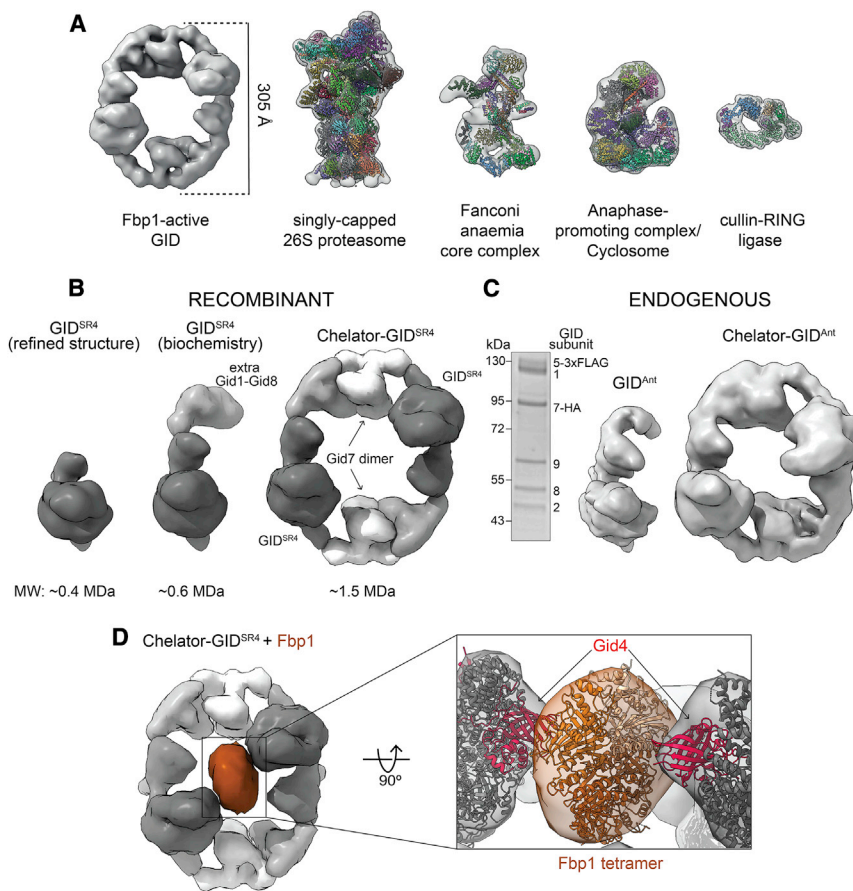


Figure 2. Multidentate capture of the Fbp1 tetramer by the Chelator-GID^{SR4} assembly

(A) Cryo-EM map of GID E3 active toward Fbp1 compared for scale with low-pass-filtered maps of the singly capped 26S proteasome (EMDB: EMD-3536; PDB: 5MPB), Fanconi anemia core complex (EMDB: EMD-10290; PDB: 6SRI), APC/C (EMDB: EMD-3433; PDB: 5L9T), and cullin-RING E3 ubiquitylation complex (EMDB: EMD-10585; PDB: 6TTU).

(B) Cryo-EM maps and molecular weights of recombinant GID assemblies. Structurally determined GID^{SR4} (left, low-pass-filtered, dark gray, EMDB: EMD 10327; PDB: 6SWY) is a stoichiometric complex of Gid1, Gid8, Gid5, Gid4, Gid2, and Gid9. The purification conditions used here include an additional Gid1-Gid8 subcomplex (gray) bound to GID^{SR4} (center, taken for the biochemical assays). The oval higher-order Chelator-GID^{SR4} assembly includes Gid7 dimers (right, white).

(C) Coomassie-stained SDS-PAGE (left) and cryo-EM maps of endogenous yeast GID^{Ant} (center) and Chelator-GID^{Ant} (right) assemblies (prepared by anti-FLAG immunoprecipitation of lysates from yeast with Gid5 3×FLAG tagged and Gid7 hemagglutinin (HA) tagged at their endogenous loci and grown under conditions when Gid4 is not induced). (D) Cryo-EM map of Chelator-GID^{SR4} (gray) bound to the Fbp1 tetramer (brown). The close up shows 2 red Gid4 protomers (modeled from PDB: 6SWY) simultaneously contacting the docked Fbp1 crystal structure.

See also [Figure S2](#) and [Tables S1](#) and [S2](#).

are not visible upon map refinement to high resolution. We interpreted the remaining density in the large oval GID assembly as Gid7 dimers, one at each vertex, given size exclusion chromatography-multi angle light scattering (SEC-MALS) data indicating that purified Gid7 dimerizes ([Figure S2B](#)). The data reveal a 1.5-MDa eicosameric GID assembly composed of 4 Gid1: 2 Gid2: 2 Gid4: 2 Gid7: 4 Gid8: 2 Gid9 protomers.

We sought to determine whether this GID assembly might be formed *in vivo*. Prior studies did ([Santt et al., 2008](#)) or did not ([Qiao et al., 2020](#)) observe Gid7 cosedimenting with other GID proteins in density gradients. This raised the possibility that, like the equally giant 26S proteasome, some subunits or regulatory partners may be prone to dissociation; for example, based on lysis conditions ([Leggett et al., 2002](#)). Thus, we examined sedimentation of a core subunit, Gid8 tagged at the endogenous locus, as a marker for a GID assembly because it cosediments with all other GID^{SR4} subunits even under relatively harsh lysis conditions ([Qiao et al., 2020](#)). Yeast lysates prepared by cryomilling were subjected to sucrose density gradient fractionation. Anti-FLAG immunoblotting showed Gid8 migrating at a lower molecular weight in a Gid7 deletion compared with the WT, irrespective of whether yeast was grown under carbon starvation or recovery in glucose, which induces GID E3 ligase activity ([Figure S2C](#)). Moreover, cryo-EM data of endogenous GID purified from yeast grown under carbon starvation yielded 3D recon-

structions corresponding to the recombinant assemblies with and without Gid7 at 14.2- and 9.5-Å resolution, respectively ([Figures 2C](#) and [S2D](#)).

Why is the minimum E3 ligase for Fbp1 so gigantic and hollow? Given the substantial effect on K_m in our enzyme kinetics analyses, we hypothesized that such an assembly would form to accommodate the substrate. To characterize the substrate, we determined the crystal structure of yeast Fbp1, which confirmed its tetrameric assembly ([Figures 2D](#) and [S2B](#); [Table S2](#)). We next resolved a cryo-EM structure with Fbp1 bound to the GID E3, which led to several conclusions ([Figure 2D](#); [Table S1](#)). First, Fbp1 was readily docked in the center of the large GID E3 oval. Second, two Fbp1 edges approach the substrate binding Gid4 subunits within each GID^{SR4} on opposite sides of the oval. Third, the density attributed to Gid7 does not directly contact Fbp1 but connects two Fbp1-binding GID^{SR4} complexes. Thus, Gid7 activates GID E3 activity toward Fbp1 indirectly by driving supramolecular assembly.

The resultant GID assembly resembles an organometallic supramolecular chelate in which multiple giant organic molecules capture a much smaller ligand through multiple discrete points of contact. Thus, we call the giant oval complex “Chelator-GID^{SR4}” based on its supramolecular assembly in which two GID^{SR4} complexes simultaneously capture degrons displayed from two protomers in the tetrameric Fbp1 substrate.

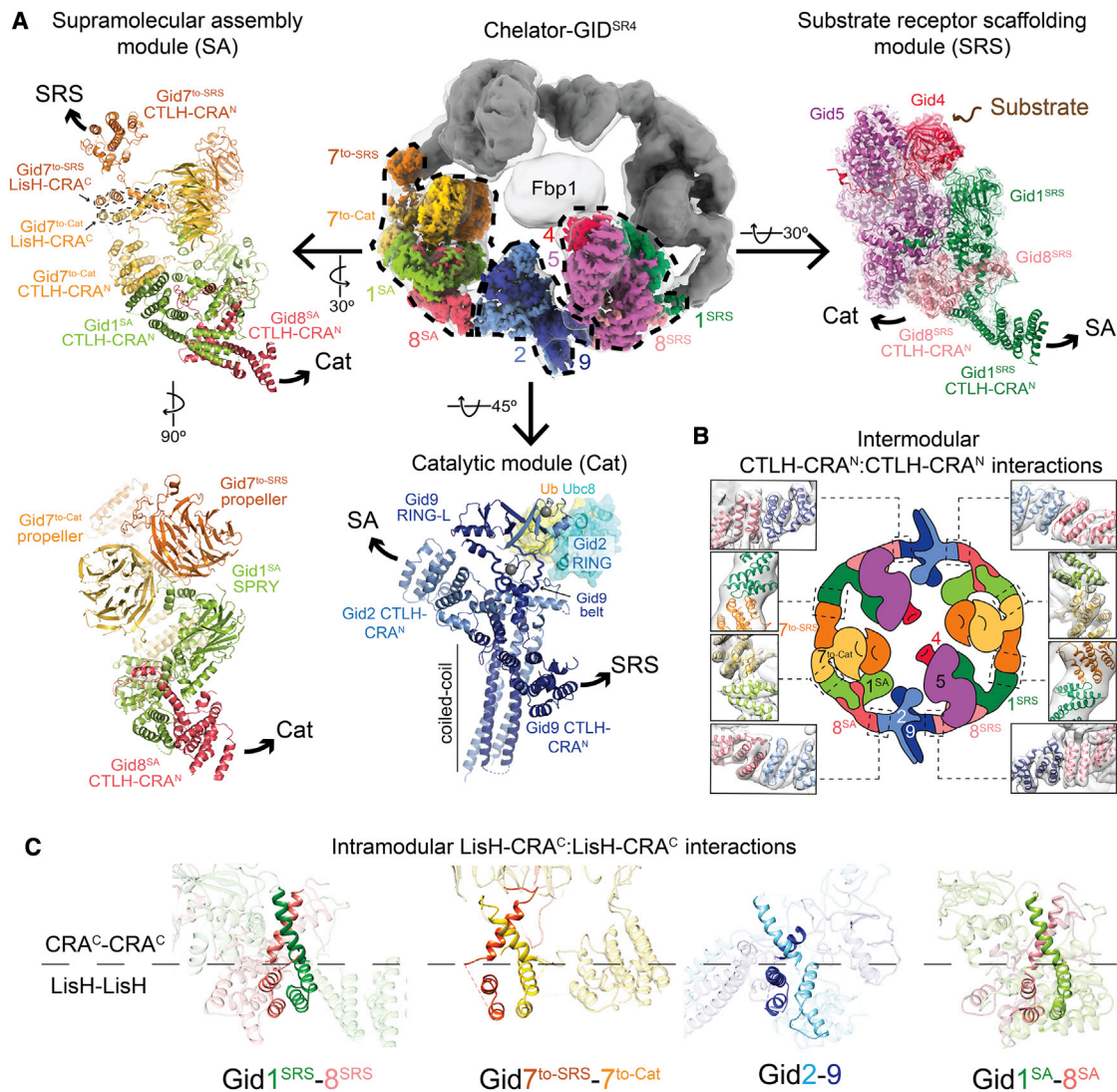


Figure 3. High-resolution details of Chelator-GID^{SR4} modular assembly

(A) Focused refined maps of the substrate receptor scaffolding (SRS), catalytic (Cat), and supramolecular assembly (SA) modules, colored according to subunit identity, fit in half of the overall map of Fbp1-bound Chelator-GID^{SR4} (top center). The GID^{SR4} structure (PDB: 6SWY) fits the SRS module (Gid1^{SRS}, dark green; Gid8^{SRS}, salmon; Gid5, purple; Gid4, red). A brown arrow points to Gid4's substrate binding site (top right). The Cat module comprises Gid2 (sky blue) and Gid9 (navy). Zinc ions are shown as gray spheres. Ubc8~Ub was modeled by aligning Gid2 RING with an E2~Ub-bound RING structure (PDB: 5H7S). The SA module comprises Gid1^{SA} (green), Gid8^{SA} (pink) and 2 Gid7 protomers, Gid7^{to-Cat} (yellow), and Gid7^{to-SRS} (orange) facing the Cat or SRS module, respectively. Superscript text refers to a module for a given Gid1 or Gid8 protomer. Arrows point to connected modules.

(B) Cartoon of Chelator-GID^{SR4} with close ups of intermodule CTLH-CRA^N:CTLH-CRA^N interactions fit into the map of Chelator-GID^{SR4} (gray).

(C) Intramodular LisH-CRA^C:LisH-CRA^C (solid ribbon) interactions in Chelator-GID^{SR4}.

See also [Figures S3](#) and [S4](#) and [Table S1](#).

High-resolution structures of modules in Chelator-GID^{SR4}

A series of focused refinements enabled building atomic models of the three functionally distinct modules comprising Chelator-GID^{SR4} ([Figures 3A](#), [S2E](#), [S3A](#), and [S4](#); [Table S1](#)): (1) the substrate receptor scaffolding (SRS) module contained in GID^{SR4}, responsible for bridging the substrate receptor to the other E3 ligase subunits; (2) the catalytic (Cat) module, also present in GID^{SR4}, which binds and activates the Ubc8~Ub inter-

mediate; and (3) a previously undescribed supramolecular assembly (SA) module.

A 3.4-Å map of the Chelator-GID^{SR4} SRS module fit the prior coordinates for this region (PDB: 6SWY) ([Figures 3A](#) and [S4B](#)). As described previously, the globular substrate-binding domain of Gid4 fits snugly in a complementary concave surface of the scaffold subunit Gid5. This arrangement is supported by a base from Gid1^{SRS} and Gid8^{SRS}, which form an intricate heterodimer involving their LisH-CTLH-CRA domains.

Focused refinement over the Cat module yielded a 3.8-Å-resolution reconstruction (Figures 3A and S4C). The map quality permitted *de novo* building and refinement of atomic coordinates for the majority of Gid2 and Gid9 (Figure S3A). The catalytic function is mediated by a region of Gid2 that adopts an E3 ligase RING domain fold (albeit stabilized by a single zinc in the E2~Ub binding site) together with a portion of Gid9 that adopts a unique RING-like (RING-L) structure (Figure S3B; Braun et al., 2011; Qiao et al., 2020; Regelman et al., 2003). Folding of the Gid2 RING depends on its incorporation into the intricately configured Gid2-Gid9 heterodimer. The Gid2 RING is embedded in an unprecedented intermolecular heart-shaped domain, stabilized by Gid9 elements, including an intermolecular zinc-binding domain; a belt that encases roughly three quarters of the base of Gid2's RING; the RING-L domain, which packs against the remaining side of Gid2's RING; and the extreme C terminus, which contributes to Gid2's RING in a manner analogous to canonical RING dimers (Budhidarmo et al., 2012). Gid2 and Gid9 are further intertwined by their N termini co-assembling in an ~70-Å-long 4-helix coiled coil (Figures 3A and S3A).

Within Chelator-GID^{SR4}, the two Gid2-Gid9 E3 ligase domains face the two degron-binding Gid4 subunits. A model of the Gid2 RING-Ubc8~Ub intermediate based on published isolated RING E3-E2~Ub complexes shows the Gid2 RING domain recruiting Ubc8, whereas its linked Ub would be activated by Gid2 and Gid9 in the canonically activated conformation (Figures 3A and S3B; Dou et al., 2012; Plechanovová et al., 2012; Pruneda et al., 2012). The model explains the previously reported effects of Gid2 and Gid9 point mutations on Fbp1 degradation (Qiao et al., 2020).

A 3.6-Å resolution map of the SA module within Chelator-GID^{SR4} enabled building of an atomic model (Figures 3A and S4D). The two Gid7 protomers form an asymmetric dimer on one side of the module. Gid1^{SA} and Gid8^{SA} form an interdigitated scaffold that connects the Gid7 dimer to the Cat module.

Each Gid7 protomer consists of an N-terminal LisH-CTLH-CRA motif and an atypical β-propeller. The LisH-CTLH-CRA motifs form elongated helical double-sided dimerization domains (Figure S3C). The LisH and CTLH helices initially progress in one direction. The distal end is capped by the first two CRA helices. The remaining CRA helices reverse and traverse the length of the domain, pack against CTLH helices along the way, and terminate adjacent to the LisH helices. We refer to one side of the LisH-CTLH-CRA structure as “LisH-CRA^C” because it contains the LisH and C-terminal CRA helices. Accordingly, the other side is called “CTLH-CRA^N.” The Gid7 LisH-CRA^C motifs mediate homodimerization, much like LisH-CRA^C motifs mediate heterodimerization between Gid1^{SRS} and Gid8^{SRS} and between Gid2 and Gid9 (Qiao et al., 2020).

β-Propellers are protein interaction domains formed by toroidally arranged β sheet “blades” (Chen et al., 2011a). The 7-bladed propellers from the two Gid7 protomers ensue from the LisH-CTLH-CRA motifs at different relative angles and interact with each other. The resultant asymmetric double-propeller domain binds part of Gid1^{SA}. The SA module is further stabilized by distinctive interactions between the CTLH-CRA^N domains from Gid1^{SA}, a loop from Gid8^{SA}, and the CTLH-CRA^N

domain from a Gid7 protomer we call Gid7^{to-Cat} because it points toward the Cat module (Figure S3D). The remainder of the Gid1^{SA} and Gid8^{SA} subcomplex superimposes on corresponding regions of Gid1^{SRS} and Gid8^{SRS}. At the two edges of the SA module, the CTLH-CRA^N domains from the SRS-facing Gid7 protomer (Gid7^{to-SRS}) and Gid8^{SA} connect to the SRS and Cat modules, respectively.

Supramolecular chelate assembly is supported by inter- and intramodule LisH-CTLH-CRA domain interactions

The relative arrangement of E3 ligase elements—the Gid4 substrate receptor and the Gid2-Gid9 RING-RING-L complex—in Chelator-GID^{SR4} depends on the exterior oval band. The oval is established by two types of intersubunit interactions—within the modules and mediating intermodule connections—in a daisy chain-like arrangement of LisH-CTLH-CRA domains (Figures 3B and 3C).

In Chelator-GID^{SR4}, the modules are connected to each other by outward-facing heterotypic dimerization of CTLH-CRA^N domains at the edges of each module (Figure 3B). The CTLH-CRA^N domains connect modules in a side-by-side manner. In the GID^{SR4} assembly, the SRS and Cat modules are adjoined by interactions between the CTLH-CRA^N domains of Gid8^{SRS} and Gid9. The Cat and SA modules are bridged by interactions between the CTLH-CRA^N domains of Gid2 and Gid8^{SA}. Notably, Gid2's CTLH-CRA^N domain also packs against Gid9's RING-L domain, which may explain how formation of the Chelator-GID^{SR4} assembly affects intrinsic Ub transferase activity (Figures 3A, S1A, and S3B). The oval structure also depends on adjoining the SRS and SA modules through interactions between the CTLH-CRA^N domains of Gid1^{SRS} and Gid7^{to-SRS}. Despite the similarity of intermodule interactions at a secondary structural level, specificity is dictated by contacts between domains, ensuring formation of the Chelator-GID^{SR4} assembly.

Chelator-GID^{SR4} assembly mediates avid recruitment of the tetrameric substrate Fbp1

Comparing the major classes of Chelator-GID^{SR4} alone or bound to Fbp1 showed relative repositioning of the SRS module toward the center of the oval to bind the substrate, resembling a Venus flytrap capturing its prey (Figure 4A). An individual Fbp1 Pro/N-degron was visualized bound to Gid4 in a locally refined map of SRS (Figures 4B and S4B). Fbp1's N-terminal proline and two subsequent residues are recruited much like short peptides binding human Gid4 (Chen et al., 2017; Dong et al., 2018; Hämmerle et al., 1998). Comparing the substrate-bound Chelator-GID^{SR4} structure with the substrate-free GID^{SR4} (Qiao et al., 2020) shows remodeling of several Gid4 loops to embrace the N-terminal residues PTL of the Fbp1 substrate (Figure 4B).

Notably, the Pro/N-degrons and several subsequent residues are not visible in the Fbp1 crystal structure, suggesting that they are intrinsically disordered (Figure 4C). These elements could emanate from opposite sides of the disk-like Fbp1 catalytic domain. In the complex with Chelator-GID^{SR4}, degrons from both sides appear to simultaneously ensnare Gid4 substrate receptors. Such avid binding would rationalize the 10-fold lower K_m in Fbp1 ubiquitylation assays (Figure 1C). To further test

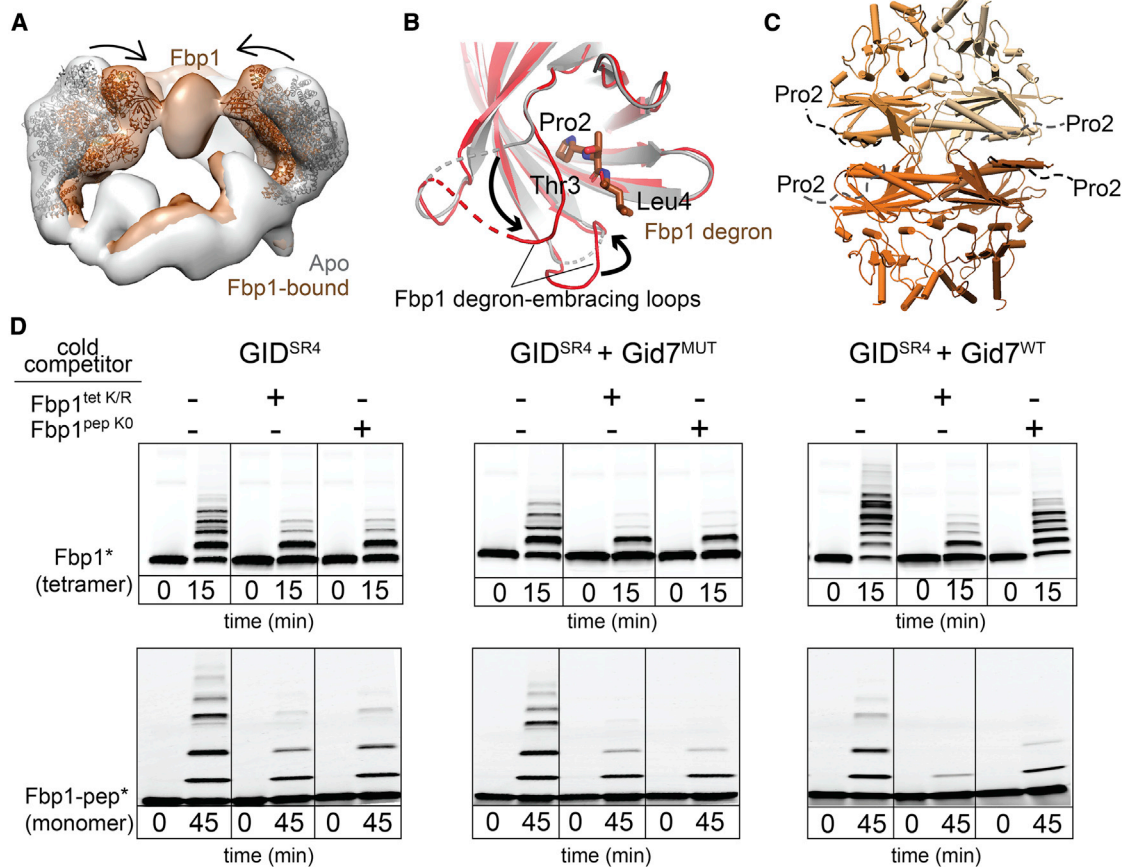


Figure 4. Chelator-GID^{SR4} assembly specifies multivalent binding for the tetrameric Fbp1 substrate

(A) Superimposed maps of substrate-free (gray) and Fbp1-bound Chelator-GID^{SR4} (brown) show relative inward movement of SRS modules (ribbon) upon substrate recruitment.

(B) Conformational differences between Gid4 in GID^{SR4} (PDB: 6SWY, gray) and Fbp1-bound Chelator-GID^{SR4} (red). The first three residues of Fbp1 (the Pro/ N-degron) bound to Gid4 are shown as sticks.

(C) Crystal structure of the Fbp1 tetramer, with the N-terminal region (residues 2–19), including the degron not visible in the electron density, depicted as dotted lines. Fbp1 protomers are shown in various brown shades.

(D) Competitive *in vitro* ubiquitylation assays probing multivalent E3-substrate interactions. Chelator-GID^{SR4} has two substrate binding sites and two catalytic centers, whereas two other E3 assemblies (GID^{SR4} or GID^{SR4} + Gid7^{MUT} lacking the LisH-CTLH-CRA motif, Δ1–285) have only one substrate binding site and one catalytic center. Substrates are oligomeric (tetrameric Fbp1) or monomeric (a peptide harboring a single acceptor Lys, Fbp1-pep) and fluorescently labeled at the C terminus (denoted by an asterisk). Competitors are oligomeric (tetrameric Fbp1^{tet K/R}, with preferred target lysines mutated to arginines) or monomeric (lysine-less peptide, Fbp1^{pep KO}).

See also [Figure S4](#) and [Tables S1](#) and [S2](#).

the possibility of avid substrate capture, we performed competitive qualitative ubiquitylation assays. Unlabeled monomeric and tetrameric Fbp1 competitors had a comparable inhibitory effect on ubiquitylation of fluorescent Fbp1 by GID^{SR4} or GID^{SR4} mixed with a Gid7 mutant that does not support supramolecular assembly (Figure 4D). However, compared with an unlabeled monomeric inhibitor, the unlabeled Fbp1 tetramer was strikingly more effective at impeding Chelator-GID^{SR4} ubiquitylation of fluorescent Fbp1. The same inhibitory trends were observed for ubiquitylation of a fluorescent monomeric peptide substrate, confirming that the Fbp1 tetramer complements the Chelator assembly. The data are consistent with avid Fbp1 recruitment to Chelator-GID^{SR4} depending on supramolecular assembly of the E3 ligase and its substrate.

Chelator-GID^{SR4} assembly establishes dual site-specific Ub targeting

We next mapped regions of Fbp1 engaging the ubiquitylation active sites. Locating di-Gly sites by mass spectrometry identified Chelator-GID^{SR4}-mediated ubiquitylation of two pairs of neighboring lysines, K32/K35 and K280/K281, preferentially from 18 potential target lysines on the surface of Fbp1 (Figure S5). The importance of these lysines was confirmed mutationally (Figures 5A and 5B). Use of K0 Ub had shown modification of up to two sites in an Fbp1 protomer during the time course of the experiment (Figure 1B). Eliminating either lysine pair reduced this to monoubiquitylation, with a slightly greater effect on the K32/K35 mutant (Figure 5A). The results suggest that either region can be ubiquitylated independent of the other but that, for

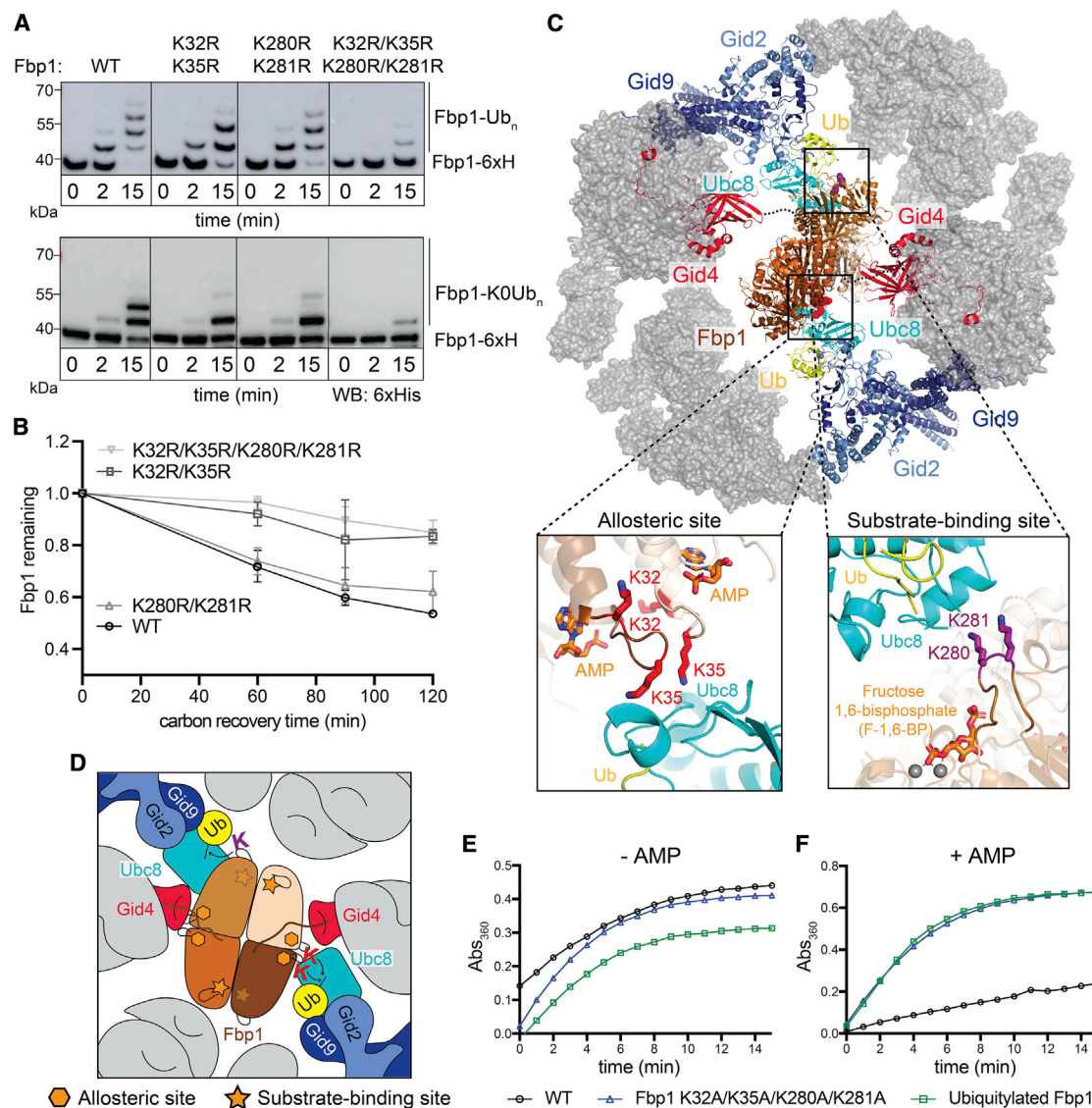


Figure 5. Chelator-GID^{SR4} configures simultaneous targeting of specific lysine clusters in metabolic regulatory regions of the Fbp1 tetramer

(A) *In vitro* ubiquitylation of Fbp1-6xHis, detected by anti-His immunoblotting, with WT (top) or K0 (bottom) Ub, testing the effects of mutating the major Fbp1 Ub-targeted lysines identified by mass spectrometry.

(B) Glucose-induced degradation *in vivo* of exogenously expressed WT or lysine mutant versions of Fbp1. Substrate levels were quantified as the ratio of substrate detected relative to the level after switching from carbon starvation to carbon recovery conditions. Points represent mean, and error bars represent SD (n = 3).

(C) Structural model of Chelator-GID^{SR4}-mediated ubiquitylation of Fbp1. Ubc8~Ub was modeled by aligning a RING-E2-Ub structure (PDB: 5H7S) on Gid2 RING. Dotted lines indicate disordered Fbp1 N termini. Close ups show major Fbp1 ubiquitylation sites near substrate (Fructose 1,6-bisphosphate, F-1,6-BP) and allosteric AMP binding sites modeled from structures with human Fbp1 (PDB: 5ZWK and 5ET6).

(D) Structure-based cartoon of Fbp1 ubiquitylation as shown in (C). Stars and hexagons represent substrate-binding and allosteric sites in Fbp1, respectively.

(E) *In vitro* Fbpase activity of purified WT, polyubiquitylated, and mutant Fbp1 (K32A/K35A/K280A/K281A).

(F) Fbpase activity assay as in (E), testing the responses of purified WT, polyubiquitylated, and mutant Fbp1 (K32A/K35A/K280A/K281A) to the allosteric inhibitor AMP.

See also Figure S5.

a given protomer, ubiquitylation is restricted to one lysine within a pair. Testing the effects of the mutations on Fbp1 degradation confirmed the importance of these lysines *in vivo*, with substantial stabilization even upon mutating only the K32/K35 lysine pair (Figure 5B).

To understand how the Chelator-GID^{SR4} supramolecular assembly determines regulation, we generated a structural model of ubiquitylation (Figures 5C and 5D). Fbp1 was first anchored via two degrons, one from each side binding a Gid4. Ubc8~Ub was modeled on the Gid2-Gid9 RING-RING-L domains based

on homology to another RING-E2~Ub assembly (Nayak and Sivaraman, 2018). Fbp1 was subjected to constrained rotation to localize the K32 and K35 region of one protomer adjacent to one active site. This led to two striking observations. First, the K32 and K35 regions of two pairs of protomers are adjacent to each other. Second, and unexpectedly, when a K32 and K35 region is aligned with one active site, the K280 and K281 region of a different Fbp1 protomer is simultaneously situated in the other Chelator-GID^{SR4} active site. Thus, the Chelator-GID^{SR4} supramolecular assembly complements the tetrameric structure of Fbp1 by enabling simultaneous capture of two Pro/N degrons and simultaneous ubiquitylation of multiple protomers within the Fbp1 tetramer.

Given that Fbp1 is allosterically regulated in response to metabolite binding (Ke et al., 1990a, 1990b), we inspected the structure for potential functional importance of the ubiquitylation sites (Figures 5C and 5D). Intriguingly, the K32 and K35 residues reside in a loop abutting the allosteric site that regulates Fbp1 activity by binding the non-competitive inhibitor AMP (Ke et al., 1990b). K280 and K281 are located adjacent to another interprotomer interface, relatively near the substrate binding site (Ke et al., 1990a). We thus examined the effects of Chelator-GID^{SR4} ubiquitylation on Fbp1 activity. A K32A/K35A/K280A/K281A mutant and a ubiquitylated version of Fbp1 show Fbpase activity in our assay. However, allosteric modulation by AMP was substantially impaired in both cases (Figures 5E and 5F). Thus, Chelator-GID^{SR4} targets sites related to Fbp1's metabolic function.

Structural and mechanistic parallels in human CTLH E3

To determine whether structural principles governing activity of the yeast GID E3 are conserved in higher eukaryotes, we studied the human CTLH complex, whose subunits mirror those of Chelator-GID^{SR4} (Figure 6A).

We first reconstituted a recombinant complex that we call "CTLH^{SR4}," which parallels yeast GID^{SR4}. A low-resolution cryo-EM envelope showed that the corresponding human subunits form SRS (hGid4-ARMC8-RANBP9-TWA1) and Cat (RMND5A-MAEA) modules (Figure S6A). As for yeast GID^{SR4} (Qiao et al., 2020), the CTLH^{SR4} Cat module is relatively poorly resolved, but the coordinates for the yeast Gid2-Gid9 subcomplex derived from Chelator-GID^{SR4} readily fit in the density. A 3.2-Å-resolution map obtained by focused refinement enabled building of atomic coordinates for the human SRS module, which superimposes on its yeast counterpart (Figures 6B, S6B and S7; Table S1).

We tested whether the structural conservation extended to the enzymatic mechanism. Because the Pro/N-end degron targets of the CTLH E3 remain unknown, we generated a model peptide substrate: an N-terminal PGLW sequence reported previously to optimally bind hGid4 (Dong et al., 2018, 2020), connected via a flexible linker to a C-terminal target lysine. With this peptide substrate, we tested the effects of structure-based point mutations on ubiquitylation. The hGid4 residues mediating its incorporation into CTLH^{SR4} and RMND5A and MAEA residues that activate UBE2H~Ub are crucial for peptide substrate ubiquitylation (Figures S6C–S6H). Moreover, as with GID^{SR4} (Qiao et al., 2020), only K48 of all Ub lysines was sufficient to support polyUb chain

formation by CTLH^{SR4}, albeit to a substantially lesser degree than WT Ub (Figure S6I). Thus, it seems that the human CTLH core module parallels that in yeast GID assemblies.

We examined by cryo-EM whether the human Gid7 orthologs WDR26 and MKLN1 have capacity for supramolecular assembly. We obtained reconstructions for two subcomplexes containing WDR26. Coexpressing WDR26 with scaffolding and catalytic subunits (ARMC8-RANBP9-TWA1-RMND5A-MAEA) yielded a complex broadly resembling Chelator-GID^{SR4} in that it forms a hollow oval of similar dimensions (Figures 6A and 6C). Docking structures of human and yeast subcomplexes into the density showed that a WDR26 dimer is the SA module. However, WDR26 binds directly to RANBP9-TWA1 in the scaffold, without duplicates of these subunits corresponding to yeast Gid1^{SA}-Gid8^{SA}. The distinct WDR26-dependent supramolecular assembly places four—not two—ARMC8 subunits poised to each bind a hGid4 to capture substrate degrons in the CTLH oval.

The distinctive arrangement of SA and SRS modules was preserved in a 6-Å resolution map of WDR26, RANBP9, TWA1, ARMC8, hGid4, and the poorly understood CTLH subunit YPEL5 (Figure 6C; Table S1). Interestingly, YPEL5 binds at the junction of the two protomers in the WDR26 double-propeller domain.

A low-resolution map showed yet another SA for another human Gid7 ortholog, MKLN1, bound to the CTLH SRS module (Figure 6D; Table S1). Like WDR26, MKLN1 binds directly to RANBP9-TWA1 in the scaffold without intervening duplicates of these subunits. However, in accordance with previous studies (Delto et al., 2015; Kim et al., 2014), MKLN1 forms a tetramer. Four MKLN1 protomers bind between two CTLH SRS modules, demonstrating potential for even higher-order CTLH complex assemblies.

We confirmed roles of WDR26 and MKLN1 in human CTLH complex assembly by sedimentation analyses of lysates from K562 cells or lines in which the human Gid7 orthologs were deleted. Immunoblotting of fractions from sucrose density gradients of parental K562 cell lysates showed comigration of CTLH subunits, corresponding to a complex with a molecular weight greater than that predicted for a uniformly stoichiometric assembly (600–800 kDa according to standards) (Figure 6E). However, probing migration of the core subunit RANBP9 as a marker for the CTLH complex showed that the assembly changes markedly, toward fractions of 150–350 kDa, in CRISPR-Cas9 genome-edited lines lacking WDR26, MKLN1, or both or the Cat module subunit MAEA (Figures 6F and S6J). Interestingly, migration of WDR26 and MKLN1 in higher-molecular-weight fractions is not interdependent (Figure 6G), possibly indicating that each Gid7 ortholog can reside in distinct CTLH assemblies. Much of the total CTLH population shifted to lower-molecular-weight fractions upon deletion of WDR26, with a lesser effect of deleting MKLN1. This may suggest that a greater proportion of the CTLH complex in these cells depends on WDR26 for supramolecular assembly, perhaps because of a higher relative concentration of WDR26 or factors differentially regulating WDR26 or MKLN1 assembly into CTLH complexes.

Overall, the results suggest that CTLH E3 assemblies contain SRS, Cat, and SA modules with features resembling those of Chelator-GID^{SR4}. Moreover, differences in structural configuration of complexes containing MKLN1 or WDR26 offer prospects

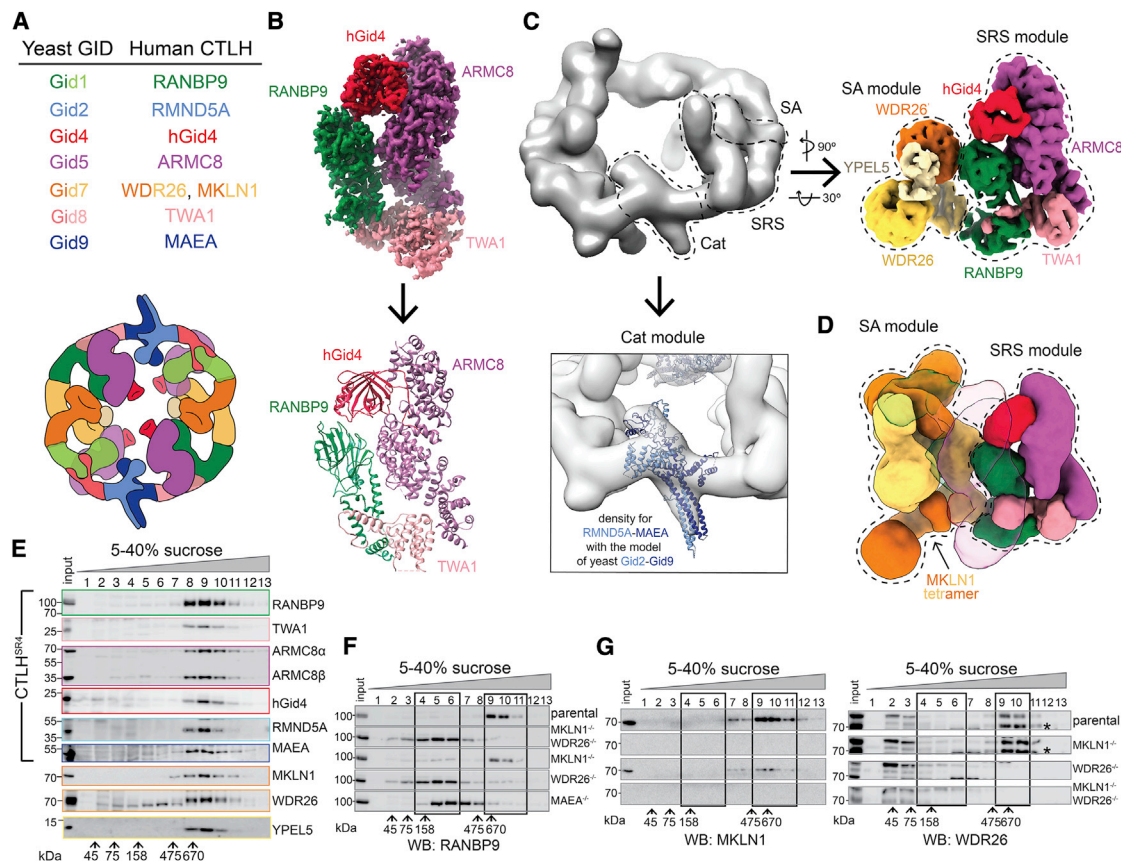


Figure 6. Higher-order assemblies of human CTLH E3

(A) Color-coded guide to yeast GID subunits and their human orthologs in the CTLH complex (top). Two colors indicate multiple protomers of a subunit. Cartoon colored as in the top, representing CTLH oval assembly where the SA module is the WDR26-YPEL5 dimer (bottom).

(B) 3.2-Å-resolution segmented map of CTLH SRS module (RANBP9-TWA1-ARMC8-hGid4) obtained by focused refinement of CTLH^{SR4} (top) and its corresponding model (bottom).

(C) Cryo-EM maps of CTLH assemblies containing the Cat (RMND5A-MAEA), SRS (RANBP9-TWA1-ARMC8 alone or bound to hGid4), and/or supramolecular assembly (WDR26 with or without YPEL5) modules, as indicated. Subunits are colored according to the guide in (A). Top left: low-resolution map of WDR26-mediated SA of CTLH (RANBP9-TWA1-ARMC8-MAEA-RMND5A-WDR26). Right: 6.5-Å-resolution map of the human CTLH SRS module (RANBP9-TWA1-ARMC8-hGid4) sub-complex with an SA module comprising WDR26-YPEL5. Bottom panel: the yeast Gid2-Gid9 structure in the corresponding CTLH Cat module.

(D) 10.4-Å-resolution map of the human CTLH SRS module with MKLN1 as the SA module. The second copy of the SRS module in the subcomplex is transparent.

(E) Immunoblots of fractions from sucrose gradients of K562 cell lysates, probed with the indicated antibodies.

(F) Immunoblots probing for the core CTLH subunit (RANBP9) in fractions from sucrose gradients of lysates from parental K562 and WDR26^{-/-}/MKLN1^{-/-}, MKLN1^{-/-}, WDR26^{-/-}, and MAEA^{-/-} knockout cells. Black boxes delineate high- and low-molecular weight (MW) peak fractions.

(G) As in (F) but probed as indicated with anti-MKLN1 or -WDR26 antibodies. *, WDR26 band.

See also [Figures S6](#) and [S7](#) and [Table S1](#).

that CTLH may adopt a variety of supramolecular E3 assemblies that could impart distinct functionalities.

DISCUSSION

Here we discovered multipronged substrate targeting by an E3 ligase chelate supramolecular assembly tailored to the oligomeric quaternary structure of its metabolic enzyme substrate. In the absence of chelate assembly, GID^{SR4} is a competent E3 ligase that can bind a substrate degron, activate the intrinsic reactivity of its E2 partner (the Ubc8~Ub intermediate), and promote Ub transfer from Ubc8 to a recruited substrate (Qiao et al., 2020). GID^{SR4} is also competent *in vivo* insofar as Gid7

is not required for glucose- and GID-dependent degradation of several substrates (Figure 1). Instead of binding directly to its specified substrate Fbp1, Gid7 alters the GID assembly (Figures 2 and 3).

Although other E3s have been reported to self-assemble (Balaji and Hoppe, 2020), this is typically achieved by catalytic or substrate receptor subunits; for example, the dimeric RING domains of single-subunit E3s or dimeric F-box and BTB substrate receptors in multisubunit cullin-RING ligases (Dou et al., 2012; McMahon et al., 2006; Ogura et al., 2010; Plechanovová et al., 2012; Welcker et al., 2013; Zhuang et al., 2009). Substrate-bound multivalent E3s can undergo liquid-liquid phase-separation (Bouchard et al., 2018). However, the transformation into

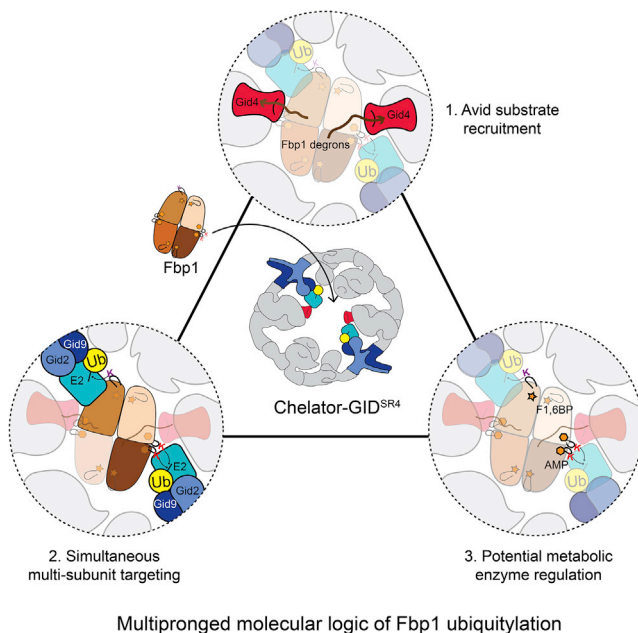


Figure 7. Molecular logic of multipronged Ub targeting of Fbp1 by Chelator-GID^{SR4}

Supramolecular chelate assembly specifies oligomeric metabolic enzyme targeting. (1) Opposing Gid4 subunits avidly bind multiple degrons of tetrameric Fbp1. (2) Opposing RING-E2-Ub active sites simultaneously target specific lysine clusters. (3) Targeted lysines map to metabolically important regions of oligomeric substrate.

Chelator-GID^{SR4} is a distinctive, extreme, and specific adjustment of E3 ligase architecture (Figures 2 and 3).

Resembling an organometallic chelate interacting with its central ligand, Chelator-GID^{SR4}'s multiple distinct points of contact with Fbp1 not only include the degron-binding sites from two opposing Gid4 substrate receptors but also the ubiquitylation active sites from Ubc8~Ub intermediates activated by two opposing Gid2-Gid9 catalytic domains (Figures 4, 5, and 7). Relative to the monodentate GID^{SR4}, the Chelator-GID^{SR4} assembly enables more molecules within the Fbp1 tetramer to be ubiquitylated simultaneously, increasing Ub density on a given Fbp1 tetramer (Figures 1A and 1B). Interestingly, there is not a 1:1 correspondence between the number of degron binding sites in Chelator-GID^{SR4} and the number of degrons in Fbp1. The Fbp1 tetramer has four exposed potential degrons, two on each side, both seemingly poised to capture one central-facing Gid4 in Chelator-GID^{SR4} (Figure 4C). An excess number of degrons is reminiscent of substrates recruited to the cullin-RING ligase receptor Cdc4, whose single binding site can continually and dynamically sample multiple degrons (Mittag et al., 2008). For Chelator-GID^{SR4}-bound Fbp1, we speculate that the arrangement of degrons allows their rapid interchange. This could potentially mediate switching between the promoters positioned adjacent to the active sites.

The human CTLH E3 complex displays striking parallels to Chelator-GID^{SR4}, albeit with interesting twists. In particular, the different Gid7 orthologs form distinct supramolecular assem-

blies (Figure 6). We speculate that the unique assemblies define distinct functions, as implied by varying phenotypic alterations upon their individual mutation (Bauer et al., 2018; Nassan et al., 2017; Skraban et al., 2017; Zhen et al., 2020).

Taken together with previous data (Lampert et al., 2018; Qiao et al., 2020), it is now clear that there is not a single yeast GID or human CTLH complex. Rather, GID and CTLH are examples of responsive systems of multiprotein assemblies with an active E3 core that can be elaborated by supramolecular assembly. Although the function of one such assembly is shown here, the variations revealed by human Gid7 orthologs suggest that they, and presumably other subunits, also co-configure substrate binding and ubiquitylation active sites in accordance with the molecular organization and quaternary structure of particular substrates. The Chelator model presented here demonstrates how GID (and presumably CTLH) utilizes an elegant molecular logic: the response to a signal such as glucose availability converges on numerous aspects of its substrate's structure and function to achieve precise physiological regulation (Figure 7).

Limitations

Chelator-GID^{SR4} is remarkably specific in ubiquitylating particular Fbp1 lysines in metabolic regulatory regions. However, the physiological roles of Fbp1 ubiquitylation impairing allosteric regulation and metabolic function are unknown. Future studies will be required to determine how metabolic flux is coupled with GID-dependent ubiquitylation during termination of gluconeogenesis.

Although Chelator-GID^{SR4} is active toward Mdh2 and Pck1, it is unclear why these oligomeric substrates are less dependent than Fbp1 on Gid7-mediated supramolecular assembly. One speculative possibility could be that any potential advantage of avid binding is offset by accessibility of numerous ubiquitylation sites to GID^{SR4}. Future studies will be required to understand how Pck1 and other GID E3 substrates, including the Gid4 substrate receptor itself, are recognized and ubiquitylated (Hämmerle et al., 1998; Karayel et al., 2020; Menssen et al., 2018).

Finally, although discovery of the Chelator configuration provides a basis for understanding higher-order GID assembly, what other assemblies or sub-assemblies may form and their functions remain unknown. Clearly, other arrangements are observed for human CTLH complexes with WDR26. MKLN1 forms an even higher-order assembly with the human SRS module. Some yeast GID assemblies migrate in the void volume, as seen by size-exclusion chromatography (Figure S2A). Moreover, the mechanistic roles of additional subunits, including YPEL5 (Figure 6), or regulatory partners, such as Cdc48/p97, remain unknown (Barbin et al., 2010; Lampert et al., 2018). We await future studies revealing functions of other variations of GID and CTLH assemblies.

STAR★METHODS

Detailed methods are provided in the online version of this paper and include the following:

- [KEY RESOURCES TABLE](#)
- [RESOURCE AVAILABILITY](#)

- Lead contact
- Materials availability
- Data and code availability

● **METHOD DETAILS**

- Yeast strain construction and growth conditions
- *In vivo* yeast substrate degradation assays
- Purification of endogenous yeast Gid for cryo EM
- Sucrose gradient fractionation of yeast lysates (Figure S2C)
- *In vivo* Fbp1 ubiquitylation assay (Figure 1E)
- Plasmid preparation and Mutagenesis
- Insect cell expression and purification of GID/CTLH complexes
- Bacterial expression and purification
- *In vitro* biochemical assays
- Biochemical assays with yeast GID
- Determination of kinetic parameters of Fbp1 ubiquitylation by GID E3
- Biochemical assays with human CTLH^{SR4}
- SEC for initial characterization of GID supramolecular assembly
- SEC-MALS
- Fbp1 enzyme activity assay
- Analysis of global proteome of WT versus Δ Gid7 yeast (Karayel et al., 2020)
- Determination of preferentially targeted lysines in Fbp1 by LC-MS/MS (Figure S5)
- Cell culture and generation of CRISPR-Cas9 knock out cell lines
- Human cell lysate fractionation by sucrose density gradient
- Cryo EM sample preparation and Imaging
- Cryo EM data processing
- Model building and refinement
- Fbp1 crystallization and data processing

● **QUANTIFICATION AND STATISTICAL ANALYSIS**

SUPPLEMENTAL INFORMATION

Supplemental information can be found online at <https://doi.org/10.1016/j.molcel.2021.03.025>.

ACKNOWLEDGMENTS

We thank A. Varshavsky for promoter reference plasmids; S. Übel and S. Peltera for peptide synthesis; D. Bollschweiler, T. Schäfer, J. Basquin, K. Valer-Saldana, and S. Pleyer for assistance with cryo-EM and crystallography; Swiss Light Source, Villigen, Switzerland for Fbp1 crystal data collection; M. Strauss for assistance with initial negative-stain data collection on the yeast Chelator-GID complex; M. Yamaguchi for Gid7 constructs; G. Kleiger for guidance regarding kinetics; I. Paron for technical assistance with mass spectrometry; and K. Baek, B. Bräuning, and the Schulman lab for advice and support. The B.A.S. lab is funded by the Leibniz Prize from Deutsche Forschungsgemeinschaft (SCHU 3196/1-1). B.A.S. and M.M. are supported by the Max Planck Society.

AUTHOR CONTRIBUTIONS

Initial conceptualization, D.S., J.C., and B.A.S.; methodology, D.S., J.C., J.R.P., C.R.L., O.K., A.F.A., and B.A.S.; investigation, D.S., J.C., S.Q., C.R.L., L.A.H., K.V.G., F.M.H., O.K., J.R.P., and A.F.A.; resources, D.S.,

J.C., K.V.G., C.R.L., S.v.G., and A.F.A.; writing – original draft, D.S., J.C., and B.A.S.; writing – review & editing, D.S., J.C., C.R.L., A.F.A., and B.A.S.; supervision, M.M., A.F.A., and B.A.S.; funding acquisition, M.M. and B.A.S.

DECLARATION OF INTERESTS

B.A.S. is an honorary professor at Technical University of Munich, Germany and adjunct faculty at St. Jude Children's Research Hospital, Memphis, TN, USA and is on the scientific advisory board of Interline Therapeutics.

Received: October 15, 2020

Revised: February 17, 2021

Accepted: March 17, 2021

Published: April 26, 2021

REFERENCES

- Adams, P.D., Afonine, P.V., Bunkóczi, G., Chen, V.B., Davis, I.W., Echols, N., Headd, J.J., Hung, L.W., Kapral, G.J., Grosse-Kunstleve, R.W., et al. (2010). PHENIX: a comprehensive Python-based system for macromolecular structure solution. *Acta Crystallogr. D Biol. Crystallogr.* 66, 213–221.
- Afonine, P.V., Klaholz, B.P., Moriarty, N.W., Poon, B.K., Sobolev, O.V., Terwilliger, T.C., Adams, P.D., and Urzhumtsev, A. (2018). New tools for the analysis and validation of cryo-EM maps and atomic models. *Acta Crystallogr. D Struct. Biol.* 74, 814–840.
- Baek, K., Krist, D.T., Prabu, J.R., Hill, S., Klügel, M., Neumaier, L.M., von Gronau, S., Kleiger, G., and Schulman, B.A. (2020). NEDD8 nucleates a multi-valent cullin-RING-UBE2D ubiquitin ligation assembly. *Nature* 578, 461–466.
- Balaji, V., and Hoppe, T. (2020). Regulation of E3 ubiquitin ligases by homotypic and heterotypic assembly. *F1000Res.* 9, F1000 Faculty Rev-88.
- Barbin, L., Eisele, F., Santt, O., and Wolf, D.H. (2010). The Cdc48-Ufd1-Npl4 complex is central in ubiquitin-proteasome triggered catabolite degradation of fructose-1,6-bisphosphatase. *Biochem. Biophys. Res. Commun.* 394, 335–341.
- Barford, D. (2020). Structural interconversions of the anaphase-promoting complex/cyclosome (APC/C) regulate cell cycle transitions. *Curr. Opin. Struct. Biol.* 61, 86–97.
- Bauer, A., Jagannathan, V., Högl, S., Richter, B., McEwan, N.A., Thomas, A., Cadieu, E., André, C., Hytönen, M.K., Lohi, H., et al. (2018). MKLN1 splicing defect in dogs with lethal acrodermatitis. *PLoS Genet.* 14, e1007264.
- Biyani, N., Righetto, R.D., McLeod, R., Caujolle-Bert, D., Castano-Diez, D., Goldie, K.N., and Stahlberg, H. (2017). Focus: The interface between data collection and data processing in cryo-EM. *J. Struct. Biol.* 198, 124–133.
- Boldt, K., van Reeuwijk, J., Lu, Q., Koutroumpas, K., Nguyen, T.M., Texier, Y., van Beersum, S.E., Horn, N., Willer, J.R., Mans, D.A., et al.; UK10K Rare Diseases Group (2016). An organelle-specific protein landscape identifies novel diseases and molecular mechanisms. *Nat. Commun.* 7, 11491.
- Bouchard, J.J., Otero, J.H., Scott, D.C., Szulc, E., Martin, E.W., Sabri, N., Granata, D., Marzahn, M.R., Lindorff-Larsen, K., Salvatella, X., et al. (2018). Cancer Mutations of the Tumor Suppressor SPOP Disrupt the Formation of Active, Phase-Separated Compartments. *Mol. Cell* 72, 19–36.e8.
- Braun, B., Pfirrmann, T., Menssen, R., Hofmann, K., Scheel, H., and Wolf, D.H. (2011). Gid9, a second RING finger protein contributes to the ubiquitin ligase activity of the Gid complex required for catabolite degradation. *FEBS Lett.* 585, 3856–3861.
- Brown, N.G., VanderLinden, R., Watson, E.R., Weissmann, F., Ordureau, A., Wu, K.P., Zhang, W., Yu, S., Mercedi, P.Y., Harrison, J.S., et al. (2016). Dual RING E3 Architectures Regulate Multiubiquitination and Ubiquitin Chain Elongation by APC/C. *Cell* 165, 1440–1453.
- Budhidarmo, R., Nakatani, Y., and Day, C.L. (2012). RINGs hold the key to ubiquitin transfer. *Trends Biochem. Sci.* 37, 58–65.
- Burnley, T., Palmer, C.M., and Winn, M. (2017). Recent developments in the CCP-EM software suite. *Acta Crystallogr. D Struct. Biol.* 73, 469–477.

- Cao, W.X., Kabelitz, S., Gupta, M., Yeung, E., Lin, S., Rammelt, C., Ihling, C., Pekovic, F., Low, T.C.H., Siddiqui, N.U., et al. (2020). Precise Temporal Regulation of Post-transcriptional Repressors Is Required for an Orderly *Drosophila* Maternal-to-Zygotic Transition. *Cell Rep.* **37**, 107783.
- Chen, V.B., Arendall, W.B., 3rd, Headd, J.J., Keedy, D.A., Immormino, R.M., Kapral, G.J., Murray, L.W., Richardson, J.S., and Richardson, D.C. (2010). MolProbity: all-atom structure validation for macromolecular crystallography. *Acta Crystallogr. D Biol. Crystallogr.* **66**, 12–21.
- Chen, C.K., Chan, N.L., and Wang, A.H. (2011a). The many blades of the β -propeller proteins: conserved but versatile. *Trends Biochem. Sci.* **36**, 553–561.
- Chen, I., Dorr, B.M., and Liu, D.R. (2011b). A general strategy for the evolution of bond-forming enzymes using yeast display. *Proc. Natl. Acad. Sci. USA* **108**, 11399–11404.
- Chen, S., Wu, J., Lu, Y., Ma, Y.B., Lee, B.H., Yu, Z., Ouyang, Q., Finley, D.J., Kirschner, M.W., and Mao, Y. (2016). Structural basis for dynamic regulation of the human 26S proteasome. *Proc. Natl. Acad. Sci. USA* **113**, 12991–12996.
- Chen, S.J., Wu, X., Wadas, B., Oh, J.H., and Varshavsky, A. (2017). An N-end rule pathway that recognizes proline and destroys gluconeogenic enzymes. *Science* **355**, eaal3655.
- Chiang, H.L., and Schekman, R. (1991). Regulated import and degradation of a cytosolic protein in the yeast vacuole. *Nature* **350**, 313–318.
- Cong, L., Ran, F.A., Cox, D., Lin, S., Barretto, R., Habib, N., Hsu, P.D., Wu, X., Jiang, W., Marraffini, L.A., and Zhang, F. (2013). Multiplex genome engineering using CRISPR/Cas systems. *Science* **339**, 819–823.
- Cowtan, K. (2006). The Buccaneer software for automated model building. 1. Tracing protein chains. *Acta Crystallogr. D Biol. Crystallogr.* **62**, 1002–1011.
- Delto, C.F., Heisler, F.F., Kuper, J., Sander, B., Kneussel, M., and Schindelin, H. (2015). The LisH motif of muskelin is crucial for oligomerization and governs intracellular localization. *Structure* **23**, 364–373.
- DiMaio, F., Echols, N., Headd, J.J., Terwilliger, T.C., Adams, P.D., and Baker, D. (2013). Improved low-resolution crystallographic refinement with Phenix and Rosetta. *Nat. Methods* **10**, 1102–1104.
- Dong, C., Zhang, H., Li, L., Tempel, W., Loppnau, P., and Min, J. (2018). Molecular basis of GID4-mediated recognition of degrons for the Pro/N-end rule pathway. *Nat. Chem. Biol.* **14**, 466–473.
- Dong, C., Chen, S.J., Melnykov, A., Weirich, S., Sun, K., Jeltsch, A., Varshavsky, A., and Min, J. (2020). Recognition of nonproline N-terminal residues by the Pro/N-degron pathway. *Proc. Natl. Acad. Sci. USA* **117**, 14158–14167.
- Dou, H., Buetow, L., Sibbet, G.J., Cameron, K., and Huang, D.T. (2012). BIRC7-E2 ubiquitin conjugate structure reveals the mechanism of ubiquitin transfer by a RING dimer. *Nat. Struct. Mol. Biol.* **19**, 876–883.
- Emsley, P., and Cowtan, K. (2004). Coot: model-building tools for molecular graphics. *Acta Crystallogr. D Biol. Crystallogr.* **60**, 2126–2132.
- Emsley, P., Lohkamp, B., Scott, W.G., and Cowtan, K. (2010). Features and development of Coot. *Acta Crystallogr. D Biol. Crystallogr.* **66**, 486–501.
- Fernandez-Leiro, R., and Scheres, S.H.W. (2017). A pipeline approach to single-particle processing in RELION. *Acta Crystallogr. D Struct. Biol.* **73**, 496–502.
- Francis, O., Han, F., and Adams, J.C. (2013). Molecular phylogeny of a RING E3 ubiquitin ligase, conserved in eukaryotic cells and dominated by homologous components, the muskelin/RanBPM/CTLH complex. *PLoS ONE* **8**, e75217.
- Gancedo, C. (1971). Inactivation of fructose-1,6-diphosphatase by glucose in yeast. *J. Bacteriol.* **107**, 401–405.
- Gibson, D.G., Young, L., Chuang, R.Y., Venter, J.C., Hutchison, C.A., 3rd, and Smith, H.O. (2009). Enzymatic assembly of DNA molecules up to several hundred kilobases. *Nat. Methods* **6**, 343–345.
- Goddard, T.D., Huang, C.C., Meng, E.C., Pettersen, E.F., Couch, G.S., Morris, J.H., and Ferrin, T.E. (2018). UCSF ChimeraX: Meeting modern challenges in visualization and analysis. *Protein Sci.* **27**, 14–25.
- Hämmerle, M., Bauer, J., Rose, M., Szallies, A., Thumm, M., Düsterhus, S., Mecke, D., Entian, K.D., and Wolf, D.H. (1998). Proteins of newly isolated mutants and the amino-terminal proline are essential for ubiquitin-proteasome-catalyzed catabolite degradation of fructose-1,6-bisphosphatase of *Saccharomyces cerevisiae*. *J. Biol. Chem.* **273**, 25000–25005.
- Haselbach, D., Schrader, J., Lambrecht, F., Henneberg, F., Chari, A., and Stark, H. (2017). Long-range allosteric regulation of the human 26S proteasome by 20S proteasome-targeting cancer drugs. *Nat. Commun.* **8**, 15578.
- Janke, C., Magiera, M.M., Rathfelder, N., Taxis, C., Reber, S., Maekawa, H., Moreno-Borchart, A., Doenges, G., Schwob, E., Schiebel, E., and Knop, M. (2004). A versatile toolbox for PCR-based tagging of yeast genes: new fluorescent proteins, more markers and promoter substitution cassettes. *Yeast* **Aug**;21(11).
- Kaiser, S.E., Riley, B.E., Shaler, T.A., Trevino, R.S., Becker, C.H., Schulman, H., and Kopito, R.R. (2011). Protein standard absolute quantification (PSAQ) method for the measurement of cellular ubiquitin pools. *Nat. Methods* **8**, 691–696.
- Karayel, O., Michaelis, A.C., Mann, M., Schulman, B.A., and Langlois, C.R. (2020). DIA-based systems biology approach unveils E3 ubiquitin ligase-dependent responses to a metabolic shift. *Proc. Natl. Acad. Sci. USA* **117**, 32806–32815.
- Ke, H.M., Thorpe, C.M., Seaton, B., Lipscomb, W.N., and Marcus, F. (1990a). Structure refinement of fructose-1,6-bisphosphatase and its fructose 2,6-bisphosphate complex at 2.8 Å resolution. *J. Mol. Biol.* **212**, 513–539.
- Ke, H.M., Zhang, Y.P., and Lipscomb, W.N. (1990b). Crystal structure of fructose-1,6-bisphosphatase complexed with fructose 6-phosphate, AMP, and magnesium. *Proc. Natl. Acad. Sci. USA* **87**, 5243–5247.
- Kelley, L.A., Mezulis, S., Yates, C.M., Wass, M.N., and Sternberg, M.J. (2015). The Phyre2 web portal for protein modeling, prediction and analysis. *Nat. Protoc.* **10**, 845–858.
- Kim, K.H., Hong, S.K., Hwang, K.Y., and Kim, E.E. (2014). Structure of mouse muskelin discoidin domain and biochemical characterization of its self-association. *Acta Crystallogr. D Biol. Crystallogr.* **70**, 2863–2874.
- Knop, M., Siegers, K., Pereira, G., Zachariae, W., Winsor, B., Nasmyth, K., and Schiebel, E. (1999). Epitope tagging of yeast genes using a PCR-based strategy: more tags and improved practical routines. *Yeast* **Jul**;15(10B).
- Kobayashi, N., Yang, J., Ueda, A., Suzuki, T., Tomaru, K., Takeno, M., Okuda, K., and Ishigatsubo, Y. (2007). RanBPM, Muskelin, p48EMLP, p44CTLH, and the armadillo-repeat proteins ARMC8alpha and ARMC8beta are components of the CTLH complex. *Gene* **396**, 236–247.
- Koshland, D.E., Jr. (1963a). Correlation of Structure and Function in Enzyme Action. *Science* **142**, 1533–1541.
- Koshland, D.E., Jr. (1963b). Properties of the active site of enzymes. *Ann. N Y Acad. Sci.* **103**, 630–642.
- Kulak, N.A., Pichler, G., Paron, I., Nagaraj, N., and Mann, M. (2014). Minimal, encapsulated proteomic-sample processing applied to copy-number estimation in eukaryotic cells. *Nat. Methods* **11**, 319–324.
- Lampert, F., Stafa, D., Goga, A., Soste, M.V., Gilberto, S., Olieric, N., Picotti, P., Stoffel, M., and Peter, M. (2018). The multi-subunit GID/CTLH E3 ubiquitin ligase promotes cell proliferation and targets the transcription factor Hbp1 for degradation. *eLife* **7**, e35528.
- Lander, G.C., Estrin, E., Matyskiela, M.E., Bashore, C., Nogales, E., and Martin, A. (2012). Complete subunit architecture of the proteasome regulatory particle. *Nature* **482**, 186–191.
- Leggett, D.S., Hanna, J., Borodovsky, A., Crosas, B., Schmidt, M., Baker, R.T., Walz, T., Ploegh, H., and Finley, D. (2002). Multiple associated proteins regulate proteasome structure and function. *Mol. Cell* **10**, 495–507.
- Liu, H., and Pfirrmann, T. (2019). The Gid-complex: an emerging player in the ubiquitin ligase league. *Biol. Chem.* **400**, 1429–1441.
- Liu, H., Ding, J., Köhnlein, K., Urban, N., Ori, A., Villavicencio-Lorini, P., Walentek, P., Klotz, L.O., Hollemann, T., and Pfirrmann, T. (2020). The GID ubiquitin ligase complex is a regulator of AMPK activity and organismal lifespan. *Autophagy* **16**, 1618–1634.

- Maitland, M.E.R., Onea, G., Chiasson, C.A., Wang, X., Ma, J., Moor, S.E., Barber, K.R., Lajoie, G.A., Shaw, G.S., and Schild-Poulter, C. (2019). The mammalian CTLH complex is an E3 ubiquitin ligase that targets its subunit muskellin for degradation. *Sci. Rep.* **9**, 9864.
- Mastronarde, D. (2003). SerialEM: A Program for Automated Tilt Series Acquisition on Tecnai Microscopes Using Prediction of Specimen Position. *Microsc. Microanal.* **9**, 1182–1183.
- McMahon, M., Thomas, N., Itoh, K., Yamamoto, M., and Hayes, J.D. (2006). Dimerization of substrate adaptors can facilitate cullin-mediated ubiquitylation of proteins by a “tethering” mechanism: a two-site interaction model for the Nrf2-Keap1 complex. *J. Biol. Chem.* **281**, 24756–24768.
- Melnykov, A., Chen, S.J., and Varshavsky, A. (2019). Gid10 as an alternative N-recognin of the Pro/N-degron pathway. *Proc. Natl. Acad. Sci. USA* **116**, 15914–15923.
- Menssen, R., Schweiggert, J., Schreiner, J., Kusevic, D., Reuther, J., Braun, B., and Wolf, D.H. (2012). Exploring the topology of the Gid complex, the E3 ubiquitin ligase involved in catabolite-induced degradation of gluconeogenic enzymes. *J. Biol. Chem.* **287**, 25602–25614.
- Menssen, R., Bui, K., and Wolf, D.H. (2018). Regulation of the Gid ubiquitin ligase recognition subunit Gid4. *FEBS Lett.* **592**, 3286–3294.
- Mittag, T., Orlicky, S., Choy, W.Y., Tang, X., Lin, H., Sicheri, F., Kay, L.E., Tyers, M., and Forman-Kay, J.D. (2008). Dynamic equilibrium engagement of a polyvalent ligand with a single-site receptor. *Proc. Natl. Acad. Sci. USA* **105**, 17772–17777.
- Monod, J., Changeux, J.P., and Jacob, F. (1963). Allosteric proteins and cellular control systems. *J. Mol. Biol.* **6**, 306–329.
- Nakatsukasa, K., Okumura, F., and Kamura, T. (2015). Proteolytic regulation of metabolic enzymes by E3 ubiquitin ligase complexes: lessons from yeast. *Crit. Rev. Biochem. Mol. Biol.* **50**, 489–502.
- Nassan, M., Li, Q., Croarkin, P.E., Chen, W., Colby, C.L., Veldic, M., McElroy, S.L., Jenkins, G.D., Ryu, E., Cunningham, J.M., et al. (2017). A genome wide association study suggests the association of muskellin with early onset bipolar disorder: Implications for a GABAergic epileptogenic neurogenesis model. *J. Affect. Disord.* **208**, 120–129.
- Nayak, D., and Sivaraman, J. (2018). Structure of LNX1:Ubc13~Ubiquitin Complex Reveals the Role of Additional Motifs for the E3 Ligase Activity of LNX1. *J. Mol. Biol.* **430**, 1173–1188.
- Ogura, T., Tong, K.I., Mio, K., Maruyama, Y., Kurokawa, H., Sato, C., and Yamamoto, M. (2010). Keap1 is a forked-stem dimer structure with two large spheres enclosing the intervening, double glycine repeat, and C-terminal domains. *Proc. Natl. Acad. Sci. USA* **107**, 2842–2847.
- Oh, J.H., Chen, S.J., and Varshavsky, A. (2017). A reference-based protein degradation assay without global translation inhibitors. *J. Biol. Chem.* **292**, 21457–21465.
- Pettersen, E.F., Goddard, T.D., Huang, C.C., Couch, G.S., Greenblatt, D.M., Meng, E.C., and Ferrin, T.E. (2004). UCSF Chimera—a visualization system for exploratory research and analysis. *J. Comput. Chem.* **25**, 1605–1612.
- Plechanová, A., Jaffray, E.G., Tatham, M.H., Nismith, J.H., and Hay, R.T. (2012). Structure of a RING E3 ligase and ubiquitin-loaded E2 primed for catalysis. *Nature* **489**, 115–120.
- Pruneda, J.N., Littlefield, P.J., Soss, S.E., Nordquist, K.A., Chazin, W.J., Brzovic, P.S., and Klevit, R.E. (2012). Structure of an E3:E2~Ub complex reveals an allosteric mechanism shared among RING/U-box ligases. *Mol. Cell* **47**, 933–942.
- Qiao, S., Langlois, C.R., Chrustowicz, J., Sherpa, D., Karayel, O., Hansen, F.M., Beier, V., von Gronau, S., Bollschweiler, D., Schäfer, T., et al. (2020). Interconversion between Anticipatory and Active GID E3 Ubiquitin Ligase Conformations via Metabolically Driven Substrate Receptor Assembly. *Mol. Cell* **77**, 150–163.e9.
- Regelmann, J., Schüle, T., Josupeit, F.S., Horak, J., Rose, M., Entian, K.D., Thumm, M., and Wolf, D.H. (2003). Catabolite degradation of fructose-1,6-bisphosphatase in the yeast *Saccharomyces cerevisiae*: a genome-wide screen identifies eight novel GID genes and indicates the existence of two degradation pathways. *Mol. Biol. Cell* **14**, 1652–1663.
- Rusnac, D.V., and Zheng, N. (2020). Structural Biology of CRL Ubiquitin Ligases. *Adv. Exp. Med. Biol.* **1217**, 9–31.
- Salemi, L.M., Maitland, M.E.R., McTavish, C.J., and Schild-Poulter, C. (2017). Cell signalling pathway regulation by RanBPM: molecular insights and disease implications. *Open Biol.* **7**, 170081.
- Sanchez-Garcia, R., Gomez-Blanco, J., Cuervo, A., Carazo, J., Sorzano, C., and Vargas, J. (2020). DeepEMhancer: a deep learning solution for cryo-EM volume post-processing. *bioRxiv*. <https://doi.org/10.1101/2020.06.12.148296>.
- Santt, O., Pfirrmann, T., Braun, B., Juretschke, J., Kimmig, P., Scheel, H., Hofmann, K., Thumm, M., and Wolf, D.H. (2008). The yeast GID complex, a novel ubiquitin ligase (E3) involved in the regulation of carbohydrate metabolism. *Mol. Biol. Cell* **19**, 3323–3333.
- Scheres, S.H. (2012). RELION: implementation of a Bayesian approach to cryo-EM structure determination. *J. Struct. Biol.* **180**, 519–530.
- Schindelin, J., Arganda-Carreras, I., Frise, E., Kaynig, V., Longair, M., Pietzsch, T., Preibisch, S., Rueden, C., Saalfeld, S., Schmid, B., et al. (2012). Fiji: an open-source platform for biological-image analysis. *Nat. Methods* **9**, 676–682.
- Schork, S.M., Bee, G., Thumm, M., and Wolf, D.H. (1994a). Catabolite inactivation of fructose-1,6-bisphosphatase in yeast is mediated by the proteasome. *FEBS Lett.* **349**, 270–274.
- Schork, S.M., Bee, G., Thumm, M., and Wolf, D.H. (1994b). Site of catabolite inactivation. *Nature* **369**, 283–284.
- Schork, S.M., Thumm, M., and Wolf, D.H. (1995). Catabolite inactivation of fructose-1,6-bisphosphatase of *Saccharomyces cerevisiae*. Degradation occurs via the ubiquitin pathway. *J. Biol. Chem.* **270**, 26446–26450.
- Schweitzer, A., Aufderheide, A., Rudack, T., Beck, F., Pfeifer, G., Plietzko, J.M., Sakata, E., Schulten, K., Förster, F., and Baumeister, W. (2016). Structure of the human 26S proteasome at a resolution of 3.9 Å. *Proc. Natl. Acad. Sci. USA* **113**, 7816–7821.
- Shakeel, S., Rajendra, E., Alcón, P., O’Reilly, F., Chorev, D.S., Maslen, S., Degliesposti, G., Russo, C.J., He, S., Hill, C.H., et al. (2019). Structure of the Fanconi anaemia monoubiquitin ligase complex. *Nature* **575**, 234–237.
- Skraban, C.M., Wells, C.F., Markose, P., Cho, M.T., Nesbitt, A.I., Au, P.Y.B., Begtrup, A., Bernat, J.A., Bird, L.M., Cao, K., et al. (2017). WDR26 Haploinsufficiency Causes a Recognizable Syndrome of Intellectual Disability, Seizures, Abnormal Gait, and Distinctive Facial Features. *Am. J. Hum. Genet.* **101**, 139–148.
- Storici, F., and Resnick, M.A. (2006). The delitto perfetto approach to in vivo site-directed mutagenesis and chromosome rearrangements with synthetic oligonucleotides in yeast. *Methods Enzymology* **409**.
- Tu, B.P., and McKnight, S.L. (2006). Metabolic cycles as an underlying basis of biological oscillations. *Nat. Rev. Mol. Cell Biol.* **7**, 696–701.
- Tyanova, S., Temu, T., Sinitcyn, P., Carlson, A., Hein, M.Y., Geiger, T., Mann, M., and Cox, J. (2016). The Perseus computational platform for comprehensive analysis of (prote)omics data. *Nat. Methods* **13**, 731–740.
- Waterhouse, A., Bertoni, M., Bienert, S., Studer, G., Tauriello, G., Gumienny, R., Heer, F.T., de Beer, T.A.P., Rempfer, C., Bordoli, L., et al. (2018). SWISS-MODEL: homology modelling of protein structures and complexes. *Nucleic Acids Res.* **46** (W1), W296–W303.
- Watson, E.R., Brown, N.G., Peters, J.M., Stark, H., and Schulman, B.A. (2019). Posing the APC/C E3 Ubiquitin Ligase to Orchestrate Cell Division. *Trends Cell Biol.* **29**, 117–134.
- Wehmer, M., Rudack, T., Beck, F., Aufderheide, A., Pfeifer, G., Plietzko, J.M., Förster, F., Schulten, K., Baumeister, W., and Sakata, E. (2017). Structural insights into the functional cycle of the ATPase module of the 26S proteasome. *Proc. Natl. Acad. Sci. USA* **114**, 1305–1310.
- Weissmann, F., Petzold, G., VanderLinden, R., Huis In ’t Veld, P.J., Brown, N.G., Lampert, F., Westermann, S., Stark, H., Schulman, B.A., and Peters, J.M. (2016). biGBac enables rapid gene assembly for the expression of

large multisubunit protein complexes. *Proc. Natl. Acad. Sci. USA* *113*, E2564–E2569.

Welcker, M., Larimore, E.A., Swanger, J., Bengoechea-Alonso, M.T., Grim, J.E., Ericsson, J., Zheng, N., and Clurman, B.E. (2013). Fbw7 dimerization determines the specificity and robustness of substrate degradation. *Genes Dev.* *27*, 2531–2536.

Zaman, S., Lippman, S.I., Zhao, X., and Broach, J.R. (2008). How *Saccharomyces* responds to nutrients. *Annu. Rev. Genet.* *42*, 27–81.

Zavortink, M., Rutt, L.N., Dzitoyeva, S., Henriksen, J.C., Barrington, C., Bilodeau, D.Y., Wang, M., Chen, X.X.L., and Rissland, O.S. (2020). The E2 Marie Kondo and the CTLH E3 ligase clear deposited RNA binding proteins during the maternal-to-zygotic transition. *eLife* *9*, e53889.

Zhang, K. (2016). Gctf: Real-time CTF determination and correction. *J. Struct. Biol.* *193*, 1–12.

Zhen, R., Moo, C., Zhao, Z., Chen, M., Feng, H., Zheng, X., Zhang, L., Shi, J., and Chen, C. (2020). Wdr26 regulates nuclear condensation in developing erythroblasts. *Blood* *135*, 208–219.

Zheng, S.Q., Palovcak, E., Armache, J.P., Verba, K.A., Cheng, Y., and Agard, D.A. (2017). MotionCor2: anisotropic correction of beam-induced motion for improved cryo-electron microscopy. *Nat. Methods* *14*, 331–332.

Zhu, J., and Thompson, C.B. (2019). Metabolic regulation of cell growth and proliferation. *Nat. Rev. Mol. Cell Biol.* *20*, 436–450.

Zhuang, M., Calabrese, M.F., Liu, J., Waddell, M.B., Nourse, A., Hammel, M., Miller, D.J., Walden, H., Duda, D.M., Seyedin, S.N., et al. (2009). Structures of SPOP-substrate complexes: insights into molecular architectures of BTB-Cul3 ubiquitin ligases. *Mol. Cell* *36*, 39–50.

Zivanov, J., Nakane, T., Forsberg, B.O., Kimanius, D., Hagen, W.J., Lindahl, E., and Scheres, S.H. (2018). New tools for automated high-resolution cryo-EM structure determination in RELION-3. *eLife* *7*, e42166.

STAR★METHODS

KEY RESOURCES TABLE

REAGENT or RESOURCE	SOURCE	IDENTIFIER
Antibodies		
Monoclonal ANTI-FLAG M2 antibody	Sigma Aldrich	Cat# F1804; RRID: AB_262044
Anti-HA antibody produced in rabbit	Sigma Aldrich	Cat# H6908; RRID: AB_260070
Goat anti-rabbit IgG Dylight488 conjugated	Invitrogen	Cat# 35552; RRID: AB_844398
Goat anti-mouse IgG Dylight633 conjugated	Invitrogen	Cat# 35512; RRID: AB_1307538
Anti-rabbit peroxidase antibody produced in goat	Sigma Aldrich	Cat# A9169; RRID: AB_258434
Anti-mouse IgG Peroxidase antibody produced in goat	Sigma Aldrich	Cat# A4416; RRID: AB_258167
Anti-His antibody produced in mouse	Cell Signaling Technology	Cat# 9991; RRID: AB_2797714
Goat polyclonal anti-RMND5A antibody	Santa Cruz	Cat# sc-161202, RRID: AB_2181510
Sheep polyclonal anti-MAEA antibody	R&D Systems	Cat# AF7288-SP, RRID: AB_10971438
Rabbit polyclonal anti-RANBP9 antibody	Abnova	Cat# PAB16671; RRID: AB_10677213
Rabbit polyclonal anti-TWA1 antibody	Novus	Cat# NBP1-32596; RRID: AB_2274921
Mouse monoclonal anti-ARMC8 antibody	Santa Cruz	Cat# sc-365307; RRID: AB_10850172
Mouse monoclonal anti-MKLN1 antibody	Santa Cruz	Cat# sc-398956; RRID: AB_2737249
Rabbit polyclonal anti-WDR26 antibody	Bethyl Laboratories	Cat# A302-245A; RRID: AB_1730876
Rabbit polyclonal anti-YPEL5 antibody	Thermo Fisher	Cat# PA5-26957; RRID: AB_2544457
Sheep polyclonal anti-hGid4	This study	N/A
HaloLink Resin	Promega	Cat# G1912
ANTI-FLAG M2 affinity gel	Sigma Aldrich	Cat# A2220
His-Select Nickel affinity gel	Sigma Aldrich	Cat# P6611
Glutathione Sepharose 4B	GE Healthcare	Cat# 17075605
StrepTactin Sepharose High Performance resin	cytiva	Cat# 28935599
His-Halo UBA ^{UBQLN1}	This study	N/A
Critical commercial assays		
EnzChek Phosphate Assay Kit	ThermoFisher Scientific	Cat# E6646
Bacterial and virus strains		
<i>E. coli</i> BL21 RIL (DE3)	MPIB	N/A
<i>E. coli</i> DH5 α	MPIB	N/A
Chemicals, peptides, and recombinant proteins		
complete EDTA free	Roche	Cat# 05056489001
Aprotinin from bovine lung	Sigma	A1153-10MG
Leupeptin	Sigma	L2884-250MG
Benzamidine	Sigma	B6506-25G
GGGGGFYVK-FAM	MPIB	N/A
PTLVNGWPR	MPIB	N/A
PTLVNGPRRDSTEGFTGRGWSGRGWS	MPIB	N/A
KGGK-FAM	MPIB	N/A
PGLWRSPRRDSTEGFTGRGWSGRG	MPIB	N/A
WSKGGK-FAM	MPIB	N/A
3xFLAG peptide	MPIB	N/A

(Continued on next page)

Continued

REAGENT or RESOURCE	SOURCE	IDENTIFIER
Deposited data		
Apo Chelator-GID ^{SR4}	This study	EMDB: EMD-12541
Chelator-GID ^{SR4} + Fbp1	This study	EMDB: EMD-12557
GID ^{SR4}	This study	EMDB: EMD-12548
SRS module	This study	EMDB: EMD-12559; PDB: 7NS3
Cat module	This study	EMDB: EMD-12560; PDB: 7NS4
SA module	This study	EMDB: EMD-12563; PDB: 7NSB
Endogenous GID ^{Ant}	This study	EMDB: EMD-12538
Endogenous Chelator-GID ^{Ant}	This study	EMDB: EMD-12540
CTLH ^{SR4}	This study	EMDB: EMD-12537
CTLH ^{SR4} SRS module	This study	EMDB: EMD-12564; PDB: 7NSC
CTLH-WDR26 SA and SRS modules	This study	EMDB: EMD-12545
CTLH-WDR26 supramolecular assembly	This study	EMDB: EMD-12542
CTLH-MKLN1 SA and SRS modules	This study	EMDB: EMD-12547
Fbp1 (crystal structure)	This study	PDB: 7NS5
Proteomics data	This study	PXD024462
Raw image data	This study	http://dx.doi.org/10.17632/rfpsg6939c.1
Experimental models: Cell lines		
Sf9 Insect cells	Thermo Fisher	Cat# 11496015
High Five Insect cells	Thermo Fisher	Cat# B85502
K562 human cells	ATCC	ATCC#CCL-243; RRID: CVCL_00004
Experimental models: Organisms/strains		
<i>Saccharomyces cerevisiae</i> : Strain S288C: BY4741; MATa his3Δ1leu2Δ0 met15Δ0 ura3Δ0	Euroscarf	Cat# Y00000
CRLY12; BY4741, Gid4::KANMX	This study	N/A
CRLY14; BY4741, Gid7::KANMX	This study	N/A
CRLY45; BY4741, Gid8::Gid8-3xFLAG-KANMX	Qiao et al., 2020	N/A
CRLY131; BY4741, Gid2::3xFLAG-Gid2 (K365A)	Qiao et al., 2020	N/A
CRLY241; BY4741, Gid7::KANMX, Gid8::Gid8-3xFLAG-HPHNT1	This study	N/A
CRLY267; BY4741, Gid7::Gid7-3xHA-HPHNT1, Gid5::Gid5-3xFLAG-KANMX	This study	N/A
CRLY498; BY4741, Fbp1::Fbp1-3xFLAG-HPHNT1, Pdr5::NATNT2	This study	N/A
CRLY504; BY4741, Fbp1::Fbp1-3xFLAG-HPHNT1, Pdr5::NATNT2, Gid7::KANMX	This study	N/A
Recombinant DNA		
pCSJ95	Chen et al., 2017	N/A
pCSJ125	Chen et al., 2017	N/A
VBP6; pRS313-pGPD-Pck1-3xFLAG-CYC-pGPD-DHFR-HA-CYC	This study	N/A
DSJC1; pRS313-pGPD-Fbp1-K32R/K35R-3xFLAG-CYC-pGPD-DHFR-HA-CYC	This study	N/A
DSJC2; pRS313-pGPD-Fbp1-K280R/K281R-3xFLAG-CYC-pGPD-DHFR-HA-CYC	This study	N/A

(Continued on next page)

Continued

REAGENT or RESOURCE	SOURCE	IDENTIFIER
DSJC3; pRS313-pGPD-Fbp1-K32R/K35R/K280R/K281R-3xFLAG-CYC-pGPD-DHFR-HA-CYC	This study	N/A
pRS415-pTEF-CYC	This study	N/A
pRS415-pTEF-GFP-ScGid4-CYC	This study	N/A
pLIB Gid1	This study	N/A
pLIB Gid2	This study	N/A
pLIB Gid4	This study	N/A
pLIB Gid5	This study	N/A
pLIB Gid7	This study	N/A
pLIB Gid8-TEV-2xStrep	This study	N/A
pLIB Gid8	This study	N/A
pLIB Gid9	This study	N/A
pLIB RANBP9	This study	N/A
pLIB RMND5A	This study	N/A
pLIB hGid4	This study	N/A
pLIB ARMC8	This study	N/A
pLIB 2xStrep-3C-ARMC8	This study	N/A
pLIB MAEA	This study	N/A
pLIB WDR26	This study	N/A
pLIB GST-TEV-WDR26	This study	N/A
pLIB MKLN1	This study	N/A
pLIB YPEL5	This study	N/A
pLIB MAEA Y394A	This study	N/A
pLIB RMND5A R340A	This study	N/A
pLIB RMND5A I338A/L339A	This study	N/A
pLIB GST-TEV-Uba1	This study	N/A
pBIG2 Gid1:Gid8-TEV-2xS:Gid5:Gid4:Gid2:Gid9	This study	N/A
pBIG2 Gid1:Gid8-TEV-2xS:Gid5:Gid2:Gid9	This study	N/A
pBIG2 Gid1:Gid8-TEV-2xS:Gid5:Gid2:Gid9:Gid7	This study	N/A
pBIG2 Gid1:Gid8-TEV-2xS:Gid5:Gid4:Gid2:Gid9:Gid7	This study	N/A
pBIG1 RANBP9:TWA1-TEV-2xS:ARMC8	This study	N/A
pBIG1 RANBP9:TWA1:2xS-3C-ARMC8	This study	N/A
pBIG2 RANBP9:TWA1-TEV-2xS:ARMC8:RMND5A:MAEA	This study	N/A
pBIG2 RANBP9:TWA1-TEV-2xS:ARMC8:RMND5A	This study	N/A
pBIG2 RANBP9:TWA1-TEV-2xS:ARMC8:MAEA	This study	N/A
pGEX GST-TEV-Gid4 (Δ 1-116)	This study	N/A
pGEX GST-TEV-Gid7	This study	N/A
pGEX GST-TEV-Gid7 (Δ 1-285)	This study	N/A
pGEX GST-TEV-hGid4 (Δ 1-99)	This study	N/A
pGEX GST-TEV-hGid4 (R189A)	This study	N/A
pGEX GST-TEV-hGid4 (Y154A)	This study	N/A
pGEX GST-TEV-hGid4 (F174A)	This study	N/A
pGEX GST-TEV-hGid4 (F239A)	This study	N/A
pGEX GST-TEV-hGid4 (C156D)	This study	N/A

(Continued on next page)

Continued

REAGENT or RESOURCE	SOURCE	IDENTIFIER
pGEX GST-TEV-hGid4 (E298A)	This study	N/A
pGEX GST-TEV-hGid4 (H147D)	This study	N/A
pGEX GST-TEV-hGid4 (Y158A/F174A)	This study	N/A
pGEX GST-TEV-hGid4 (Y158A/F239A)	This study	N/A
pGEX GST-TEV-hGid4 (F174A/F239A)	This study	N/A
pGEX GST-TEV-hGid4 (Y297A/F229A)	This study	N/A
pGEX GST-TEV-hGid4 (Δ 297-300)	This study	N/A
pRSF Ubc8-6xHis	This study	N/A
pRSF Fbp1-6xHis	This study	N/A
pRSF Fbp1 (K32R/K35R)-6xHis	This study	N/A
pRSF Fbp1 (K280R/K281R)-6xHis	This study	N/A
pRSF Fbp1 (K32R/K35R/K280R/ K281R)-6xHis	This study	N/A
pRSF Fbp1-GGGGS-sortag-6xHis	This study	N/A
pRSF Mdh2-GGGGS-sortag-6xHis	This study	N/A
pRSF Pck1-GGGGS-sortag-6xHis	This study	N/A
pQlink Fbp1-TEV-V5-2xS	This study	N/A
pRSF Ube2H-6xHis	This study	N/A
pGEX GST-3C-Ub	This study	N/A
pGEX GST-3C-Ub K0 (all K > R)	This study	N/A
pGEX GST-3C-Ub K6 (all K > R; R6K)	This study	N/A
pGEX GST-3C-Ub K11 (all K > R; R11K)	This study	N/A
pGEX GST-3C-Ub K27 (all K > R; R27K)	This study	N/A
pGEX GST-3C-Ub K29 (all K > R; R29K)	This study	N/A
pGEX GST-3C-Ub K33 (all K > R; R33K)	This study	N/A
pGEX GST-3C-Ub K48 (all K > R; R48K)	This study	N/A
pGEX GST-3C-Ub K63 (all K > R; R63K)	This study	N/A
pET3b Ub	This study	N/A
pET29 sortase A	Chen et al., 2011b	N/A

Software and algorithms

FOCUS	Biyani et al., 2017	https://focus.c-cina.unibas.ch/documentation.php
SerialEM	Mastronarde, 2003	https://bio3d.colorado.edu/SerialEM/
MOTIONCOR2	Zheng et al., 2017	https://emcore.ucsf.edu/ucsf-software
Gctf	Zhang, 2016	https://www2.mrc-lmb.cam.ac.uk/download/gctf/
Gautomatch	Kai Zhang	https://www2.mrc-lmb.cam.ac.uk/download/gautomatch-053/
Relion3.0/3.1	Fernandez-Leiro and Scheres, 2017 ; Scheres, 2012 ; Zivanov et al., 2018	https://www3.mrc-lmb.cam.ac.uk/relion/index.php/Main_Page
Phyre ²	Kelley et al., 2015	http://www.sbg.bio.ic.ac.uk/~phyre2/html/page.cgi?id=index
SWISS-MODEL	Waterhouse et al., 2018	https://swissmodel.expasy.org
UCSF Chimera	Pettersen et al., 2004	https://www.cgl.ucsf.edu/chimera/
UCSF ChimeraX	Goddard et al., 2018	https://www.rbvi.ucsf.edu/chimerax/
PyMOL v2.1	Schrödinger	https://pymol.org/2/
CCP-EM	Burnley et al., 2017	https://www.ccpem.ac.uk/download.php
Buccaneer	Cowtan, 2006	http://www.yesbl.york.ac.uk/~cowtan/buccaneer/buccaneer.html

(Continued on next page)

Continued

REAGENT or RESOURCE	SOURCE	IDENTIFIER
Coot	Emsley and Cowtan, 2004; Emsley et al., 2010	https://www2.mrc-lmb.cam.ac.uk/personal/pemsley/coot/
Phenix	Adams et al., 2010; Afonine et al., 2018; DiMaio et al., 2013	https://www.phenix-online.org/
Molprobrity	Chen et al., 2010	http://molprobrity.biochem.duke.edu/
Image Studio	LI-COR Biosciences	https://www.licor.com/bio/image-studio/
Fiji/ImageJ	Schindelin et al., 2012	https://imagej.net/Welcome
GraphPad Prism version 8.0	GraphPad Software	http://www.graphpad.com:443/
ImageQuant TL Toolbox version 8.2	Cytiva (formerly GE Healthcare)	https://www.cytivalifesciences.com
DeepEMhancer	Sanchez-Garcia et al., 2020	http://www.biorxiv.org
Other		
QUANTIFOIL® R1.2/1.3, 100 Holey Carbon Films, Grids: Cu 200 mesh	Quantifoil Micro Tools GmbH	https://www.quantifoil.com
IMEM	Thermo Fisher	Cat# 12440-053

RESOURCE AVAILABILITY

Lead contact

Information and requests for resources and reagents should be directed to the Lead Contact, Prof. Dr. Brenda Schulman (schulman@biochem.mpg.de).

Materials availability

All unique/stable reagents generated in this study are available from the lead contact with a completed Materials Transfer Agreement.

Data and code availability

The accession codes for the PDB models and EM maps are available in RCSB and EMDB, respectively, as follows: Apo Chelator-GID^{SR4}, EMDB: EMD-12541; Chelator-GID^{SR4} + Fbp1, EMDB: EMD-12557; GID^{SR4}, EMDB: EMD-12548; SRS module, EMDB: EMD-12559, PDB: 7NS3; Cat module, EMDB: EMD-12560; PDB: 7NS4; SA module, EMDB: EMD-12563; PDB: 7NSB; Endogenous GID^{Ant}, EMDB: EMD-12538; Endogenous Chelator-GID^{Ant}, EMDB: EMD-12540; CTLH^{SR4}, EMDB: EMD-12537; CTLH^{SR4} SRS module, EMDB: EMD-12564; PDB: 7NSC; CTLH-WDR26 supramolecular assembly, EMDB: EMD-12542; CTLH-WDR26 SA and SRS modules, EMDB: EMD-12545; CTLH-MKLN1 SA and SRS modules, EMDB: EMD-12547; Fbp1 crystal structure, PDB: 7NS5.

All proteomics data have been deposited on ProteomeXchange with the dataset identifier PRIDE: PXD024462.

All the unprocessed image data have been deposited to Mendeley Data : <http://dx.doi.org/10.17632/rfpg6939c.1>

METHOD DETAILS

Yeast strain construction and growth conditions

The yeast strains used in this study are specified in the Key Resources Table. They were constructed as derivatives of BY4741 using standard genetic techniques (Janke et al., 2004; Knop et al., 1999; Storici and Resnick, 2006) and were verified using PCR, DNA sequencing and immunoblotting (to confirm protein expression). Unless stated otherwise, yeast strains were grown to OD₆₀₀ of 1.0 in synthetic dropout (SD-glucose; 0.17% yeast nitrogen base, 0.5% ammonium sulfate, 2% glucose, amino acid mix) or yeast peptone-based medium (YPD; 1% yeast extract, 2% peptone, 2% glucose) as indicated in the respective assays.

In vivo yeast substrate degradation assays

Degradation assays were performed to test the dependency of Fbp1, Mdh2, and Pck1 degradation on Gid4 and Gid7 (Figure 1F) using the promoter reference technique adapted from Oh et al. (2017). The respective strains were transformed with a plasmid harboring the open reading frame of either Fbp1-3xFLAG, Mdh2-3xFLAG or Pck1-3xFLAG and the control protein DHFR-HA, both expressed from identical promoters. Cells were grown in SD-glucose medium to OD₆₀₀ of 1.0 before being starved in SE medium (0.17% yeast nitrogen base, 0.5% ammonium sulfate, 2% ethanol, amino acid mix) for 19 hours. Subsequently, an equivalent of 1 OD₆₀₀ was transferred to SD-glucose medium containing 0.5 mM tetracycline that inhibits translation of the respective substrate and DHFR by binding to specific RNA-regions within their ORFs. At the indicated time points, 1 mL or 1 OD₆₀₀ of cells was harvested. Cell lysis was performed by resuspending the pellets in 800 μ L 0.2 M NaOH and incubating them on ice for 20 minutes with subsequent centrifugation at 11,200xg for 1 minute at 4°C. The pellets were aspirated and resuspended in 50 μ L HU buffer (8 M Urea, 5%

SDS, 1 mM EDTA, 100 mM DTT, 200 mM Tris-HCl, pH 6.8, protease inhibitor, bromphenol blue), heated at 70°C for 10 minutes and then centrifuged again for 5 minutes at 11,200xg at 4°C. Protein levels of the substrates and a control protein DHFR were visualized by immunoblotting with anti-FLAG and anti-HA antibodies, respectively, and imaged using a Typhoon scanner (GE Healthcare). The bands were quantified using the ImageStudioLite software (LI-COR) and the substrate signal was normalized relative to the DHFR signal for every sample. At least three biological replicates were considered for all *in vivo* assays and the standard deviation was presented using error bars.

To validate the major ubiquitylation sites in Fbp1 *in vivo* (Figure 5B), the above-described PRT degradation assays were carried out in a similar manner with Fbp1-3xFLAG mutants, in which the lysines targeted by Chelator-GID^{SR4} (K32, K35, K280 and K281) were mutated to arginine.

To test if overexpression of Gid4 affects degradation of Fbp1 in Δ Gid7 yeast (Figure S1E), the GFP-Gid4 overexpression plasmid was transformed together with the Fbp1-3xFLAG PRT plasmid into different yeast strains (WT, Δ Gid7 and a Gid2^{K365A} catalytically inactive mutant). The cells were grown in SD medium lacking histidine and leucine, which served as selection markers for the Gid4 overexpression plasmid. After 8 h growth in SD-glucose media, samples of 1 OD₆₀₀ were harvested and analyzed as described above.

Purification of endogenous yeast GID for cryo EM

To purify endogenous GID complex, 3 l of a yeast strain with Gid7 and Gid5 C-terminally tagged at their endogenous loci with an HA and 3xFLAG tag, respectively, were grown in YPD medium for 8 hours. Subsequently, the cells were washed and resuspended to OD₆₀₀ of 1.0 in YPE medium (1% yeast extract, 2% peptone, 2% ethanol). Cells were harvested at OD₆₀₀ of 18.0. The pellet was resuspended in the lysis buffer (50 mM HEPES pH 7.5, 150 mM NaCl, 1 mM CaCl₂, 0.2 M sorbitol, complete protease inhibitor tablets) and frozen in liquid nitrogen in the form of small beads. For lysis, the frozen yeast pellets were subjected to cryogenic grinding using a cryo-mill (SPEX Sample Prep-6875 Freezer/Mill). The obtained yeast powder was thawed and centrifuged at 35,000 rpm for 10 minutes, and the resultant supernatant was incubated with ANTI-FLAG M2 affinity resin for an hour. After thorough washing, the protein was eluted using 3xFLAG peptide and visualized by Coomassie-stained SDS-PAGE. The eluted complex was concentrated to 1 mg/ml and analyzed by cryo EM.

Sucrose gradient fractionation of yeast lysates (Figure S2C)

Yeast strains with Gid8 C-terminally tagged at its endogenous locus with a 3xFLAG tag, with or without Gid7 deleted were grown in YPD media for 8 hours. Subsequently, they were switched to YPE medium and grown for 19 to 24 hours. One part of both cultures was harvested, while the other was switched to YPD medium for glucose recovery and harvested after 2 hours. The pellets were resuspended and lysed using a cryo-mill (as described above). To perform sucrose gradient fractionation of yeast lysates, roughly 300–500 mg of yeast powder was resuspended in the lysis buffer (50 mM HEPES, pH 7.5, 150 mM NaCl, 1 mM CaCl₂, 0.2 M sorbitol, complete protease inhibitor tablets). To aid in resolubilization, lysates were incubated for 15 minutes at 4°C with gentle agitation, and then pre-cleared by centrifugation at 17,000xg for 10 minutes. Protein concentration was normalized by Bradford assay, lysates were loaded onto a 5%–40% sucrose gradient, and centrifuged at 34,300 rpm for 16 hours at 4°C. Gradients were then fractionated into fourteen equal fractions and loaded onto a 12% SDS-PAGE gel. Proteins were visualized by immunoblotting and imaged with Amersham Typhoon imager (GE Healthcare).

In vivo Fbp1 ubiquitylation assay (Figure 1E)

Yeast strains with Fbp1 tagged at its endogenous locus with 3xFLAG were grown to OD₆₀₀ of 1.0–1.5 in YPD, pelleted by centrifugation at 3,000 rpm for 3 min, washed with pre-warmed YPE, resuspended to an OD₆₀₀ = 1 in fresh, pre-warmed YPE, and grown at 30°C for 18 hours. Cultures for the ethanol condition were then diluted to an OD = 1 in fresh, pre-warmed YPE containing 1% DMSO. For the recovery condition, cells were pelleted by centrifugation at 3,000 rpm for 3 minutes, and resuspended in fresh pre-warmed YPD containing 1% DMSO. After two hours of growth at 30°C, 50 ODs of cells were pelleted by centrifugation at 3,000 rpm for 3 minutes, and flash frozen in liquid nitrogen.

Samples were resuspended in 1 mL lysis buffer (50 mM Tris-HCl, pH7.5, 150 mM NaCl, 2 mM EDTA, 50 mM NaF, 0.1% SDS, 1% NP-40, 0.5% Na-deoxycholate, 1% glycerol, 20 mM NEM, and complete protease inhibitor tablets), and lysed by 3 rounds of 20 s in a FastPrep-24 instrument, resting 5 minutes on ice between each round. Lysates were then pre-cleared by centrifugation at 4,000xg for 10 minutes, and the supernatant was added to pre-equilibrated His-Halo-UBA^{UBQLN1}-conjugated agarose beads, and incubated for 2 hours at 4°C with gentle rotation. Beads were separated by centrifugation at 800xg for 1 minute, washed once with lysis buffer and four times with wash buffer (50 mM Tris-HCl, pH7.5, 150 mM NaCl, 2 mM EDTA, 50 mM NaF, 0.1% SDS, 1% NP-40, 0.5% Na-deoxycholate, 1% glycerol). Proteins were eluted by addition of sample buffer, and heating at 95°C for 5 minutes. Samples were then loaded on a 12% SDS-PAGE gel and visualized by immunoblotting.

Plasmid preparation and Mutagenesis

All the genes encoding yeast GID subunits and the substrates Fbp1, Mdh2 and Pck1 were originally amplified from *S. cerevisiae* BY4741 genomic DNA. The genes coding for subunits of human CTLH were obtained from human cDNA library (Max Planck Institute of Biochemistry), except for hGid4, which was codon-optimized for bacterial expression system and synthesized by GeneArt gene

synthesis service (Thermo Fisher Scientific). The sequences of all the CTLH genes correspond to the canonical UniProt sequences, besides ARMC8, for which isoform 2 (missing the residues 2-15 of the canonical sequence) was used based on the prior literature (Kobayashi et al., 2007).

The constructs for recombinant protein expression were generated by Gibson assembly method (Gibson et al., 2009), whereas the mutant versions of the genes were prepared by the QuickChange protocol (Stratagene). All the coding sequences used for protein expression were verified by DNA sequencing. To express GID/CTLH subunits from a single baculoviral expression vector, the genes were combined by the biGBac method (Weissmann et al., 2016). All the plasmids used in this study are listed in the [Key resources table](#).

Insect cell expression and purification of GID/CTLH complexes

Both yeast GID and human CTLH complexes used for the biochemical assays and cryo EM were expressed in insect cells. For protein expression, Hi5 insect cells were transfected with recombinant baculovirus variants carrying the respective protein-coding sequences and grown for 60 to 72 hours in EX-CELL 420 Serum-Free Medium at 27°C. After harvesting, insect cell pellets were resuspended in a lysis buffer containing 50 mM HEPES pH 7.5, 200 mM NaCl, 5 mM DTT, 10 μg/ml leupeptin, 20 μg/ml aprotinin, 2 mM benzamide, EDTA-free Complete protease inhibitor tablet (Roche, 1 tablet per 50 mL of buffer) and 1 mM PMSF.

All recombinant yeast GID complexes were purified from insect cell lysates by StrepTactin affinity chromatography by pulling on a twin-Strep tag fused at the Gid8 C terminus. Further purification was performed by anion exchange chromatography and size exclusion chromatography (SEC) in the final buffer containing 25 mM HEPES pH 7.5, 200 mM NaCl and 5 mM (Buffer A) or 1 mM DTT (Buffer B) for cryo EM and biochemical assays, respectively. To ensure a stoichiometric level of the substrate receptor Gid4 in all cryo EM samples, all GID complexes were expressed without Gid4, and a bacterially-expressed truncated version of Gid4 (Δ1-116) was added at a 2-fold molar excess to Gid^{Ant} (Gid1-Gid8-Gid2-Gid9-Gid5) before final SEC. To assemble Chelator-GID^{SR4}, both Gid4 (Δ1-116) and Gid7 were added to Gid^{Ant} at a 2-fold molar excess before final SEC. For the sample of Chelator-GID^{SR4} with Fbp1 bound, 2-fold molar excess of the substrate was added to a purified and concentrated complex just before cryo EM grids preparation. A list of yeast GID complexes analyzed by cryo EM along with strategies for their expression and purification is shown below:

1. Chelator-GID^{SR4}: Gid1, Gid2, Gid5, Gid8-2xS, Gid9 coexpressed in Hi5 insect cells; bacterially expressed Gid4 (Δ1-116) and Gid7 added before final SEC; purified by StrepTactin affinity, IEX and SEC
2. Fbp1-bound Chelator-GID^{SR4}: Gid1, Gid2, Gid5, Gid8-2xS, Gid9 coexpressed in Hi5 insect cells; bacterially expressed Gid4 (Δ1-116) and Gid7 added before final SEC; purified by StrepTactin affinity, IEX and SEC; Fbp1-6xHis added directly before cryo EM grids preparation
3. GID^{SR4}: Gid1, Gid2, Gid5, Gid8-2xS, Gid9 coexpressed in Hi5 insect cells; bacterially expressed Gid4 (Δ1-116) added before final SEC; purified by StrepTactin affinity, IEX and SEC

CTLH^{SR4} and CTLH-MKLN1 subcomplex comprising SA and SRS modules were purified from insect cell lysates by StrepTactin affinity chromatography by pulling on a twin-Strep tag fused at the TWA1 C terminus, whereas the CTLH-WDR26 subcomplex comprising SA and SRS modules was pulled on a twin-Strep tag at the ARMC8 N terminus. Further purification was performed by anion exchange chromatography and size exclusion chromatography in Buffer A or Buffer B. As for yeast GID, the CTLH subcomplexes used for cryo EM were saturated with hGid4 by mixing them with the bacterially-expressed truncated version of hGid4 (Δ1-99) and running SEC. CTLH-WDR26 supramolecular assembly was purified from lysates by a tandem affinity chromatography, by first pulling on TWA1-2xS and then GST-WDR26. The pull-down fractions were run on SEC in Buffer A. A list of human CTLH complexes analyzed by cryo EM along with strategies for their expression and purification is shown below:

1. CTLH-WDR26 supramolecular assembly: RANBP9, TWA1-2xS, ARMC8, RMND5A, MAEA, GST-WDR26 coexpressed in Hi5 insect cells; purified by tandem StrepTactin and GST affinity and SEC
2. CTLH-WDR26 SA and SRS modules: RANBP9, TWA1, 2xS-ARMC8, WDR26, YPEL5 coexpressed in Hi5 insect cells; bacterially expressed hGid4 (Δ1-99) added before final SEC; purified by StrepTactin affinity, IEX and SEC
3. CTLH-MKLN1 SA and SRS modules: RANBP9, TWA1-2xS, ARMC8, MKLN1 coexpressed in Hi5 insect cells; bacterially expressed hGid4 (Δ1-99) added before final SEC; purified by StrepTactin affinity, IEX and SEC
4. CTLH^{SR4}: RANBP9, TWA1-2xS, ARMC8, RMND5A, MAEA coexpressed in Hi5 insect cells; bacterially expressed hGid4 (Δ1-99) added before final SEC; purified by StrepTactin affinity, IEX and SEC

Bacterial expression and purification

All bacterial expressions were performed in *E. coli* BL21 (DE3) RIL cells in a Terrific Broth (TB) medium overnight at 18°C.

All the mutant and WT versions of Gid4 (both yeast and human ortholog) and Gid7 were expressed as GST-TEV fusions. After harvesting, cell pellets were resuspended in the lysis buffer containing 50 mM HEPES pH 7.5, 200 mM NaCl, 5 mM DTT and 1 mM PMSF and purified from bacterial lysates by glutathione affinity chromatography, followed by overnight digestion at 4°C with tobacco etch virus (TEV) protease to liberate the GST tag. Further purification was carried out with size exclusion chromatography in Buffer B. Additionally, a pass-back over glutathione affinity resin was performed to get rid of the remaining uncleaved GST-fusion protein and free

GST, Ubc8, Ube2H, Ub (for generating ubiquitylated Fbp1), Fbp1 (WT and mutants), Mdh2 and Pck1 were expressed as their C-terminally 6xHis-tagged versions. After harvesting, cell pellets were resuspended in the lysis buffer containing 50 mM HEPES pH 7.5, 200 mM NaCl, 5 mM β -mercaptoethanol, 10 mM imidazole and 1 mM PMSF, and purified from bacterial lysates by nickel affinity chromatography, followed by anion exchange and size exclusion chromatography in Buffer A or Buffer B (for structural studies and activity assays, respectively). Fbp1-V5-2xS (for Fbpase activity assays) was purified by StrepTactin affinity chromatography and SEC in Buffer B.

Untagged WT ubiquitin used for *in vitro* assays was purified via glacial acetic acid method (Kaiser et al., 2011), followed by gravity S column ion exchange chromatography and size exclusion chromatography in Buffer B. Different Ub variants as well as WT Ub used for the ubiquitin chain type determination assay were expressed as GST-3C fusions and purified by glutathione affinity chromatography, followed by incubation with HRV-3C protease for 3 hours at room temperature. Further purification was done with size exclusion chromatography in Buffer B.

Fluorescent tagging of the GID substrates Fbp1, Mdh2 and Pck1 used for all the biochemical assays was performed with a sortase A-mediated reaction, which catalyzed fusion of fluorescein to the C terminus of the substrate. The reaction mix contained 50 μ M of the substrate, which was C-terminally tagged with a sortag (LPETGG) and a 6xHis tag, 250 μ M of a fluorescent peptide (GGGGGFYVK-FAM) and 50 μ M of sortase A (Chen et al., 2011b). The labeling reaction was carried out for 30 minutes at room temperature in a buffer comprising 50 mM Tris-HCl pH 8, 150 mM NaCl and 10 mM CaCl_2 . The reaction mixture was consecutively passed-back through the Ni-NTA Sepharose resin to get rid of unreacted Fbp1. Further purification was done with size exclusion chromatography in Buffer B.

All the labeled and unlabeled peptides used in the biochemical assays were synthesized in the MPIB Biochemistry Core Facility.

In vitro biochemical assays

All *in vitro* activity assays were performed at room temperature in a buffer containing 25 mM HEPES pH 7.5, 150 mM NaCl, 5 mM ATP and 10 mM MgCl_2 . To ensure that all the reaction mixtures contained equal concentrations of WT and mutant versions of Gid4 and Gid7, these proteins were added exogenously for all assays besides kinetics. To analyze kinetics of Fbp1 ubiquitylation, the assays were performed with purified GID^{SR4} and Chelator-GID^{SR4} obtained by co-expressing all of their subunits, as well as GID^{SR4} mixed with Gid7 before starting the reaction. All the reactions were quenched at indicated time points by mixing an aliquot of the total reaction mix with SDS-PAGE loading buffer. Ubiquitylation of fluorescent substrates was visualized by a fluorescent scan of SDS-PAGE gel using the Amersham Typhoon imager (GE Healthcare).

Biochemical assays with yeast GID

The influence of Gid7 and Gid4 on ubiquitylation of the full-length (Figures 1A and 1B) and peptide versions (Figure S1B) of Fbp1 was tested in a multiturnover assay format using 0.2 μ M Uba1, 1 μ M Ubc8-6xHis, 0.5 μ M GID^{Ant}, 0 or 1 μ M Gid4, 0 or 2 μ M Gid7, 1 μ M full-length Fbp1-FAM or a fluorescently labeled model peptide substrate and 20 μ M Ub (WT or all K > R (K0) version). The model peptide substrate was designed with the N-terminal Fbp1 sequence (aa 2-16) and a single lysine placed at position 27 (to span the distance between the substrate receptor Gid4 and the catalytic center measured in the structure of Chelator-GID^{SR4}). Similarly, the influence of Gid7 and Gid4 on ubiquitylation of other gluconeogenic substrates, Mdh2 and Pck1, was tested in a multiturnover assay using their fluorescently labeled versions and carried out under identical conditions (Figure 1A). The same assay format and conditions were employed to qualitatively compare Fbp1 ubiquitylation activity of GID^{SR4} exogenously mixed with Gid7 to that of the SEC-purified Chelator-GID^{SR4} (containing co-expressed Gid7) (Figure S1C). All the assays were performed in at least duplicates and some of them were quantified using image analysis software ImageQuant (GE healthcare; version 8.2).

To test the influence of Gid7 on intrinsic activity of GID E3, a substrate-independent pulse-chase assay monitoring discharge of Ubc8~Ub to free lysine in solution was employed (Figure S1A). In the pulse reaction, loading of Ubc8 was performed by mixing 0.5 μ M Uba1, 10 μ M Ubc8-6xHis, 30 μ M Ub, 2.5 mM MgCl_2 and 1 mM ATP. After 15 minutes at room temperature, Ubc8 loading was stopped by incubation of the pulse mixture with 50 mM EDTA on ice for 5 minutes. For the chase reaction, the quenched pulse mixture was mixed with an equal volume of the chase-initiating mixture containing 1 μ M GID^{SR4} complex, 0 or 2 μ M Gid7 (WT or Δ 1-285 mutant) and 25 mM lysine pH 8.0. The discharge was carried out at room temperature, quenched at different time points and visualized by non-reducing SDS-PAGE stained with Coomassie.

Avid binding of Fbp1 to Chelator-GID^{SR4} was verified by performing a competition ubiquitylation assay in a multiturnover format (Figure 4D). The reactions were initiated by mixing 0.2 μ M Uba1, 1 μ M Ubc8-6xHis, 0.5 μ M E3 GID^{SR4}, 0 or 2 μ M Gid7 (WT or its Δ 1-284 mutant), 0.5 μ M of fluorescently labeled tetrameric Fbp1 or a monomeric model peptide substrate containing Fbp1 degron (as described above), 20 μ M of an unlabeled competitor (full-length Fbp1-6xHis with major target lysines K32, K35, K280, K281 mutated to R or a lysine-less 9-residue peptide containing Fbp1 N-terminal sequence) and 20 μ M Ub. Before starting the reaction, GID^{SR4} was incubated with Gid7 for 3 minutes.

To validate the preferred ubiquitylation sites in Fbp1 determined by proteomics, multi-turnover ubiquitylation assays were performed using mutants of Fbp1, in which the pairs of major target lysines were mutated to arginine separately or together (Figure 5A). The reaction mixtures contained 0.2 μ M Uba1, 1 μ M Ubc8-6xHis, 0.5 μ M GID^{Ant}, 1 μ M Gid4, 2 μ M Gid7, 1 μ M Fbp1-6xHis (WT or target K > R mutants) and 20 μ M Ub (WT or its all K > R (K0) version). Ubiquitylation of the substrates was visualized by immunoblotting with anti-His antibody.

Determination of kinetic parameters of Fbp1 ubiquitylation by GID E3

To examine the effect of Gid7 on the Michaelis-Menten constant K_m for Fbp1 ubiquitylation by GID E3 (Figure 1C), multiturnover assays were performed by titrating the E3 concentration and with substrate levels that were below K_m . Assays were performed with GID^{SR4}, GID^{SR4} mixed with Gid7 as well as a purified Chelator-GID^{SR4} (GID^{SR4} coexpressed with Gid7). Reactions were quenched at time points such that the initial velocities of all reactions were well within the linear range (determined by running time courses for reactions that contained the highest E3 concentration from the titrations). Reactions with GID^{SR4} comprised 0.2 μ M Uba1, 1 μ M Ubc8, 0.25–8 μ M GID^{SR4}, 0.5 μ M Fbp1-FAM and 20 μ M Ub, and were quenched after 8 minutes. For GID^{SR4} exogenously mixed with Gid7, reactions comprised 0.2 μ M Uba1, 1 μ M Ubc8, 0.025–0.8 μ M GID^{SR4} mixed with a 2-fold excess of Gid7, 0.1 μ M Fbp1-FAM and 20 μ M Ub, and were quenched after 3 minutes. In the case of Chelator-GID^{SR4}, the reaction mixes contained 0.2 μ M Uba1, 1 μ M Ubc8, 0.03–1 μ M Chelator-GID^{SR4}, 0.1 μ M Fbp1-FAM and 20 μ M Ub, and the reactions were quenched after 2 minutes. Reaction substrate and products were resolved by SDS-PAGE and quantified using ImageQuant (GE healthcare; version 8.2). Fraction of Fbp1 that had been modified by one or more ubiquitins was then plotted as a function of E3 concentration in GraphPad Prism and fit to the Michaelis-Menten equation using non-linear curve fitting. All reactions were performed in duplicate.

Since the method described in the previous paragraph involved titration of E3 levels rather than that of the substrate, k_{cat} was estimated using the following protocol. Initial velocities were measured for both GID^{SR4} and Chelator-GID^{SR4} by performing a time course where the ratios of both E3 to K_m and substrate to K_m were the same for each E3 complex (2.7 and 0.4, respectively). The fraction of ubiquitylated Fbp1 was plotted in GraphPad Prism as a function of time (Figure S1D) and the rate of the reaction was estimated by linear regression. Having calculated the rate, initial velocities V_0 were calculated using the following equation: $V_0 = rate \cdot [S]$. V_{max} was then estimated using a modified form of the Michaelis-Menten equation: $V_{max} = \frac{V_0 \cdot (K_m + [S])}{[S]}$, where $[S] = \frac{K_m}{2.5}$ because the substrate concentration was 2.5 times lower than K_m . To obtain k_{cat} values, V_{max} was divided by the E3 concentration: $k_{cat} = \frac{V_{max}}{[E3]}$.

Biochemical assays with human CTLH^{SR4}

All *in vitro* ubiquitylation assays with CTLH^{SR4} were performed using a 30-residue fluorescent model peptide substrate harboring an N-terminal hGid4-interacting sequence PGLW and a single lysine placed at position 27, which is an optimal distance between the catalytic module and hGid4 based on the cryo EM structure.

To probe the residues of hGid4 that mediate its incorporation into CTLH^{SR4}, structure-based hGid4 mutants (corresponding to homologous mutations in yeast Gid4 (Qiao et al., 2020)) were tested in a binding test (Figure S6D) and ubiquitylation assays (Figure S6E). For the binding test, 10-fold molar excess of the purified WT and mutant hGid4 (Δ 1–99) was mixed with 20 μ g of RANBP9-TWA1-ARMC8-RMND5A-MAEA complex (tagged with a twin-Strep tag at TWA1 C terminus) in a buffer containing 25 mM HEPES pH 7.5, 150 mM NaCl and 1 mM DTT. After incubating the proteins for 30 minutes on ice, 40 μ L of the StrepTactin resin was added to the mixture and further incubated for 1 hour. As a control, RANBP9-TWA1-ARMC8-RMND5A-MAEA complex and hGid4 were mixed with StrepTactin alone. After throughout wash of the resin, elution fractions were collected and analyzed with SDS-PAGE stained with Coomassie. Ubiquitylation reactions were performed in a multiturnover format by mixing 0.2 μ M Uba1, 2 μ M Ube2H-6xHis, 1 μ M RANBP9-TWA1-ARMC8-RMND5A-MAEA complex, 1 μ M hGid4 (Δ 1–99, WT or an indicated mutant), 0.5 μ M fluorescent model peptide substrate and 20 μ M Ub.

The catalytic mechanism of CTLH was examined by testing mutants of RMND5A and MAEA in substrate-independent discharge reactions (Figure S6G) and ubiquitylation assays (Figure S6H). The substrate-independent reactions monitored the discharge of Ube2H~Ub to free lysine in solution in a pulse-chase format, applying the conditions as described for the assay with yeast GID. For the ubiquitylation multiturnover assays, the reactions contained 0.2 μ M Uba1, 2 μ M Ube2H-6xHis, 1 μ M RANBP9-TWA1-ARMC8-RMND5A-MAEA complex (containing either WT or indicated mutants of RMND5A or MAEA), 1 μ M hGid4 (Δ 1–99), 0.5 μ M fluorescent model peptide substrate and 20 μ M Ub.

For characterizing the ubiquitin chain type formed by CTLH^{SR4} in conjunction with Ube2H, a multiturnover assay was performed (Figure S6I). The reaction mix contained 0.2 μ M Uba1, 2 μ M Ube2H-6xHis, 1 μ M RANBP9-TWA1-ARMC8-RMND5A-MAEA complex, 1 μ M hGid4 (Δ 1–99), 0.5 μ M fluorescent model peptide substrate and 20 μ M Ub (WT, lysine-less (all K > R) or one of its single-lysine variants (with all but one lysine mutated to arginine)).

SEC for initial characterization of GID supramolecular assembly

For initial test of how Gid7 affects GID complex assembly (Figure S2A), 200 μ L of 10 μ M Gid7 and GID^{SR4} alone or together (mixed in 1:1 ratio) were loaded onto a Superose 6 column (GE Healthcare) equilibrated with 25 mM HEPES 7.5, 150 mM NaCl and 5 mM DTT. SEC fractions were analyzed with Coomassie-stained SDS-PAGE.

SEC-MALS

To determine the oligomeric state of Fbp1 and Gid7 (Figure S2B), the proteins were subjected to SEC-MALS analysis. For each run, 100 μ L of samples at 1 mg/mL were loaded onto Superdex 200 column equilibrated with a buffer containing 25 mM HEPES pH 7.5, 150 mM NaCl and 5 mM DTT. SEC-MALS was conducted in the MPIB Biochemistry Core Facility.

Fbp1 enzyme activity assay

To test the effect of Fbp1 ubiquitylation on its activity (Figure 5E) and sensitivity to allosteric regulation by AMP (Figure 5F), EnzChek Phosphate Assay Kit (ThermoFisher Scientific) was employed. This assay quantifies inorganic phosphate (P_i) released from fructose-1,6-bisphosphate by Fbp1 through enzymatic conversion of 2-amino-6-mercapto-7-methyl-purine riboside (MESG) to ribose 1-phosphate and 2-amino-6-mercapto-7-methylpurine by purine nucleoside phosphorylase (PNP). This leads to a shift in maximum absorbance from 330 nm for MESG to 360 nm for the final reaction product (2-amino-6-mercapto-7-methylpurine).

To obtain fully ubiquitylated Fbp1, it was subjected to an overnight multiturnover ubiquitylation reaction at room temperature consisting of 0.2 μM Uba1, 1 μM Ubc8, 0.5 μM GID^{Ant}, 1 μM Gid4, 2 μM Gid7, 10 μM Fbp1-V5-2xS and 100 μM 6xHis-3c-Ub. The reaction mix was run on SEC (using Superose 6 column) to separate different components of the assay. Fractions corresponding to the ubiquitylated Fbp1 were pooled and incubated with Ni-NTA resin for 30 minutes. After throughout wash, the bound protein was eluted and visualized by SDS-PAGE.

Fbp1 activity assays were performed according to the manufacturer's instructions at room temperature. First, all the reagents provided in the assay kit (MESG, PNP and 20x reaction buffer), 0.5 mM fructose-1,6-bisphosphate substrate and 0.6 mM AMP (only for the Fbp1 inhibition assay) were pre-mixed and incubated for 5 min. Then, the reaction was initiated by addition of 53 nM of the WT, target lysine mutant (K32A/K35A/K280A/K281A) or fully ubiquitylated Fbp1, and the reaction progress was followed by measuring a time-course of absorbance at 360 nm (A₃₆₀, absorbance of the final reaction product) using CLARIOStar Plus microplate reader (BMG LABTECH) in a UV-transparent 96-well plate. The values of A₃₆₀ obtained for the buffer-only control were subtracted from all the experimental measurements, which were then plotted in GraphPad Prism.

Analysis of global proteome of WT versus ΔGid7 yeast (Karayel et al., 2020)

To test which proteins are dependent on Gid7 for their *in vivo* degradation, we compared the global proteome of WT with that of the ΔGid7 yeast (Figure S1F). Cells were grown in SD media to an OD of 1-1.5, pelleted by centrifugation, washed in pre-warmed SE media, and resuspended to an OD of 1 in fresh, pre-warmed SE media. Cultures were then allowed to grow at 30°C for 18 hours, after which cells were again pelleted by centrifugation, and resuspended in fresh, pre-warmed SD media to an OD of 1. Following growth at 30°C for 2 hours, 50 ODs of cells were pelleted by centrifugation, flash frozen and stored at -80°C until lysis. The frozen pellets were mixed with SDC lysis buffer (1% SDC and 100 mM Tris pH 8.5) and immediately heat-treated for 5 minutes at 95°C. Lysates were homogenized by sonication at 4°C using a Bioruptor and then diluted to achieve equal protein concentrations in a 96-well plate. Samples were next incubated for 5 minutes at 45°C with 40 mM CAA and 10 mM TCEP for reduction and alkylation and digested overnight at 37°C using trypsin (1:100 w/w, Sigma-Aldrich) and LysC (1/100 w/w, Wako). Next day, peptide material was desalted using SDB-RPS StageTips (Empore) (Kulak et al., 2014) and resuspended in buffer A (0.2% TFA/2% ACN). Peptide concentrations were measured by absorbance at 280 nm (Nanodrop 2000, Thermo Scientific) and equalized using buffer A*. 300 ng peptides were subjected to LC-MS/MS analysis.

Samples were loaded onto a 20 cm reversed phase column (75 μm inner diameter, packed in house with ReproSil-Pur C18-AQ 1.9 μm resin (Dr. Maisch GmbH)). The column temperature was maintained at 60°C using a homemade column oven. A binary buffer system, consisting of buffer I (0.1% formic acid (FA) and buffer II (80% ACN plus 0.1% FA), was used for peptides separation, at a flow rate of 450 nL/min. An EASY-nLC 1200 system (Thermo Fisher Scientific), directly coupled online with the mass spectrometer (Q Exactive HF-X, Thermo Fisher Scientific) via a nano-electrospray source, was employed for nano-flow liquid chromatography. We used a gradient starting at 5% buffer B, increased to 35% in 18 and a half minute, 95% in a minute and stayed at 95% for three and a half min. The mass spectrometer was operated in DIA mode. Full MS resolution was set to 120,000 with a full scan range of 300-1650 m/z, a maximum fill time of 60 ms and an automatic gain control (AGC) target of 3e6. One full scan was followed by 12 windows with a resolution of 30,000 in profile mode. Precursor ions were fragmented by stepped higher-energy collisional dissociation (HCD) (NCE 25.5, 27,30%).

Spectronaut version 13 (Biognosys) was used to analyze DIA raw files using the yeast FASTA file (Swissprot, 2018) and the proteome library previously published (Karayel et al., 2020) with default settings and enabled cross run normalization. The Perseus software package version 1.6.0.7 was used for the data analysis (Tyanova et al., 2016). Protein intensities were log₂-transformed and filtered to make sure that identified proteins showed expression in all biological triplicates of at least one condition. The missing values were subsequently replaced by random numbers that were drawn from a normal distribution (width = 0.3 and down shift = 1.8). For volcano plots, we used permutation-based FDR, which was set to 0.05 in conjunction with an S0-parameter of 0.1 to determine the significance.

Determination of preferentially targeted lysines in Fbp1 by LC-MS/MS (Figure S5)

To determine the preferentially targeted lysines in Fbp1, it was ubiquitylated by Chelator-GID^{SR4} and subjected to proteomic analysis. To capture the initial ubiquitylation events, the assay was performed in a single-turnover pulse-chase format, wherein the concentration of the substrate was significantly exceeding that of E2~Ub. In the pulse, 10 μM Ubc8 was loaded with 30 μM lysine-less ubiquitin mutant (all K > R) and 0.5 μM Uba1 for 15 minutes at room temperature and quenched with 50 mM EDTA. To start the chase, the pulse reaction was mixed with an equal volume of the chase-initiating mixture containing 1 μM GID^{Ant}, 2 μM Gid7, 2 μM Gid4 and 4 μM Fbp1-6xHis and incubated at room temperature. After 1 minute, the reaction was quenched by adding 10 mM DTT, which was then removed by desalting before proteomic analysis.

Proteins were digested and prepared for LC-MS/MS measurements as previously described (Qiao et al., 2020). Briefly, samples were diluted in digestion buffer (1 M urea in 50 mM ammonium bicarbonate, pH 8.0), followed by addition of TCEP and CAA to a final concentration of 10 mM and 40 mM, respectively. After reduction and alkylation for 5 minutes at 45°C, samples were enzymatically digested using either trypsin (1:20 w/w, Sigma-Aldrich) alone, trypsin (1:40 w/w)/GluC (1:40 w/w, BioLab) or trypsin (1:40 w/w)/AspN (1:40 w/w, Promega) at 37°C overnight. Thereafter, protease activity was quenched and peptides were loaded and cleaned on SDP-RPS StageTips. Peptides were subsequently eluted with 1.25% ammonium hydroxide/80% ACN, dried using a SpeedVac centrifuge (Eppendorf, Concentrator plus) and resuspended in buffer A (2% ACN/0.1% TFA) for LC/MS-MS analysis.

Peptide concentration was estimated by UV spectrometry and approximately 200 ng were loaded on a 50 cm reversed phase column (75 μ m inner diameter, packed in-house with ReproSil-Pur C18-AQ 1.9 μ m resin (Dr. Maisch GmbH)). Column temperature was maintained at 60°C using a homemade column oven. Peptides were separated with a binary buffer system of buffer A (0.1% formic acid (FA)) and buffer B (80% acetonitrile plus 0.1% FA), at a flow rate of 300 nl/min. We used an EASY-nLC 1200 system (Thermo Fisher Scientific), which was directly coupled online with the mass spectrometer (Q Exactive HF-X, Thermo Fisher Scientific) via a nano-electrospray source. Peptides were eluted with a gradient starting at 3% buffer B and stepwise increased to 8% in 8 min, 36% in 32 min, 45% in 4 minutes and 95% in 4 min. The mass spectrometer was operated in Top12 data-dependent mode (DDA) with a full scan range of 250–1350 m/z at 60,000 resolution with an automatic gain control (AGC) target of 3e6 and a maximum fill time of 20 ms. Precursor ions were isolated with a width of 1.4 m/z and fragmented by higher-energy collisional dissociation (HCD) with a normalized collision energy (NCE) of 28%. Fragment scans were performed at a resolution of 30,000, an AGC of 1e5 and a maximum injection time of 110 ms. Dynamic exclusion was enabled and set to 15 s.

Raw MS data were searched against UniProt Yeast FASTA using MaxQuant (version 1.6.2.10) with a 1% FDR at peptide and protein level. Cysteine carbamidomethylation was set as fixed, protein N-terminal acetylation, methionine oxidation and lysine diGly as variable modifications. The minimum peptide length was set to 7 amino acids, enzyme specificity was set to trypsin and two missed cleavages were allowed, permitting a maximum of 5 modifications per peptide. MS/MS spectra identifying ubiquitylated peptides of interest were obtained and exported using MaxQuant Viewer.

Cell culture and generation of CRISPR-Cas9 knock out cell lines

K562 erythroleukemia cell line was obtained from ATCC (CCL-243TM) and cultured in IMDM completed with 10% (v/v) FBS (GIBCO) and antibiotics (100 units/ml penicillin, 0.1 mg/ml streptomycin, GIBCO). Cell densities were kept between $0.1-1 \times 10^6$ cells/mL, and cultures were regularly checked for the absence of mycoplasma contamination. For CRISPR-Cas9(D10A) nickase-mediated functional knockouts of MAEA, MKLN1 and WDR26, paired sense and antisense guide RNAs (gRNA) were designed to target MAEA in exon 2, exon 5 in MKLN1 and exon 1 in WDR26 genetic locus. Sense and antisense gRNA were cloned into pBABED-U6-Puromycin plasmid (gift from Thomas Macartney, University of Dundee, UK) and pX335-Cas9(D10A) (Addgene) (Cong et al., 2013), respectively. K562 cells were co-transfected with vectors encoding the pair of gRNAs using Lipofectamine LTX reagent (Invitrogen) following manufacturer's instructions. Twenty-four hours after transfection, cells were selected in puromycin (2 μ g/ml) for 2 days, followed by expansion, and single-cell dilution to obtain cell clones. Successful knockout clones were confirmed by immunoblotting and genomic sequencing of targeted loci (Figure S6J).

Human cell lysate fractionation by sucrose density gradient

1×10^7 cells were harvested by centrifugation at 360 x g, washed once with ice-cold PBS, and resuspended in lysis buffer (40 mM HEPES pH 7.5, 120 mM NaCl, 1 mM EGTA, 0.5% NP40, 1 mM DTT, and Complete protease inhibitor mix (Roche)). Cells were homogenized by pushing them 10 times through a 23G syringe. The obtained lysate was cleared by centrifugation at 23,000 x g for 30 minutes at 4°C. 3 mg of total protein were loaded on top of a 5%–40% sucrose gradient (weight/volume, in lysis buffer) and centrifuged in a SW60 rotor at 34,300 rpm for 16 hours at 4°C. Fractions were collected from top of the gradient and separated by SDS-PAGE, followed by immunoblotting using the following antibodies: RMND5A (Santa Cruz), MAEA (R&D systems), RANBP9 (Novus Biologicals), TWA1 (Thermo Fisher), ARMC8 (Santa Cruz), WDR26 (Bethyl Laboratories), MKLN1 (Santa Cruz) and YPEL5 (Thermo Fisher). Antibodies that recognize hGid4 were generated by immunizing sheep with bacterially expressed GST-hGid4 (Δ 1–99). Western blots were developed using Clarity Western ECL Substrate (BioRad) and imaged using Amersham Imager 600 (GE Lifesciences).

Cryo EM sample preparation and imaging

Cryo EM grids were prepared using Vitrobot Mark IV (Thermo Fisher Scientific) operated at 4°C and 100% humidity. 3.5 μ l of freshly purified proteins at 0.3–0.5 mg/ml were applied to glow-discharged Quantifoil holey carbon grids (R1.2/1.3 200 mesh). Grids were immediately blotted with Whatman no. 1 filter paper (blot time: 3 s, blot force: 3) and vitrified by plunging into liquid ethane.

Cryo EM data were first screened and collected on a Talos Arctica or Glacios transmission electron microscope (Thermo Fisher Scientific) operated at 200 kV, equipped with a Falcon III (Thermo Fisher Scientific) or K2 (Gatan) direct electron detector, respectively. Automated data collection was carried out using EPU software (Thermo Fisher Scientific) or SerialEM (Mastronarde, 2003). High-resolution datasets were collected on a Titan Krios (Thermo Fisher Scientific) microscope operated at 300 kV, equipped with a post-column GIF and a K3 Summit direct electron detector (Gatan) operating in a counting mode. SerialEM was used to automate data collection (Mastronarde, 2003). Details of cryo EM data collection and map refinement are listed in Table S1.

Cryo EM data processing

Frames were motion-corrected with dose weighting using MotionCorr2 (Zheng et al., 2017) and subjected to estimation of contrast transfer function parameters with Gctf (Zhang, 2016). Auto-picking of particles was performed with Gautomatch (<https://www.mrc-lmb.cam.ac.uk/kzhang/>) and for most datasets, it was aided by provision of a template obtained from previous low-resolution datasets. For Titan Krios datasets, movies were being pre-processed on-the-fly during data collection with Focus (Biyani et al., 2017), which also automatically discarded poor quality images. All the subsequent stages of data processing were carried out with Relion (Fernandez-Leiro and Scheres, 2017; Scheres, 2012; Zivanov et al., 2018). To clean up the data, extracted particles were subjected to either several rounds of 2D classification, followed by a 3D classification or submitted directly to a masked 3D classification. The chosen subset of particles was subjected to auto-refinement without and with a mask. To improve the quality of maps obtained after consensus refinement, a 3D classification without particle alignment was performed and a class having the most complete features was selected.

High-resolution maps of yeast substrate receptor scaffolding (SRS), catalytic (Cat) and supramolecular assembly (SA) modules were obtained from the Chelator-GID^{SR4} dataset with its substrate Fbp1 bound. For the SRS module, a more resolved half of the Chelator-GID^{SR4} was first auto-refined and a focused 3D classification without particle alignment was performed with a mask over GID^{SR4}. Then, focused refinement was performed, wherein the Cat module was masked out. For Cat and SA modules, the number of particles used for alignment was doubled by taking advantage of the Chelator-GID^{SR4} having C2 symmetry. First, the map of the entire complex was auto-refined with C2 symmetry imposed and masks were created for each of its halves. Then, the signal for each half was separately subtracted and the resulting semi-elliptical particles were aligned by auto-refinement. After masking out the SRS module, a focused 3D classification without particle alignment was performed separately for Cat and SA modules. After one more round of 3D classification without particle alignment with a higher T-value, the particles were subjected to CTF refinement and final auto-refinement.

For high-resolution CTLH^{SR4} dataset, the density corresponding to the catalytic module (RMND5A-MAEA) was masked out due to its mobility relative to the substrate receptor scaffolding module (RANBP9-TWA1-ARMC8-hGid4). For visualization of less resolved parts of the map, such as RANBP9^{LisH-CRAC}-TWA1 as well as the N- and C-termini of ARMC8, subsequent rounds of focused 3D classifications with masks over these regions were carried out. The final auto-refinement was preceded by a CTF refinement.

All maps were post-processed by automatic B-factor weighting and high-resolution noise substitution in Relion. In addition, to aid in building atomic models, the refined maps of the Chelator-GID^{SR4} SA module and CTLH^{SR4} SRS module were post-processed with DeepEMhancer (Sanchez-Garcia et al., 2020) and are deposited as additional maps in EMDB. The estimated resolutions of all reconstructions are based on the gold-standard Fourier Shell Correlation (FSC) at 0.143 criterion. Simplified schematic of processing for both Titan Krios datasets are presented in Figures S4 and S7 (for Chelator-GID^{SR4} and CTLH^{SR4}, respectively).

Model building and refinement

Manual building of all models was performed with Coot (Emsley and Cowtan, 2004; Emsley et al., 2010), whereas structure visualization and analysis was carried out with Chimera (Pettersen et al., 2004), ChimeraX (Goddard et al., 2018) and Pymol-v2.1 (<https://pymol.org/2/>).

The atomic model of CTLH substrate receptor scaffolding module was prepared as follows. Most of ARMC8 was built automatically with Buccaneer (Cowtan, 2006) and refined manually with Coot. The model of the substrate receptor hGid4 was generated by docking its crystal structure (PDB: 6CDC) into the EM map and manual building of its N- and C-termini. The crystal structure of RANBP9 SPRY domain (PDB: 5J17) was fitted into the electron density map and served as a starting point for manual building of its downstream region. Manual building of TWA1 was guided by fitting parts of its homology model into the map (generated by SWISS-MODEL (Waterhouse et al., 2018), based on the structure of yeast Gid8 in Gid^{SR4}, PDB: 6SWY) and secondary structure prediction obtained from Phyre² server (Kelley et al., 2015).

The structure of the SRS module in Chelator-GID^{SR4} was generated by fitting the atomic coordinates of the corresponding part of GID^{SR4} (PDB: 6SWY) and manual refinement. The loops of Gid4 surrounding its substrate-binding cavity as well as Fbp1 degron were built manually. Coordinates of most of Gid8 and Gid1 in the SA module were fitted from the structure of GID^{SR4} and the missing or differing parts, such as Gid1 CTLH-CRA^N, were built manually. The LisH-CRA^C as well as CTLH-CRA^N domains of Gid7 were built manually, guided by secondary structure predictions. Manual building of Gid7 β -propellers was aided by their homology model from Phyre² (Kelley et al., 2015). All of the Cat module was built manually and the geometry of the zinc binding site was constrained to account for tetrahedral coordination of zinc ions.

All the models were subjected to iterative rounds of manual building with Coot and real space refinement in PHENIX (Adams et al., 2010; Afonine et al., 2018; DiMaio et al., 2013) until a satisfactory model quality, in terms of its geometry and agreement with the map, was obtained.

Fbp1 crystallization and data processing

Crystallization trials of Fbp1-6xHis were performed in the MPIB Crystallization Facility. Before setting up the crystallization trays, the purified Fbp1 was concentrated to 12 mg/mL and combined with 0.5 mM of its allosteric inhibitor AMP and the substrate fructose-1,6-bisphosphate. Crystals used for X-ray data collection were obtained at 4°C in the buffer containing 16% PEG 3350, 0.2 M MgCl₂

and 0.1 M Bis-Tris pH 6 using a vapor diffusion method performed in a sitting-drop format. Crystals were cryoprotected using 20% ethylene glycol and stored by flash freezing in liquid nitrogen until data collection.

Diffraction dataset was recorded at X10SA beam line, Swiss Light Source (SLS) in Villigen, Switzerland. Data were recorded at 0.5 degree rotation intervals using Dectris Pilatus 2M-F detector. Data were indexed, integrated, and scaled using XDS package to a resolution limit of 1.95 Å. Phasing was performed through molecular replacement using a structure of human Fbp1 (PDB: 1FTA) with PHASER integrated into the PHENIX software suite (Adams et al., 2010; Afonine et al., 2018; DiMaio et al., 2013). Model building was done using Coot (Emsley and Cowtan, 2004; Emsley et al., 2010), whereas refinement was carried out with phenix.refine. Details of X-ray diffraction data collection and refinement statistics are listed in Table S2.

QUANTIFICATION AND STATISTICAL ANALYSIS

For the assays described in the section “*In vivo* yeast substrate degradation assays,” protein bands visualized by western blots were quantified using ImageStudioLite software (Li-Cor). For statistical analysis, at least three biological replicates were considered and the standard deviation of the replicates was presented using error bars.

Fluorescently labeled proteins in *in vitro* ubiquitylation reactions were quantified in ImageQuant (GE Healthcare) and the calculated fractions of ubiquitylated substrates were plotted in GraphPad Prism. All *in vitro* assays were performed in at least duplicates and the standard deviation represented by error bars are shown wherever necessary. For determination of K_m for Fbp1 ubiquitylation by GID E3 with kinetics, the fraction of ubiquitylated Fbp1 was fit to the Michaelis-Menten equation in GraphPad Prism. k_{cat} was calculated based on a slope of a linear phase of Fbp1 ubiquitylation reaction fitted in GraphPad Prism.

2.2. Multifaceted N-degron recognition and ubiquitylation by GID/CTLH E3 ligases (Chrustowicz and Sherpa, et al. Journal of Molecular Biology, 2021)

This section includes my second co-first author paper that has been reprinted according to the permission from the Elsevier (licensed by Creative Commons). A brief summary and my contributions to this project are listed below.

Here using diverse approaches such as phage display, binding assays and X-ray crystallography, we have elucidated mechanisms of how a singular GID/CTLH E3 ligase substrate receptor can target diverse substrates with varying degron sequences. We have shown that the substrate binding domains of yeast *Gid4*, yeast *Gid11* and human *Gid4* have malleable loops that allow the binding pocket to adjust according to different degron/ peptide sequences bound. Moreover, we have identified novel peptide binders that have non-proline residues at their N-terminus with higher binding affinities compared to natural degrons. Overall, our study demonstrates how ubiquitylation of GID substrates rely on their substrate degron affinities, availability of target lysine sites and higher-order assembly of the GID E3 ligase.

In particular, for this paper I contributed the following experiments:

- Preparation of experimental materials, planning of individual experiments, manuscript preparation
- Preparation of samples for NMR experiments (Fig. 1A), fluorescence polarization experiments (1B), sample preparation for phage display (Fig. 2B, 4A, 4B), Isothermal titration calorimetry experiments (Fig. 2C), peptide spot array assays (Fig. S1C), in vivo degradation assays (Fig. 6C, 6D, S4B), sample preparation, optimization and determination of crystal structure of hGid4 (Fig. 1C, PDB ID: 7Q4Y)

Publisher: Elsevier

Copyright © 1969, Elsevier

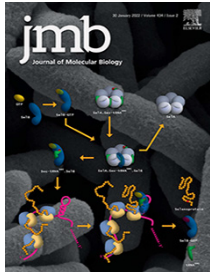
Creative Commons

This is an open access article distributed under the terms of the [Creative Commons CC-BY](#) license, which permits unrestricted use, distribution, and reproduction in any medium, provided the original work is properly cited.

You are not required to obtain permission to reuse this article.

To request permission for a type of use not listed, please contact [Elsevier](#) Global Rights Department.

Are you the [author](#) of this Elsevier journal article?



Multifaceted N-Degron Recognition and Ubiquitylation by GID/CTLH E3 Ligases

Jakub Chrustowicz^{1†}, Dawafuti Sherpa^{1†}, Joan Teyra², Mun Siong Loke¹, Grzegorz M. Popowicz^{4,5}, Jerome Basquin⁶, Michael Sattler^{4,5}, J. Rajan Prabu¹, Sachdev S. Sidhu^{2,3} and Brenda A. Schulman^{1*}

1 - Department of Molecular Machines and Signaling, Max Planck Institute of Biochemistry, 82152 Martinsried, Germany

2 - The Donnelly Centre, University of Toronto, Toronto, ON M5S 3E1, Canada

3 - Department of Molecular Genetics, University of Toronto, Toronto, ON M5S 1A8, Canada

4 - Helmholtz Zentrum München, Ingolstädter Landstrasse 1, 85764 Neuherberg, Germany

5 - Bavarian NMR Center, Department of Chemistry, Technical University of Munich, Germany

6 - Department of Structural Cell Biology, Max Planck Institute of Biochemistry, 82152 Martinsried, Germany

Correspondence to Brenda A. Schulman: schulman@biochem.mpg.de (B.A. Schulman)

[@dawafutisherpa](https://twitter.com/dawafutisherpa) (D. Sherpa), [@chrustowicz_j](https://twitter.com/chrustowicz_j) (J. Chrustowicz), [@rajanprabu](https://twitter.com/rajanprabu) (J.R. Prabu)

<https://doi.org/10.1016/j.jmb.2021.167347>

Edited by Igor Stagljar

Abstract

N-degion E3 ubiquitin ligases recognize specific residues at the N-termini of substrates. Although molecular details of N-degion recognition are known for several E3 ligases, the range of N-terminal motifs that can bind a given E3 substrate binding domain remains unclear. Here, we discovered capacity of Gid4 and Gid10 substrate receptor subunits of yeast “GID”/human “CTLH” multiprotein E3 ligases to tightly bind a wide range of N-terminal residues whose recognition is determined in part by the downstream sequence context. Screening of phage displaying peptide libraries with exposed N-termini identified novel consensus motifs with non-Pro N-terminal residues binding Gid4 or Gid10 with high affinity. Structural data reveal that conformations of flexible loops in Gid4 and Gid10 complement sequences and folds of interacting peptides. Together with analysis of endogenous substrate degions, the data show that degion identity, substrate domains harboring targeted lysines, and varying E3 ligase higher-order assemblies combinatorially determine efficiency of ubiquitylation and degradation.

© 2021 The Author(s). Published by Elsevier Ltd. This is an open access article under the CC BY license (<http://creativecommons.org/licenses/by/4.0/>).

Introduction

Specificity of ubiquitylation depends on E3 ligases recognizing motifs, termed “degions”, in substrates to be modified. The first such motif to be identified was the N-terminal sequence - now called N-degion¹ - in substrates of the yeast E3 ligase Ubr1.^{2,3} Subsequently, several E3 ligases in different families were discovered to recognize protein N-termini as degions. Higher eukaryotes have one HECT-type and several

RING-family E3s with “Ubr” domains homologous to those in yeast Ubr1 that either have been shown to or are presumed to recognize distinct N-terminal sequences.^{4,5} Other N-degion-recognizing ubiquitin ligases were identified either through characterizing substrate sequences mediating E3-binding,^{6,7} or through systematic genetic screens matching human protein N-terminal sequences with E3 ligases.⁸ Some of the best-studied pathways recognize sequences with an N-terminal Arg,⁹ Pro^{6,10} or Gly^{8,11} (termed

Arg/N-degron, Pro/N-degron or Gly/N-degron, respectively), or acetylated N-terminus.^{12–15}

An N-degron-recognizing E3 of emerging importance is a suite of related multiprotein complexes termed “GID” in budding yeast (named due to mutations causing glucose-induced degradation deficiency of fructose-1,6-bisphosphatase, Fbp1)^{7,16–20} or “CTLH” in higher eukaryotes (named due to preponderance of subunits containing CTLH motifs).²¹ The yeast GID E3 mediates degradation of gluconeogenic enzymes Fbp1, Mdh2 and Icl1 during recovery from carbon starvation.⁷ The GID E3 recognizes the N-terminal Pro in these substrates generated by cleavage of the initiator methionine.^{6,7} In higher eukaryotes, corresponding CTLH complexes are involved in diverse biological processes including erythropoiesis, organ development, embryogenesis, and cell division.^{22–32} However, the mechanistic roles of CTLH-mediated ubiquitylation in these pathways remain largely mysterious.

Recent genetic, biochemical and structural studies have revealed that the GID E3 is not a singular complex. Rather a core GID^{Ant} complex (comprising Gid1, Gid5, Gid8, Gid2, Gid9 subunits) essentially anticipates shifts in environmental conditions that stimulate expression of interchangeable and mutually exclusive substrate-binding receptors – Gid4 (termed “yGid4” for yeast Gid4 hereafter),^{17,33,34} Gid10 (yGid10 hereafter)^{34–36} and Gid11 (yGid11 hereafter).³⁷ Whereas yGid4 is expressed after glucose has been restored to carbon-starved yeast, yGid10 and yGid11 are upregulated upon other environmental perturbations including heat shock, osmotic stress as well as carbon, nitrogen and amino acid starvation. The resultant E3 complexes, GID^{SR4}, GID^{SR10}, and GID^{SR11} (where SR# refers to Gid substrate receptor), recognize distinct N-terminal sequences of their substrates.^{6,7,34,35,37} In addition, another subunit, Gid7, can drive supramolecular assembly of two GID^{SR4} units into a complex named Chelator-GID^{SR4} to reflect its resemblance to an organometallic chelate capturing a smaller ligand through multiple contacts.³⁸ The cryo EM structure of a Chelator-GID^{SR4} complex with Fbp1 showed two opposing Gid4 molecules avidly binding N-degrons from different Fbp1 protomers. As such, Fbp1 is encapsulated within the center of the oval-shaped Chelator-GID^{SR4}. This assembly positions functionally-relevant target lysines from multiple Fbp1 protomers adjacent to two Chelator-GID^{SR4} catalytic centers.

The molecular details of GID/CTLH recognition of Pro/N-degrons were initially revealed from crystal structures of human Gid4 (referred to as hGid4 hereafter) bound to peptides with N-terminal prolines.¹⁰ Although Pro/N-degron substrates of the CTLH E3 remain unknown, hGid4 is suitably well-behaved for biophysical and structural characterization, whereas yGid4 has limited solubility on its own.¹⁰ Previously, the sequence PGLWKS was

identified as binding hGid4 with highest affinity amongst all sequences tested, with a K_D in the low micromolar range.¹⁰ The crystallized peptide-binding region of hGid4, which superimposes with the substrate-binding domains of yGid4 and yGid10 in GID^{SR4} and GID^{SR10}, adopts an 8-stranded β -barrel with a central tunnel that binds the N-terminus of a peptide, or of the intrinsically-disordered N-terminal degron sequence of a substrate.^{10,34,36,38,39} Loops between β -strands at the edge of the barrel bind residues downstream of the peptide’s N-terminus. Interestingly, although GID^{SR4} was originally thought to exclusively bind peptides with an N-terminal Pro, hGid4 can also bind peptides with non-Pro hydrophobic N-termini such as Ile or Leu, albeit with at best ≈ 8 -fold lower affinity.³⁹ Furthermore, yGid11 is thought to use a distinct structure to recognize substrate Thr/N-degrons.³⁷ Collectively, these findings suggested that the landscape of GID/CTLH E3 substrates can extend beyond Pro/N-degron motifs.

Here, phage display screening identified peptides with various non-Pro N-termini that not only bind hGid4, yGid4 and yGid10, but do so with comparable or higher affinity than the previously identified Pro-initiating sequences including Pro/N-degrons of ubiquitylation substrates. Structural data reveal that loops in GID/CTLH substrate-binding domains adopt conformations complementary to partner peptide sequences downstream of the N-terminus. Thus, sequence context is a determinant of N-terminal recognition by GID/CTLH substrate-binding domains. In the context of natural substrates recognized by yGid4, not only the degron but also the associated domain harboring targeted lysine contribute to ubiquitylation by the core GID^{SR4} and its superassembly.

Results

hGid4 can bind peptides with a range of N-terminal sequences

We took advantage of the amenability of hGid4 to biophysical characterization to further characterize features of the PGLWKS sequence mediating interactions. To assess the importance of peptide length beyond the N-terminus, we examined chemical shift perturbations (CSPs) in 2D ¹H, ¹⁵N-HSQC NMR spectra of [¹⁵N]-labeled hGid4 mixed with the amino acid Pro, a Pro-Gly dipeptide, or the PGLWKS peptide (Figure 1(A)). Although prior studies emphasized the importance of an N-terminal Pro,^{10,39} Pro alone only minimally influenced the spectrum. The Pro-Gly dipeptide elicited stronger CSPs, presumably due to the peptide bond directly interacting with hGid4, and suppressing repulsion by burying the negatively charged carboxylate of a single Pro in a hydrophobic environment (Figure S1(A)). The PGLWKS peptide showed the greatest CSPs and binding kinetics in the slow exchange regime at the NMR chemical shift

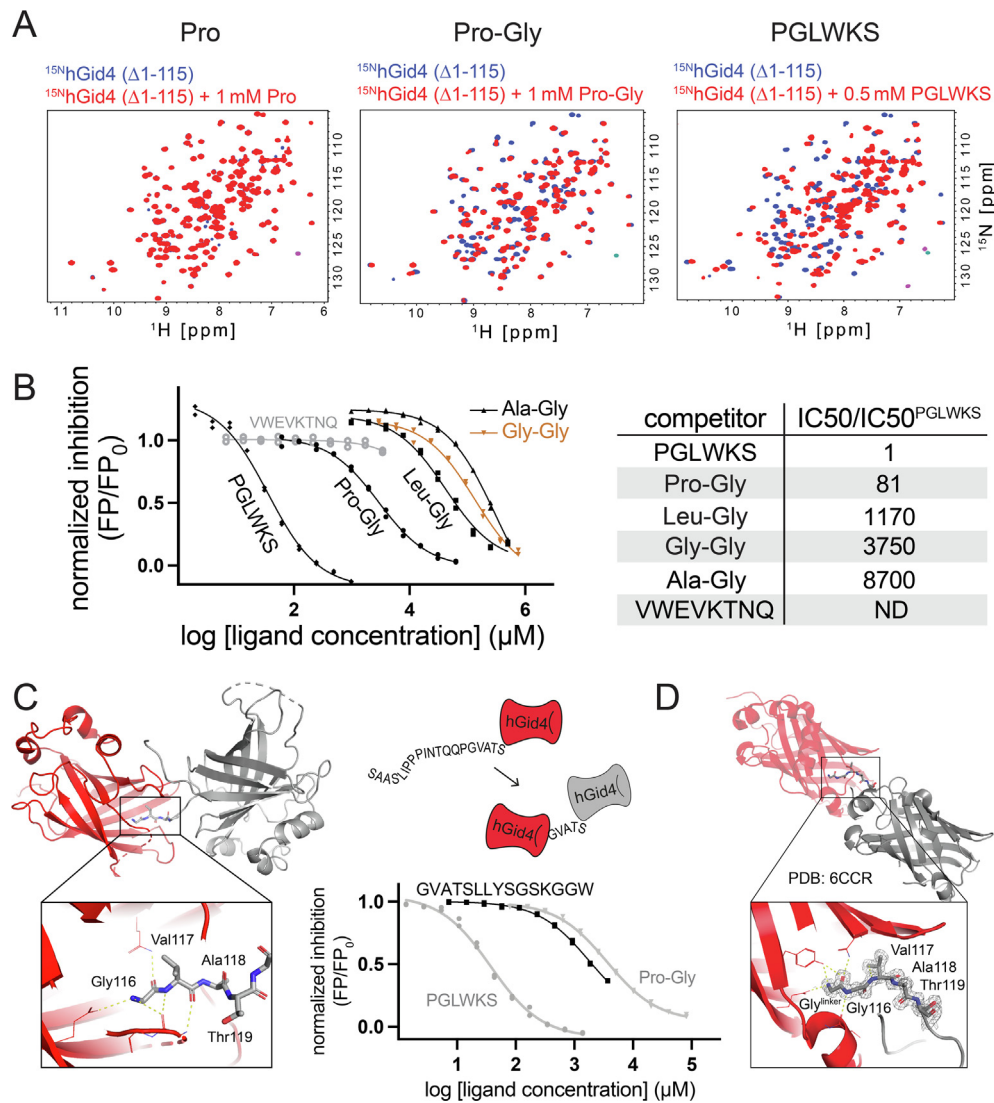


Figure 1. hGid4 recognizes various peptide N-termini and several downstream residues. A. Overlaid ^1H , ^{15}N -HSQC NMR spectra of 0.1 mM [^{15}N]-labeled 6xHis-hGid4 ($\Delta 1-115$) alone (blue) and upon addition of 1 mM Pro, 1 mM Pro-Gly or 0.5 mM PGLWKS peptide (red). B. Competitive fluorescence polarization (FP) experiments comparing different unlabeled ligands for inhibiting hGid4 ($\Delta 1-115$) binding to C-terminally fluorescein-labeled PGLWKS peptide. Ratios of FP signals at varying concentrations of unlabeled ligands to that in the absence of a competitor (FP/FP_0) were plotted as a function of $\log[\text{ligand concentration}]$ (left). Half-maximal inhibitory concentrations (IC_{50}) for each ligand were determined by fitting to $\log[\text{inhibitor}]$ vs. response model and presented relative to IC_{50} of the unlabeled PGLWKS peptide (right). The peptide VWEVKTNQ corresponding to the N-terminus of Hbp1 (2–9) that is not an hGid4 substrate⁸⁸ was included as a negative control. C. Crystal structure of one hGid4 (red) accommodating serendipitously generated Gly116-initiating N-terminus of an adjacent hGid4 molecule (grey) in the crystal lattice. The binding strength of the newly generated N-terminal sequence (116–127) to hGid4 was compared to that of PGLWKS and Pro-Gly with competitive FP (right bottom). D. Previously published hGid4 crystal structure (PDB ID: **6CCR**) revealing one hGid4 binding the N-terminus bearing an additional Gly upstream Gly116 derived from cloning of an adjacent hGid4 molecule (grey) in the lattice of a distinct crystal form.

time scale, indicating tight binding, and, therefore, importance of downstream residues.

Given the ability of a Pro-Gly dipeptide to bind hGid4, we examined importance of the N-terminal residue by testing commercially-available variants (Leu-Gly, Ala-Gly, and Gly-Gly along with Pro-Gly)

for competing with a fluorescently-labeled PGLWKS peptide whose binding to hGid4 can be measured by fluorescence polarization (FP) (Figure S1(B)). Although each of the dipeptides yielded sigmoidal curves, those with N-terminal Pro or Leu were superior (Figure 1(B)). Pro-Gly

showed a 15-fold lower IC_{50} than Leu-Gly, consistent with prior studies emphasizing the importance of an N-terminal Pro.³⁹

To examine roles of individual positions in the 6-residue PGLWKS sequence, we employed peptide spot arrays testing all natural amino acids in position 1, positions 2 and 3 together, position 4 or position 5 (Figure S1(C)). Binding was detected after incubating the membranes with the substrate binding domain of hGid4, and immunoblotting with anti-hGid4 antibodies. Overall, the data confirm the previous findings that out of the peptides tested PGLWKS is an optimal binder, and that N-terminal non-Pro hydrophobic residues are tolerated in the context of the downstream GLWKS sequence albeit with lower binding.^{10,39}

The peptide array data also highlighted the importance of context. Amongst the 400 possible combinations of residues 2 and 3, Gly, and to a lesser extent Ser, Val and Ala are preferred at position 2 and Ile or Leu at position 3, mirroring the previously defined sequence preferences.¹⁰ The dynamic range of our assay suggested that downstream residues also contribute to specificity, by unveiling pronounced amino acid preference for bulky hydrophobics and some non-hydrophobic residues also at position 4. In agreement with the structural data,¹⁰ the 5th position following the PGLW sequence tolerates many amino acids.

Despite this seemingly strong preference for an N-terminal Pro, we serendipitously visualized hGid4 recognizing a supposedly non-cognate sequence when we set out to visualize its structure in the absence of a peptide ligand by X-ray crystallography. Unexpectedly, the electron density from data at 3 Å resolution showed the first visible N-terminal residue of one molecule of hGid4 inserted into the substrate binding tunnel of an adjacent hGid4 molecule in the crystal lattice (Figure 1(C); Table S1). Perplexingly, this was not the first residue of the input hGid4 construct but Gly116 located 16 positions downstream. It appears that hGid4 underwent processing during crystallization, although it remains unknown if this neo-N-terminus was generated through enzymatic cleavage by a contaminating bacterial protease or chemical processing. Nonetheless, the potential for hGid4 to recognize a non-cognate N-terminal Gly was supported by re-examination of the published “apo” hGid4 crystal. In the previous structure of hGid4 (PDB ID: **6CCR**), distinct crystal packing is also mediated by a peptide-like sequence (initiating with a Gly from the Tobacco Etch Virus (TEV) protease cleavage site, followed by hGid4 Gly116) inserting into the substrate binding tunnel of the neighboring molecule in the lattice (Figure 1(D)). The positions and interactions of the two N-terminal Gly are similar but not identical, as hGid4's Tyr258 does not hydrogen bond to the N-terminal amine of Gly116 in our structure.

To test binding of our fortuitously identified hGid4-binding sequence in solution, we examined competition with the fluorescently-labeled PGLWKS peptide (Figure 1(C)). Limited solubility of the GVATSLLYSGSKGGW peptide (hGid4 residues 116–127, with C-terminal Trp appended with a Gly-Gly linker to accurately measure peptide concentration) precluded accurate measurement of IC_{50} using our competitive FP assay. Nonetheless, the data qualitatively indicated that the GVATSLLYSGSKGGW peptide binds to hGid4 with significantly lower affinity than PGLWKS, but more tightly than the Pro-Gly dipeptide. Therefore, we speculate that these structurally-observed interactions were favored by the high concentration of protein during crystallization.

Taken together with published work, the data confirmed hGid4's preference for binding to the previously-defined sequence PGLWKS, but they also highlighted capacity for hGid4 to recognize alternative N-termini. Moreover, given that specific combinations of residues downstream of the Pro-Gly substantially impact the interaction, we considered the possibility that hGid4 recognition of N-terminal sequences could be influenced by context.

Identification of superior hGid4-binding motifs not initiated by Pro

To discover alternative hGid4-binding sequences that do not initiate with Pro, we constructed a highly diverse N-terminal peptide phage-displayed library of 3.5×10^9 random octapeptides. The library was constructed after the signal peptide using 8 consecutive NNK degenerate codons encoding for all 20 natural amino acids and fused to the N-terminus of the phage coat protein. It is expected that Arg or Pro located next to the cleavage site (position + 1) will be inexistent or strongly underrepresented because they are known to either inhibit the secretion of phages^{40,41} or the signal peptidase cleavage,^{42,43} respectively.

The library was cycled through five rounds of selections following an established protocol⁴⁴ to enrich for phages displaying peptides that preferentially bound hGid4 (Figure 2(a)). Phages from individual clones that bound to GST-hGid4 (Δ 1-99) but not a control GST based on phage ELISA were subjected to DNA sequence analysis.

The screen yielded 41 unique sequences, none of which were overtly similar to the previously defined hGid4-binding consensus motif PGLWKS (Figure 2(B); Table S2). A new consensus emerged with the following preferences: (1) hydrophobic residues at position 1, with Phe predominating; (2) Asp at position 2; (3) hydrophobic residues at positions 3 and 6, and to a lesser extent at position 5; and (4) small and polar residues at positions 4 and 7. Unlike the PGLWKS sequence wherein the striking selectivity

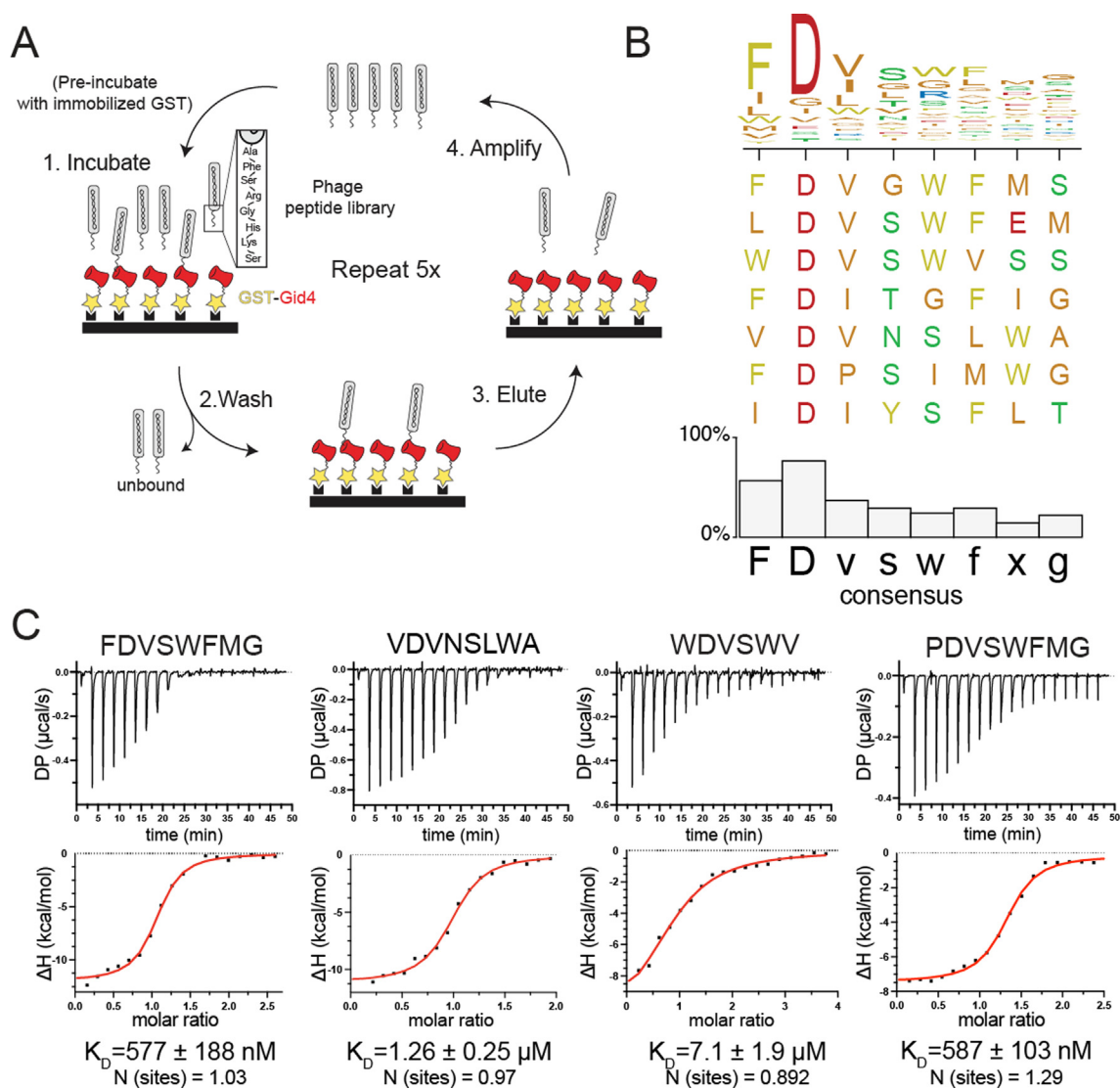


Figure 2. Identification of high-affinity hGid4-binding motifs initiating with non-Pro hydrophobic residues. **A.** Schematic of phage-display peptide library screen identifying peptides binding GST-tagged hGid4 ($\Delta 1-99$). **B.** Consensus motif obtained from multiple sequence alignment of 41 unique hGid4-binding peptide sequences listed in Table S2 (out of which a representative set of 7 sequences is shown). The height of the bars reflects the frequency of a given residue at different positions of the consensus. **C.** Isothermal titration calorimetry (ITC) to quantify binding of newly determined sequences to hGid4 ($\Delta 1-115$). The amount of heat released (ΔH) upon peptide injection was calculated from integrated raw ITC data (top) and plotted as a function of peptide:protein molar ratio (bottom). Dissociation constant (K_D) and the stoichiometry of the binding event (N) were determined by fitting to the One-Set-of-Sites binding model.

is predominantly for the first four residues, this new consensus extends through the seventh residue.

Although peptides with non-Pro hydrophobic N-termini were previously shown to bind hGid4, the tested sequences bound with one to two orders-of-magnitude lower affinity (K_D for IGLWKS 16 µM, VGLWKS 36 µM) than to PGLWKS ($K_D = 1.9$ µM) (Figure S2(A)).³⁹ To determine how the newly identified sequences compare, we quantified interactions by isothermal titration calorimetry (ITC). Notably, the peptides of sequences FDVSWFMG

and VDVNSLWA showed superior binding ($K_D = 0.6$ and 1.3 µM, respectively) to the best binder with an N-terminal Pro (Figure 2(C) and S1 (D)). Recognition of N-terminal Pro is also substantiated by the new consensus as substitution of Phe in FDVSWFMG with a Pro resulted in significantly tighter binding ($K_D = 0.6$ µM) than that of the PGLWKS motif (Figures 2(C) and S1(D)). Moreover, the affinity for a sequence starting with a Trp ($K_D = 7.1$ µM for WDVSWV) was superior to the previously identified best binder initiating with a non-Pro

hydrophobic residue (Figures 2(C) and S1(D)). Thus, hGid4 is able to accommodate even the bulkiest hydrophobic sidechain at the N-terminus of an interacting peptide. Taken together, the data show hGid4 binds a wide range of peptide sequences, with affinity strongly influenced by residues downstream of the N-terminus.

hGid4 structural pliability enables recognition of various N-terminal sequences

To understand how hGid4 recognizes diverse sequences, we determined its crystal structure bound to the FDVSWFMG peptide (Figure 3(A), Table S1; all peptide residues except C-terminal Gly visible in density). Overlaying this structure with published coordinates for other hGid4 complexes revealed diverse N-termini protruding into a common central substrate-binding tunnel (Figure S2(B), Phe (our study), or Pro, Leu, Val, or newly recognized Gly.^{10,39} The N-terminal residues are anchored through contacts of their amine groups with hGid4 Glu237 and Tyr258 at the tip of the substrate binding tunnel, and common hydrogen bonds of the peptide backbone carbonyl to hGid4 Gln132.

The structures suggest that the varying peptide sequences are accommodated by complementary conformations of four hairpin loops (L1-L4) at the edge of the hGid4 substrate-binding tunnel (Figure 3(B)). The L2, L3, and L4 loops are fully or partially invisible, and are presumably mobile, in the structure of apo-hGid4 assembled in a subcomplex with its interacting subunits from the CTLH E3.³⁸ However, they are ordered and adopt different conformations when bound to the different peptides.

As compared to the structure with PGLWKS, the interactions with FDVSWFMG are more extensive and relatively more dominated by hydrophobic contacts rather than hydrogen bonding, which rationalizes improved binding of the new motif (Figure 3(C)). The L2 and L3 loops are relatively further from the central axis of the hGid4 β -barrel to interact with more residues in the peptide sequence. The different position of the L2 loop is also required to accommodate the hydrophobic Phe in the context of the new sequence (Figure 3(D)). Meanwhile, repositioning of the L4 loop places hGid4 Gln282 to form a hydrogen bond with Asp2 in the peptide (Figure 3(C)). Moreover, upon binding to hGid4, FDVSWFMG itself adopts a structured conformation owing to multiple intrapeptide backbone hydrogen bonds as well as interaction of Asp2 sidechain with the sidechain and backbone amide of Ser4 (Figure 3(E)). Therefore, a strong bias towards Asp at position 2 of all identified sequences may stem from its importance for maintaining the complementary folds of both the peptide and the substrate binding pocket. Overall, the structures reveal pliability of the hGid4 substrate-binding tunnel enabling interactions with a range of N-terminal sequences,

which themselves may also contribute interactions by conformational complementarity.

Yeast GID substrate receptors recognize natural degrons with suboptimal affinity

To extend our findings to the yeast GID system, we screened the phage peptide library for binders to the yGid4 and yGid10 substrate receptors. The selected consensus sequence binding yGid4 paralleled that for hGid4 (Figure 4(A); Table S2), in agreement with their being true orthologs. Remarkably, despite high similarity to the Gid4s, and its only known endogenous substrate likewise initiating with a Pro,³⁶ the selections with yGid10 identified 12 unique sequences, some with bulky hydrophobic residues and others with Gly prevalent at position 1, each followed by a distinct downstream pattern (Figure 4(B); Table S3). By solving an X-ray structure of yGid10 bound to FWLPANLW peptide and superimposing it on its prior structure with N-terminus of its *bona fide* substrate Art2,³⁶ we confirmed that the novel sequence is accommodated by the previously characterized binding pocket of yGid10 (Figures 4(C) and S3(A); Table S1). Moreover, conformations of the yGid10 loops varied in complexes with different peptides,^{36,45} suggesting like hGid4, yGid10 structural pliability allows recognition of various N-terminal sequences (Figure S3(B)).

Then, we sought to quantitatively compare binding of the new sequences to respective substrate receptors. Affinities of yGid10 for Phe and Gly-initiating sequences, measured by ITC, were comparable to and 2-fold greater than for a peptide corresponding to the N-degron of a natural substrate Art2³⁶ (Figures 4(D) and S3(C)). Notably, the endogenous degron, and selected sequences, bind yGid10 10- to 20-fold more tightly than the Pro-initiating sequence previously identified by a yeast two-hybrid screen.³⁵ Although yGid4 is not amenable to biophysical characterization, we could rank-order peptides by inhibition of ubiquitylation of a natural GID^{SR4} substrate Mdh2 (Figure 4(E)). Comparing IC₅₀ values for the different peptides led to two major conclusions: (1) the phage display-selected sequences are better competitors than N-terminal sequences of endogenous gluconeogenic substrates, and (2) natural substrate N-terminal sequences themselves exhibit varying suppressive effects, with degron of Mdh2 being the most potent, followed by those of Fbp1 and Icl1.

To test if the novel sequences can mediate binding of substrates for ubiquitylation, we performed two experiments. First, we connected a yGid4- and a yGid10-binding sequence to a lysine via a flexible linker designed based on prior structural modelling.³⁸ The peptides also had a C-terminal fluorescein for detection. Incubating the peptides with either GID^{SR4} or GID^{SR10} and ubiquitylation assay mixes revealed that each serves as a substrate only for its cognate E3, with low activity

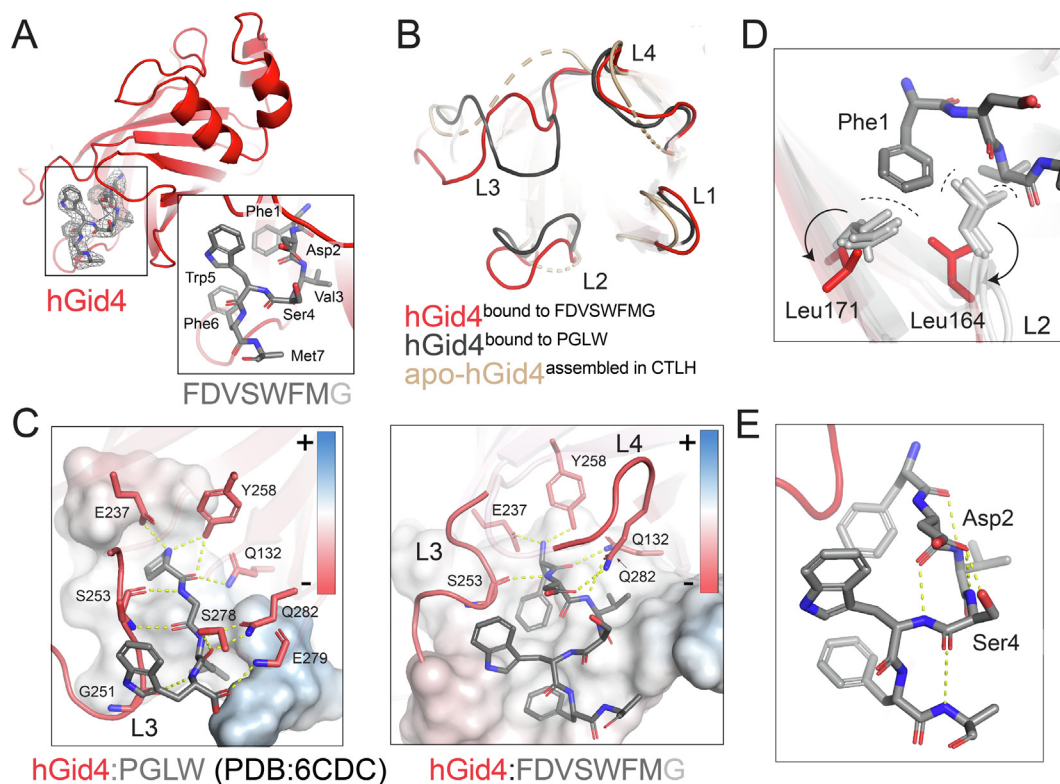


Figure 3. Molecular details of high-affinity peptide binding by hGid4. A. Crystal structure of hGid4 ($\Delta 1-120$, $\Delta 294-300$) bound to the FDVSWFMG peptide. Clear electron density ($2F_o - F_c$, contoured at 1.5σ ; grey mesh) was visible for all peptide residues besides the C-terminal Gly and the sidechain of Met7, presumably reflecting their mobility. B. Conformations of binding tunnel hairpin loops in apo-hGid4 assembled in CTLH^{SR4} (PDB ID: **7NSC**, light brown) as well as PGLW- (PDB ID: **6CDC**, dark grey) and FDVSWFMG-bound (red) hGid4. C. Comparison of PGLW (left) and FDVSWFMG (right) binding modes to hGid4. Hydrogen bonds between hGid4 residues (red sticks) and peptides (dark grey sticks) are depicted as yellow dashes, whereas the predominantly hydrophobic character of the binding tunnel is visualized as electrostatic potential surface (plotted at ± 7 kT/e; surface colored according to the potential: red – negative (-), blue – positive (+), white – uncharged). D. Overlay of hGid4 bound to PGLW (PDB ID: **6CDC**, light grey), IGLWKS (PDB ID: **6WZX**, light grey), VGLWKS (PDB ID: **6WZZ**, light grey) and FDVSWFMG (red) revealing conformational changes of L2 loop, which prevents steric clash (black dashes) between hGid4 Leu164 and Leu171 and N-terminal Phe of the FDVSWFMG peptide. E. Intra-peptide hydrogen bonding pattern (yellow dashes) within FDVSWFMG upon binding to hGid4.

of GID^{SR10} towards the yGid4-binding sequence (Figure 4(F)). Second, we replaced a native N-terminus of Fbp1 with the novel yGid4-binding consensus and performed *in vitro* ubiquitylation assay with two known forms of the GID E3 – the monomeric GID^{SR4} and the oligomeric Chelator-GID^{SR4} (Figure S4(A)). In both cases, the phage display-determined motif potentiated ubiquitylation of Fbp1 as compared to the WT control, indicating that it can mediate ubiquitylation of a full-length substrate.

Although ubiquitylation is typically a prerequisite, a multitude of processes control ubiquitin-mediated proteolysis in cells. Thus, we examined if the novel non-Pro initiating motifs would be sufficient to target Fbp1 for cellular degradation. We used the promoter reference technique, which was pioneered for examining degradation of GID E3 ligase substrates by normalizing for translation of

an exogenously expressed substrate (here, C-terminally 3xFLAG-tagged versions of Fbp1) relative to a simultaneously expressed control (here, DHFR).^{6,46} Since varying N-terminal sequences are differentially processed by Met-aminopeptidases,⁴⁷ or subjected to co-translational N-terminal acetylation⁴⁸ that would block binding to yGid4, we employed the previously-described technique of expressing assorted versions of Fbp1 as linear N-terminal fusions to ubiquitin. The N-terminal ubiquitin is cleaved off by deubiquitylating enzymes, revealing the residue following the ubiquitin sequence as a neo N-terminus.^{39,49} As shown previously, Fbp1 harboring the native degen, or that replaced by the sequence IGLW that binds yGid4 with 8-fold lower affinity promoted timely degradation in this assay.³⁹ However, neither of the novel tight binders, initiating with either Phe or Leu, con-

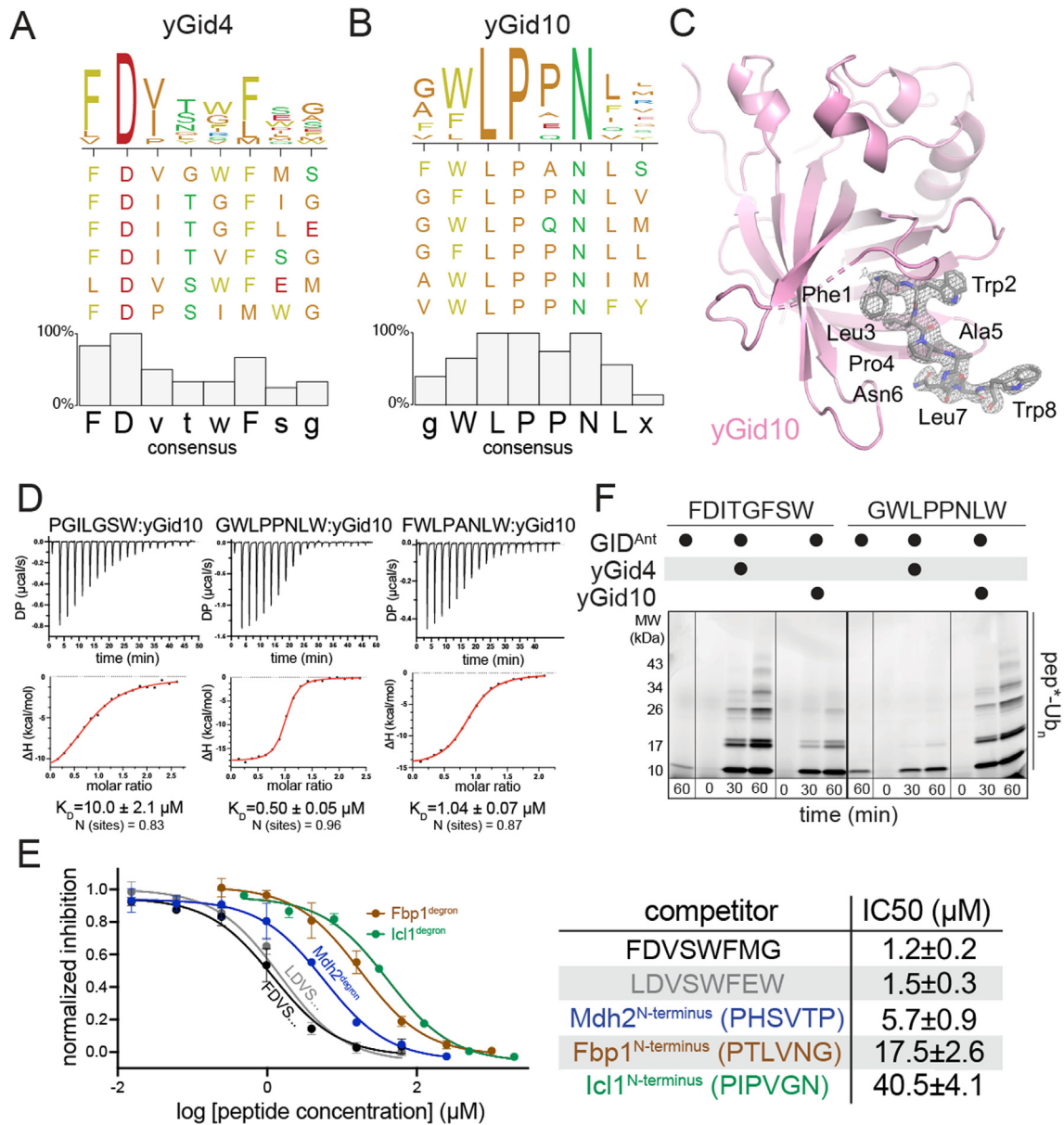


Figure 4. Identification of novel yGid4 and yGid10-binding sequence motifs superior to natural degrons. **A.** Consensus motif obtained by multiple sequence alignment of 12 unique yGid4-binding peptide sequences listed in Table S2 (out of which a representative set of 6 sequences is shown). **B.** Consensus motif obtained by multiple sequence alignment of 12 unique yGid10-binding peptide sequences listed in Table S3 (out of which a representative set of 6 sequences is shown). **C.** Crystal structure of yGid10 ($\Delta 1-64$, $\Delta 285-292$) (pink) bound to FWLPPNLW (grey sticks). The $2F_o - F_c$ electron density map corresponding to the peptide is shown as grey mesh contoured at 2σ . **D.** ITC binding assays as in Figure 2(C) but quantifying binding of several peptides to yGid10 ($\Delta 1-56$). **E.** Competitive *in vitro* ubiquitylation assays probing binding of two novel Phe- and Leu-initiating sequences to yGid4 ($\Delta 1-115$) as compared to N-termini of natural GID substrates (Mdh2, Fbp1 and Icl1). Unlabeled peptides were titrated to compete off binding of fluorescent Mdh2 (labeled with C-terminal fluorescein) to GID^{SR4}, thus attenuating its ubiquitylation. Normalized inhibition (fraction of ubiquitylated Mdh2 at varying concentration of unlabeled peptides divided by that in the absence of an inhibitor) was plotted against peptide concentration. Fitting to log[inhibitor] vs. response model yielded IC50 values and its standard error based on 2 independent measurements. **F.** Fluorescent scans of SDS-PAGE gels after *in vitro* ubiquitylation of fluorescent model peptides harboring either a yGid4 or yGid10-binding sequence by GID^{Ant} (comprising 2 copies each of Gid1 and Gid8, and one copy each of Gid5, Gid2 and Gid9) mixed with either yGid4 ($\Delta 1-115$) or yGid10 ($\Delta 1-56$) (forming GID^{SR4} or GID^{SR10}, respectively). The model peptides contained a corresponding phage display-determined consensus at the N-terminus connected to C-terminal fluorescein (indicated by an asterisk) with a flexible linker.

ferred instability (Figure S4(B)). At this point, future studies will be required to determine the molecular basis for defective proteasomal targeting. However, given that these sequences increased ubiquitylation *in vitro*, it is possible that accelerated ubiquitylation could impede degradation for example through mis-recruitment of deubiquitylating enzymes, mis-processing by Cdc48,⁵⁰ or more trivially, they may be subject to unknown modifications that inhibit binding to or ubiquitylation by the GID E3.

GID E3 supramolecular assembly differentially impacts catalytic efficiency toward different substrates

We were surprised by the differences in IC_{50} values for the naturally occurring degrons from the best-characterized GID E3 substrates, Fbp1 and Mdh2. We thus sought to compare ubiquitylation of the two substrates, which not only display different degrons but also distinct catalytic domains with unique constellations of lysines. Previous studies showed that ubiquitylation of both substrates depends on coordination of degron binding by yGid4 with placement of specific lysines in the ubiquitylation active site.^{34,38} However, while GID^{SR4} is competent for Mdh2 degradation *in vivo*, a distinct E3 assembly – wherein the Gid7 subunit drives two GID^{SR4} complexes into an oval arrangement (Chelator-GID^{SR4}) is specifically required for optimal ubiquitylation and degradation of Fbp1.³⁸ Two yGid4 subunits in Chelator-GID^{SR4} simultaneously bind degrons from the oligomeric Fbp1, for simultaneous ubiquitylation of specific lysines on multiple Fbp1 protomers.

Much like for Fbp1, addition of Gid7 to GID^{SR4} was shown to affect Mdh2 ubiquitylation *in vitro*, albeit in a more nuanced way.³⁸ As a qualitative test for avid binding to two degrons from Mdh2 (whose dimeric state was confirmed by SEC-MALS (Figure S5(A)) and homology modeling (Figure S5(B))) we performed competition assays with monovalent (GID^{SR4} alone or with addition of a truncated version of Gid7 that does not support supramolecular assembly) and bivalent (GID^{SR4} with Gid7 to form Chelator-GID^{SR4}) versions of the E3, and lysineless monodentate (Mdh2 degron peptide) and bidentate (Mdh2 dimer) inhibitors (Figure S5(C)). While the two inhibitors attenuated ubiquitylation of Mdh2 to a similar extent in reactions with the monovalent E3s, only the full-length Mdh2 complex substantially inhibited the bivalent Chelator-GID^{SR4}. This suggested that Chelator-GID^{SR4} is capable of avidly binding to Mdh2.

Thus, we quantified roles of the Fbp1 and Mdh2 degrons by measuring kinetic parameters upon titrating the two different GID E3 assemblies. In reactions with monovalent GID^{SR4}, the K_m for Mdh2 was roughly 3-fold lower than for Fbp1, in accordance with differences in degron binding (Figure 5(A) and (B)). Although the higher-order Chelator-GID^{SR4} assembly improved the K_m

values for Fbp1 and for Mdh2, the extents differ such that the values are similar for both substrates. Formation of the higher-order Chelator-GID^{SR4} assembly also dramatically increased the reaction turnover number (k_{cat}) for Fbp1, with a marginal increase for Mdh2 (8- vs. 1.4- times higher k_{cat} , respectively), which was already relatively high in the reaction with monomeric GID^{SR4} (Figures 5(C) and S4(C)). Combined with its effects on K_m , formation of the Chelator-GID^{SR4} assembly increased catalytic efficiency (k_{cat}/K_m) more than 100-times for Fbp1 and only 6-fold for Mdh2, which may rationalize Gid7-dependency of Fbp1 degradation.

Beyond avid substrate binding, the multipronged targeting of Fbp1 by Chelator-GID^{SR4} involves proper orientation of the substrate so that specific lysines in metabolic regulatory regions are simultaneously ubiquitylated.³⁸ To explain the lesser effect of Chelator-GID^{SR4} on catalytic efficiency toward Mdh2, we examined structural models. Briefly, after docking two substrate degrons into opposing yGid4 protomers, we rotated the tethered substrate to place the targeted lysines in the ubiquitylation active sites (Figure S5(E) and (F)). As shown previously, docking either Fbp1 targeted lysine cluster (K32/K35 and K280/K281) places the other in the opposing active site (Figures 5(D) and S5(E)). For Mdh2, upon mutating the individual clusters of preferentially targeted lysines determined previously,³⁴ we found that K330 is the major ubiquitylation target for Chelator-GID^{SR4} (Figure S5(D)). However, the structural locations of the two K330 residues within the Mdh2 dimer precludes their simultaneously engaging both Chelator-GID^{SR4} active sites (Figures 5(D) and S5(F)). Thus, the distinct constellations of targeted lysines may also contribute to differences in ubiquitylation efficiency.

Degron identity determines K_m for ubiquitylation but differentially impacts glucose-induced degradation of Mdh2 and Fbp1

To assess the roles of differential degron binding in the distinct contexts provided by the Fbp1 and Mdh2 experiments, we examined the effects of swapping their degrons. We first performed qualitative ubiquitylation assays using the simpler GID^{SR4} E3 ligase. Comparing ubiquitylation of fluorescently-labeled Fbp1 and Mdh2 side-by-side showed more Mdh2 is ubiquitylated with more ubiquitins during the time-course of reactions.³⁸ These properties are reversed when the N-terminal sequence of Mdh2 is substituted for the Fbp1 degron and vice-versa (Figure 6(A)).

Quantifying the K_m values showed that the values for degron-swapped substrates roughly scaled with degron identity (Figures 6(B) and S4(D)); for Mdh2 $K_m \approx 1.3 \mu\text{M}$, for degron-swapped Fbp1^{Mdh2 degron} $K_m \approx 0.8 \mu\text{M}$, for Fbp1 $K_m \approx 3.6 \mu\text{M}$, for degron-swapped Mdh2^{Fbp1 degron} $\approx 3.5 \mu\text{M}$). Furthermore,

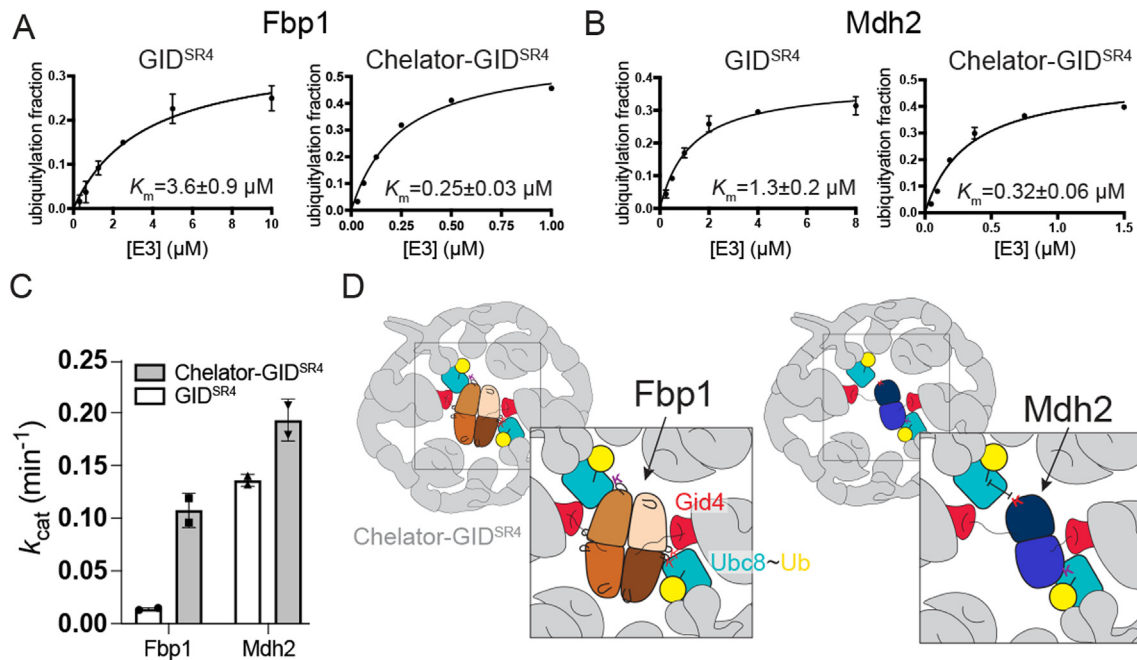


Figure 5. Differential targeting of Mdh2 and Fbp1 by GID E3. A. Plots showing fraction of *in vitro*-ubiquitylated Fbp1 as a function of varying concentration of GID E3 in either its monomeric GID^{SR4} or higher-order Chelator-GID^{SR4} form (co-expressed GID^{SR4} + Gid7). Fitting to Michaelis-Menten equation yielded K_m values. Error bars represent standard deviation ($n = 2$). B. Plots as in (A) but analyzing Mdh2 ubiquitylation. C. Comparison of k_{cat} values for Fbp1 and Mdh2 ubiquitin targeting by GID^{SR4} and Chelator-GID^{SR4} based on a time-course of substrate ubiquitylation (Figure S4(C)). D. Cartoons representing ubiquitylation of Fbp1 and Mdh2 by Chelator-GID^{SR4} based on structural modeling (Figure S5(E) and (F)).

as expected, the K_m values for all substrates improved in reactions with Chelator-GID^{SR4}. However, the relative impact seemed to scale with the way in which they are presented from the folded domain of a substrate rather than the degrons themselves (roughly 14-fold for Fbp1 and 11-fold for Fbp1^{Mdh2 degron} versus 4-fold for Mdh2 and 6-fold for Mdh2^{Fbp1 degron}).

Effects *in vivo* were examined by monitoring glucose-induced degradation of the wild-type and mutant substrates with the promoter-reference technique.^{6,46} As shown previously, Mdh2 was rapidly degraded in the wild-type yeast and the Δ Gid7 strain (Figure 6(C)).³⁸ However, turnover of the mutant version bearing the weaker Fbp1 degron was significantly slower in both genetic backgrounds. Thus, the Mdh2 degron is tailored to the Mdh2 substrate. In striking contrast, although the Mdh2 degron did subtly impact degradation of Fbp1, it was not sufficient to overcome dependency on Gid7 (Figure 6(D)). Thus, substrate ubiquitylation, and turnover, depend not only on degron identity, but also on their associated targeted domains.

Discussion

Overall, our study leads to several conclusions. First, GID/CTLH E3 substrate receptors recognize a diverse range of N-terminal sequences, dictated

not only by the N-terminal residue, but also the pattern of downstream amino acids (Figures 1 and S1). Second, such diverse N-terminal sequence recognition is achieved by the combination of (1) a deep substrate-binding tunnel culminating in conserved Glu and Tyr side-chains recognizing the N-terminal amine, (2) pliable loops at the entrance to the substrate binding tunnel that conform to a range of downstream sequences, and (3) the binders themselves forming distinct extended conformations that likewise complement the receptor structures (Figure 3). Remarkably, the hGid4 loops and the bound peptide reciprocally affect each other – peptide binding induces folding of the flexible loops whereas the arrangement of the loops dictates affinity for the bound peptide. This correlation rationalizes strong dependence of Gid4 specificity on the peptide sequence context. Third, the range of interactions result in a range of affinities (Figures 2, 4 and S2(A)). Notably, our randomized phage-display peptide library screen identified far tighter binders to yGid4 than known natural degrons. This approach also generated yGid10-binding sequences with affinities similar to or greater than the only known natural degron, and with significantly higher affinity than a sequence identified by yeast two-hybrid screening. Phage-display peptide library screening may thus prove to be a generally useful method for identifying E3

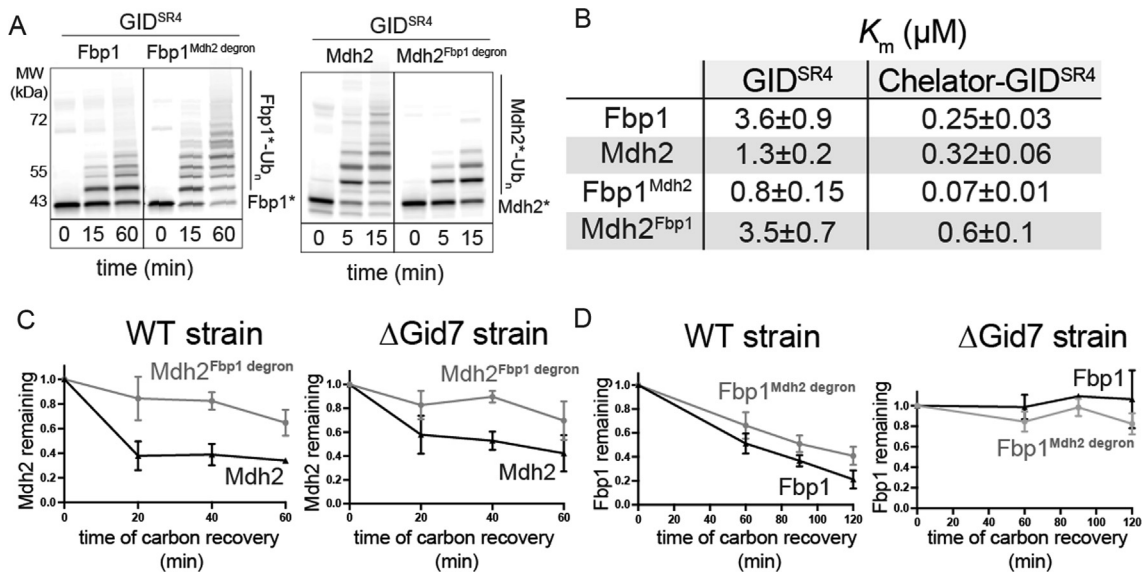


Figure 6. Combinatorial nature of substrate recognition by GID. A. Qualitative *in vitro* ubiquitylation assay probing effect of degnon exchange between Fbp1 and Mdh2. Both WT and degnon-swapped versions of Fbp1 and Mdh2 were C-terminally labelled with fluorescein (indicated by an asterisk) and ubiquitylated by GID^{SR4}. B. Table summarizing values of K_m for ubiquitylation of WT and degnon-swapped substrates by the two versions of GID based on the plots in Figure S4(D). C. *In vivo* glucose-induced degradation of exogenously expressed and C-terminally 3xFlag-tagged Mdh2 as well as its degnon-swapped versions quantified with a promoter-reference technique. Levels of the substrates (relative to the level of DHFR) at different timepoints after switch from gluconeogenic to glycolytic conditions were divided by their levels before the switch (timepoint 0). For each substrate, the experiment was performed in WT and Δ Gid7 yeast strains. Error bars represent standard deviation ($n = 3$), whereas points represent the mean. D. *In vivo* assay as in (C) but with WT and degnon-swapped Fbp1.

ligase binders. Fourth, degnon binding is only part of substrate recognition by GID E3s (Figures 5 and 6). Rather, ubiquitylation and degradation depend on both the pairing of a degnon with a substrate domain that presents lysines in a particular constellation, and configuration of the GID E3 in either a simplistic monovalent format or in a multivalent chelator assembly specialized for targeting some but not all oligomeric substrates.

Some features of the high-affinity peptide binding by Gid4s and yGid10 parallel other end-degnon E3s. Although ubiquitin ligases in the Ubr family employ UBR-box 1 and UBR-box 2 domains with a shallower modes of N-degnon recognition,^{51–57} C-degnon recognition by several cullin-RING ligase substrate receptors involves terminal peptide binding within deep clefts or tunnels^{58–61} much like the high-affinity binder interactions with Gid4s and yGid10. Furthermore, end-degnon E3 ligases use different strategies to recognize diverse degnon sequences. For example, a single Ubr-family E3 can bind different N-terminal sequences through distinct N-degnon-binding domains.^{62–64} However, much like Gid4s and yGid10 recognize diverse N-terminal sequences, the substrate-binding site of a single cullin-RING ligase was recently shown to bind interchangeably to a C-degnon or to a different substrate's internal sequence.^{60,61,65}

To-date, few GID E3 substrates have unambiguously been identified. Thus, our findings may have implications for identifying new substrates. Most of the currently characterized substrates depend on co-translational generation of an N-terminal Pro. However, sequences initiating with bulky hydrophobic residues may be refractory to N-terminal processing enzymes such as Met aminopeptidases.⁴⁷ Nonetheless, post-translational processing could generate such N-termini. Several paradigms for post-translational generation of N-degrons have been established by studies of Ubr1 substrates. First, endoproteolytic cleavage – by caspases, calpains, separases, cathepsins and mitochondrial proteases^{37,66–71} – is responsible for the generation of myriad Arg/N-degnon pathway substrates recognized by some Ubr-family E3s.⁹ Similarly, N-terminal trimming by aminopeptidases has recently been reported to expose Pro/N-degrons of two yGid4 substrates.⁷² Notably, 15 hGid4 interactors reported in the BioGRID database⁷³ have a solvent-exposed internal [FIL]-D-[VIL] sequence (Figure S6), raising the possibility that the newly identified Gid4- and yGid10-binding motifs likewise could be exposed upon post-translational proteolytic cleavage. Second, some N-degrons are created by aminoacyl-tRNA protein transferases-catalyzed appendage of an

additional amino acid at the protein's N-terminus.^{64,74} The bacterial N-degron pathway involves conjugation of hydrophobic residues such as Phe and Leu,^{75,76} hence it is tempting to speculate that hydrophobic N-degrons in eukaryotes could likewise involve such N-terminal amino acid addition. Finally, yeast Ubr1 is modulated in an intricate manner: after HtrA-type protease cleavage, a portion of the protein Roq1 binds Ubr1 and alters its substrate specificity.⁷⁷ Notably, proteomic studies showed that the human CTLH complex itself associates with the HtrA-type protease HTRA2,^{22,24,78–80} known to be involved in mitochondrial quality control.^{81,82} This raises the tantalizing possibility that the CTLH E3 might form a multienzyme targeting complex that integrates a regulatory cascade to generate its own substrates or regulatory partners.

The identified sequences might also play various non-degradative functions. Some tight binders to other E3 ligases are pseudosubstrates that modulate subcellular localization,^{83,84} or inhibit activity.^{85–87} Irrespective of whether such sequences target endogenous proteins to GID/CTLH-family E3 ligases, the identification of nanomolar hGid4 binders and the structural insight into the substrate receptor plasticity may be useful for development of small molecules targeting these E3s.

Finally, our examination of degron-swapped GID E3 substrates Fbp1 and Mdh2 showed that

N-terminal sequence is only part of the equation determining ubiquitylation and subsequent degradation. Mdh2 required its own degron and its ubiquitylation and degradation were impaired when substituted with the weaker degron from Fbp1, irrespective of capacity for GID^{SR4} to undergo Gid7-mediated superassembly. However, while either degron could support Fbp1 targeting, this requires Gid7-dependent formation of the chelate-like E3 configuration. Taken together, our data reveal that structural malleability of both the substrate receptor and the E3 supramolecular assembly endows GID E3 complexes – and presumably CTLH E3s as well – capacity to conform to diverse substrates, with varying degrons and associated targeted domains. Such structural malleability raises potential for regulation through modifications or interactions impacting the potential conformations of both the substrate binding domains and higher-order assemblies, and portends future studies will reveal how these features underlie biological functions of GID/CTLH E3s across eukaryotes. Moreover, our results highlight that turnover depends on structural complementarity between E3 and both the substrate degron and ubiquitylated domains, a principle of emerging importance for therapeutic development of targeted protein degradation.

Methods

Reagent table

Reagent/Resource	Reference or Source	Identifier or Catalog Number
Experimental models, cell lines and strains		
High Five Insect cells	Thermo Fisher	Cat#B85502
<i>Saccharomyces cerevisiae</i> : Strain S288C: BY4741; MATa his3Δ1leu2Δ0 met15Δ0 ura3Δ0	Euroscarf	Cat#Y00000
CRLY12; BY4741, Gid4::KANMX	38	N/A
CRLY14; BY4741, Gid7::KANMX	38	N/A
Recombinant DNA		
pCSJ95	6	N/A
pCSJ125	6	N/A
DSJC3; pRS313-pGPD-MPHSVTP-Fbp1(Δ1-7)-3xFLAG-CY C-pGPD-DHFR-HA-CYC	This study	N/A
DSJC4; pRS313-pGPD-MPTLVNG-Mdh2(Δ1-7)-3xFLAG-CY C-pGPD-DHFR-HA-CYC	This study	N/A
DSJC5; pRS313-pGPD-Ub-FDITGFSW-Fbp1(Δ1-9)-3xFLAG-CYC-pGPD-DHFR-HA-CYC	This study	N/A
DSJC6; pRS313-pGPD-Ub-LDVSWFEW-Fbp1(Δ1-9)-3xFLAG-CYC-pGPD-DHFR-HA-CYC	This study	N/A
DSJC7; pRS313-pGPD-Ub-IGLW-Fbp1(Δ1-5)-3xFLAG-CYC-pGPD-DHFR-HA-CYC	39	N/A
pLIB Gid4	34	N/A
pLIB Gid7	38	N/A
pBIG2 Gid1:Gid8-TEV-2xS:Gid5:Gid2:Gid9:Gid7	38	N/A
pBIG2 Gid1:Gid8-TEV-2xS:Gid5:Gid4:Gid2:Gid9:	38	N/A

(continued)

Reagent/Resource	Reference or Source	Identifier or Catalog Number
Gid7		
pBIG2 Gid1:Gid8-TEV-2xS:Gid5:Gid4:Gid2:Gid9	34	N/A
pBIG2 Gid1:Gid8-TEV-2xS:Gid5:Gid2:Gid9	34	N/A
pGEX GST-TEV-hGid4 (Δ1-115)	This study	N/A
pGEX GST-TEV-Gid7	38	N/A
pGEX GST-TEV-Gid7 (Δ1-285)	38	N/A
pGEX GST-TEV-hGid4 (Δ1-99)	38	N/A
pGEX GST-TEV-hGid4 (Δ1-120, Δ294-300)	This study	N/A
pGEX GST-TEV-yGid4 (Δ1-115)	34	N/A
pGEX GST-TEV-yGid10 (Δ1-57)	34	N/A
pGEX GST-TEV-yGid10 (Δ1-64, Δ285-292)	This study	N/A
pRSF Fbp1-GGGGS-sortag-6xHis	38	N/A
pRSF Mdh2-GGGGS-LPETGG-6xHis	34	N/A
pRSF MPHSVTP-Fbp1 (Δ1-7)-GGGGS-LPETGG-6xHis	This study	N/A
pRSF MPTLVNG-Mdh2 (Δ1-7)-GGGGS-sortag-6xHis	This study	N/A
pRSF GST-TEV-SUMO- FDITGFSW-Fbp1(Δ1-9)-GGGGS-so rtag-6xHis	This study	N/A
pRSF Ubc8-6xHis	34	N/A
pRSF 6xHis-hGid4 (Δ1-115)	This study	N/A
pET3b Ub (ubiquitin)	34	N/A
pET29 sortase A	89	N/A
pRSF Mdh2-6xHis	34	N/A
pRSF Mdh2-6xHis K254R/K256R/K259R	This study	N/A
pRSF Mdh2-6xHis K330R	This study	N/A
pRSF Mdh2-6xHis K360R/K361R	This study	N/A
pRSF Mdh2-6xHis K254R/K256R/K259R; K330R; K360R/ K361R	34	N/A
Antibodies		
Mouse anti-His	Cell Signaling Technology	Cat#9991
Sheep polyclonal anti-hGid4	38	N/A
Monoclonal ANTI-FLAG M2	Sigma Aldrich	Cat#F1804
Rabbit anti-HA	Sigma Aldrich	Cat#H6908
Goat anti-rabbit IgG Dylight488 conjugated	Invitrogen	Cat#35552
Goat anti-mouse IgG Dylight633 conjugated	Invitrogen	Cat#35512
Goat anti-mouse IgG HRP conjugated	Sigma Aldrich	Cat#A4416; PRID
Chemicals, Enzymes and peptides		
complete EDTA free	Roche	Cat#05056489001
Aprotinin from bovine lung	Sigma	A1153-10MG
Leupeptin	Sigma	L2884-250MG
Benzamidine	Sigma	B6506-25G
GGGGGFYVK-FAM	MPIB	N/A
PGLWKS	MPIB	N/A
IGLWKS	MPIB	N/A
Leu-Gly	Sigma	CAS# 686–50-0
Pro-Gly	Sigma	CAS# 2578–57-6
Ala-Gly	MPIB	CAS# 687–69-4
Gly-Gly	MPIB	CAS# 556–50-3
GVATSLW	MPIB	N/A
FDVSWFMG	MPIB	N/A
PDVSWFMG	MPIB	N/A
LDVSWFMG	MPIB	N/A
VDVNSLWA	MPIB	N/A
WDVSWV	MPIB	N/A
FDITGFS	MPIB	N/A

(continued on next page)

(continued)

Reagent/Resource	Reference or Source	Identifier or Catalog Number
GWLPPNLW	MPIB	N/A
PGILGSW	MPIB	N/A
FWLPANLW	MPIB	N/A
PHSVTPWSI	MPIB	N/A
PTLVNGWPR	MPIB	N/A
PIPVGNWTK	MPIB	N/A
VWEVKTNQ	MPIB	N/A
PHSVTPSIEQDSLK	MPIB	N/A
PGLWKS-FAM	MPIB	N/A
GGGGRHDS(P)GLDS(P)MKDEE-FAM	MPIB	N/A
FDITGFSWRDSTEGFTGRGWSGRGWSKGGK-FAM	MPIB	N/A
GWLPPNLWRDSTEGFTGRGWSGRGWSKGGK-FAM	MPIB	N/A
Software		
Phyre ²	90	http://www.sbg.bio.ic.ac.uk/~phyre2/html/page.cgi?id=index
UCSF Chimera	91	https://www.cgl.ucsf.edu/chimera/
UCSF ChimeraX	92	https://www.rbvi.ucsf.edu/chimerax/
PyMOL v2.1	Schrödinger	https://pymol.org/2/
Coot	93,94	https://www2.mrc-lmb.cam.ac.uk/personal/pemsley/coot/
Phenix	95–97	https://www.phenix-online.org/
Image Studio	LI-COR Biosciences	https://www.licor.com/bio/image-studio/
Fiji/ImageJ	98	https://imagej.net/
GraphPad Prism version 8.0	GraphPad Software	www.graphpad.com
ImageQuant TL Toolbox version 8.2	GE Healthcare	
MicroCal PEAQ-ITC Analysis Software	Malvern Panalytical	

Plasmid preparation and mutagenesis

All the genes encoding yeast GID subunits including the substrate receptors yGid4 and yGid10, as well as Fbp1 and Mdh2 substrates were amplified from *S. cerevisiae* BY4741 genomic DNA. The gene encoding hGid4 was codon-optimized for bacterial expression system and synthesized by GeneArt (Thermo Fisher Scientific).

All the recombinant constructs used for protein expression were generated by Gibson assembly method⁹⁹ and verified by DNA sequencing. The GID subunits were combined using the biGBac method¹⁰⁰ into a single baculoviral expression vector. All the plasmids used in this study are listed in the Reagent table.

Bacterial protein expression and purification

All bacterial expressions were carried out in *E. coli* BL21 (DE3) RIL cells in a Terrific Broth medium¹⁰¹ overnight at 18 °C. All versions of yGid4, yGid10 and hGid4 (except for that used for NMR) were expressed as GST-TEV fusions. The harvested cell pellets were resuspended in the lysis buffer (50 mM HEPES pH 7.5, 200 mM NaCl, 5 mM DTT and 1 mM PMSF), disintegrated by sonication and subjected to

glutathione affinity chromatography, followed by overnight cleavage of the eluted proteins at 4 °C with tobacco etch virus⁸⁷ protease to release the GST tag. Final purification was performed with size exclusion chromatography (SEC) in the final buffer containing 50 mM HEPES pH 7.5, 200 mM NaCl and 1 mM or 5 mM DTT (for assays and crystal trials, respectively), or 0.5 mM TCEP (for ITC binding assay). Additionally, pass-back over glutathione affinity resin was performed in order to get rid of the remaining uncleaved GST-fusion protein and free GST.

All versions of Ubc8, Fbp1 (except for FDITGFSW-Fbp1) and Mdh2 were expressed with a C-terminal 6xHis tag. The harvested cell pellets were resuspended in the lysis buffer (50 mM HEPES pH 7.5, 200 mM NaCl, 5 mM β-mercaptoethanol, 10 mM imidazole and 1 mM PMSF) and sonicated. Proteins were purified by nickel affinity chromatography, followed by anion exchange and SEC in the final buffer containing 50 mM HEPES pH 7.5, 200 mM NaCl and 1 mM DTT.

To purify FDITGFSW-Fbp1 for fluorescein labeling, it was expressed as N-terminal GST-SUMO fusion. After glutathione affinity chromatography, the GST-SUMO tag was cleaved

off with a SUMO-specific protease SENP2 generating a desired N-terminus. After cleavage, FDTGFSW-Fbp1 was further purified by SEC in the final buffer containing 50 mM HEPES pH 7.5, 200 mM NaCl and 1 mM DTT. The uncleaved GST-SUMO fusion and free GST-SUMO was removed by pass-back over the GST resin.

Untagged WT ubiquitin used for *in vitro* assays was purified via glacial acetic acid method,¹⁰² followed by gravity S column ion exchange chromatography and SEC.

Insect cell protein expression and purification

All yeast GID complexes used in this study were expressed in insect cells. For protein expression, Hi5 insect cells were transfected with recombinant baculovirus variants and grown for 60–72 h in EX-CELL 420 Serum-Free Medium at 27 °C. The insect cells were harvested by centrifugation at 450xg for 15 min and pellets were resuspended in a lysis buffer (50 mM HEPES pH 7.5, 200 mM NaCl, 5 mM DTT, 10 µg/ml leupeptin, 20 µg/ml aprotinin, 2 mM benzamidine, EDTA-free complete protease inhibitor tablet (Roche, 1 tablet per 50 ml of buffer) and 1 mM PMSF). All the complexes were purified from insect cell lysates by StrepTactin affinity chromatography by pulling on a twin-Strep tag fused to the Gid8 C-terminus. Further purification was performed by anion exchange chromatography and SEC in the final buffer containing 25 mM HEPES pH 7.5, 200 mM NaCl and 1 mM DTT.

Preparation of fluorescent substrates for *in vitro* activity assays

C-terminal labelling of Fbp1, Mdh2 and their degron-swapped versions with fluorescein was performed through a sortase A-mediated reaction. The reaction mix contained 50 µM substrate (C-terminally tagged with a sortag (LPETGG) followed by a 6xHis tag), 250 µM fluorescent peptide (GGGGGFYVK-FAM), 50 µM sortase A⁸⁹ and a reaction buffer (50 mM Tris pH 8, 150 mM NaCl and 10 mM CaCl₂). The reaction was carried out at room temperature for 30 min. After the reaction, a pass-back over Ni-NTA resin was done to get rid of unreacted substrates. Further purification was done with SEC in the final buffer containing 50 mM HEPES pH 7.5, 200 mM NaCl and 1 mM DTT.

¹⁵N labelling of hGid4

For NMR experiments, ¹⁵N-labeling of 6xHis-hGid4 (Δ1-115) was carried out. Firstly, 50 ml of the preculture was spun at 3000 rpm for 20 mins. The supernatant was then removed and resuspended with 1x M9 cell growth medium (2 g glucose, 5 mg/ml thiamine chloride, 1 M MgSO₄, 1 M CaCl₂ and 1g ¹⁵NH₄Cl per liter of 1x M9 medium) containing all essential ions and

antibiotics. The cultures were then grown at 37 °C and 200 rpm until it reached the OD₆₀₀ of 0.5–0.8. Subsequently, the temperature was reduced to 23 °C and kept for an hour before inducing with 0.6 M IPTG. The cultures were then kept growing overnight at 23 °C, 200 rpm, harvested and used for protein purification as described in the section “Protein expression and purification” but in the final SEC buffer containing 25 mM phosphate buffer pH 7.8, 150 mM NaCl and 1 mM DTT.

NMR (Nuclear Magnetic Resonance) spectroscopy

NMR experiments were recorded at 298 K on Bruker Avance III 600 MHz spectrometer (at ¹H Larmor frequency of 600 MHz) equipped with a 5 mm TCI cryoprobe. Samples at 0.1 mM ¹⁵N-labeled hGid4 were prepared in NMR buffer (50 mM HEPES, 100 mM NaCl, pH 7.0) supplemented with 10% D₂O. ¹H,¹⁵N HSQC (heteronuclear single quantum coherence) correlation spectra were acquired with 2048 × 256 complex points and a recycle delay of 1.2 s, with 24 scans. DMSO references were acquired at the beginning and end of the assay. No differences were observed between them. Spectra in the presence of ligands were measured at 1 mM Pro or Pro-Gly and 0.5 mM PGLWKS peptide.

Phage-displayed N-terminal peptide library construction and selections

A diverse octapeptide N-terminal phage-displayed library was generated for the identification of peptides binding to hGid4 (Δ1-99), yGid4 (Δ1-115) and yGid10 (Δ1-56). An IPTG-inducible P_{tac} promoter was utilized to drive the expression of open-reading frames encoding the fusion proteins in the following form: the still secretion signal sequence, followed by a random octapeptide peptide, a GGGSGGG linker and the M13 bacteriophage gene-8 major coat protein (P8). The libraries were constructed by using oligonucleotide-directed mutagenesis with the phagemid pRSTOP4 as the template, as described.¹⁰³ The mutagenic oligonucleotides used for library construction were synthesized using with NNK degenerate codons (where N = A/C/G/T & K = G/T) that encode all 20 genetically encoded amino acids. The diversity of the library was 3.5 × 10⁹ unique peptides.

The N-terminal peptide library was cycled through five rounds of binding selections against immobilized GST-tagged hGid4, yGid4, and yGid10, as described.⁴⁴ Pre-incubation of the phage pools against immobilized GST was performed before each round of selections to deplete non-specific binding peptides. For rounds four and five, 48 individual clones were isolated and tested for binding to the corresponding targets by phage ELISA,¹⁰⁴ and clones with a strong and specific pos-

itive ELISA signal were Sanger sequenced. A total of 41, 12, and 12 unique peptide sequences were identified binding to hGid4, yGid4, and yGid10, respectively, and their sequences were aligned to identify common specificity motifs.

Oligonucleotide used for the Kunkel reaction to construct the library:

GCTACAAATGCCTATGCANNKNNKNNKNNKN
NKNNKNNKNNKGGTGGAGGATCCGGAGGA.

Fluorescence polarization (FP) assays

To determine conditions for a competitive FP assay, we first performed the experiment in a non-competitive format. A 2-fold dilution series of hGid4 (Δ 1-115) was prepared in the FP buffer containing 25 mM Hepes pH 7.5, 150 mM NaCl, 0.5 mM DTT and 20 nM fluorescent PGLWKS-FAM and a non-binding GGGGRHDS(P)GLDS(P)MKDEE-FAM as a control peptide. The mixed samples were equilibrated at room temperature for 5 min before transferring to Greiner 384-well flat bottom black plates. Then, the polarization values were measured at the excitation and emission wavelengths of 482 nm and 530 nm, respectively using CLARIOstar microplate reader (BMG LABTECH). For each run, the gain was recorded with FP buffer-only control. The data were fit to one site-binding model in GraphPad Prism to determine K_D value.

To compare binding of several unlabeled ligands to hGid4, we performed the FP measurements in a competitive format. Based on the FP plot from hGid4 titration experiment, we identified hGid4 concentration, which resulted in ~60% saturation of the FP signal. Next, 2-fold dilution series of unlabeled competitors was prepared in the FP buffer mixed with 6.8 μ M hGid4. After 5 min incubation, the measurement was performed as described above. The data were plotted relative to the FP signal in the absence of an inhibitor as a function of log(ligand concentration) and analyzed with log(inhibitor) vs. response model to determine IC50 values. To determine relative inhibitory strength of the ligands, the determined IC50 values were divided by that of PGLWKS.

Screening of PGLWKS sequence for hGid4 binding using peptide spot array

The array of peptides derived from the PGLWKS sequence with all 20 amino acid substituted at positions 1, 2 and 3 together, 4 and 5 were synthesized on a membrane in the MPIB biochemistry core facility. The membrane blot was first blocked with 3% milk in TBST buffer (20 mM Tris, 150 mM NaCl and 0.1% Tween 20) for 1 h at room temperature. hGid4 (Δ 1-99) was diluted to 10 μ g/ml in the buffer containing 150 mM NaCl, 25 mM HEPES pH 7.5, 0.5 mM EDTA pH 8.0, 10% glycerol, 0.1% Tween 20, 2% milk and 1 mM DTT and incubated with the blocked membrane

overnight at 4 °C with gentle shaking. The membrane was then washed with TBST buffer 3 times, incubated with primary anti-hGid4 sheep polyclonal antibody (1:500) for 3 h with gentle shaking, followed by multiple washing steps with TBST and 1 h incubation with secondary HRP-conjugated anti-sheep (1:5000) antibody. The membranes were again washed multiple times with TBST and hGid4 binding was visualized by chemiluminescence in Amersham Imager 800 (Cytiva).

Isothermal titration calorimetry (ITC) binding assays

To quantify binding of peptides to hGid4 (Δ 1-115) and yGid10 (Δ 1-56), we employed ITC. All peptides were dissolved in the SEC buffer used for purification of substrate receptors containing 25 mM HEPES pH 7.5, 150 mM NaCl and 0.5 mM TCEP and their concentration was measured by absorbance at 280 nm (if not present in the original sequence, a single tryptophan residue was appended at peptides' C-termini to facilitate determination of peptide concentration). Binding experiments were carried out in the MicroCal PEAQ-ITC instrument (Malvern Pananalytica) at 25 °C by titrating peptides to either hGid4 or yGid10. Peptides were added to individual substrate receptors using 19 \times 2 μ l injections, with 4 s injection time and 150 s equilibration time between the injections. The reference power was set to 10 μ cal/s. The concentration of the peptides and substrate receptors were customized according the estimated K_D values. Raw ITC data were analyzed using One-Set-of-Sites binding model (Malvern Pananalytica) to determine K_D and stoichiometry of the binding events (N). All plots presented in figures were prepared in GraphPad Prism.

Size exclusion chromatography with multiangle light scattering (SEC-MALS)

To determine the oligomeric state of Mdh2, we performed SEC-MALS (conducted in the MPIB Biochemistry Core Facility). For each run, 100 μ l Mdh2 at 1 mg/mL were injected onto Superdex 200 column equilibrated with a buffer containing 25 mM HEPES pH 7.5, 150 mM NaCl and 5 mM DTT.

In vitro activity assays

All ubiquitylation reactions were performed in a multi-turnover format in the buffer containing 25 mM HEPES pH 7.5, 150 mM NaCl, 5 mM ATP and 10 mM MgCl₂. To quench the reactions at indicated timepoints, an aliquot of the reaction mix was mixed with SDS-PAGE loading buffer. Ubiquitylation of fluorescein-labelled substrates was visualized with a fluorescent scan of an SDS-

PAGE gel with a Typhoon imager (GE Healthcare) and quantified with ImageQuant (GE Healthcare; version 8.2).

To verify whether FDITGFSW and GWLPPNLW can be recognized by, respectively, yGid4 and yGid10 during ubiquitylation reaction (Figure 4(D)), we performed an *in vitro* activity assay with model peptides, consisting of the respective N-terminal sequences connected to a single acceptor lysine with a 23-residue linker and C-terminal fluorescein (the length of the linker was optimized based on the GID^{SR4} structure³⁸). To start the reaction, 0.2 μM E1 Uba1, 1 μM E2 Ubc8-6xHis, 0.5 μM E3 GID^{Ant}, 20 μM ubiquitin, 1 μM yGid4 (Δ1-115) or yGid10 (Δ1-56) and 1 μM peptide substrate were mixed and incubated at room temperature.

In order to probe avid binding of Mdh2 to Chelator-GID^{SR4}, we employed a competition ubiquitylation assay (Figure S4(C)). The reactions were initiated by mixing 0.2 μM Uba1, 1 μM Ubc8-6xHis, 0.5 μM E3 GID^{SR4}, 0 or 2 μM Gid7 (WT or its N terminal deletion mutant, Δ1-284), 0.5 μM Mdh2-FAM, 20 μM unlabeled competitor (dimeric Mdh2-6xHis or a peptide comprising Mdh2 N-terminal sequence PHSVTSPSEQDSLK) and 20 μM ubiquitin. GID^{SR4} was incubated with Gid7 for 5 min on ice before the start of the reaction.

To test which of the preferred ubiquitylation sites within Mdh2 determined previously for GID^{SR434} are major ubiquitylation targets of Chelator-GID^{SR4}, we performed an activity assay with WT and mutant Mdh2, in which putative target lysine clusters (K254/K256/K259; K330; K360/K361) were mutated to arginines individually and all together (Figure S5(A)). To start the reaction, 0.2 μM Uba1, 1 μM Ubc8-6xHis, 0.1 μM Chelator-GID^{SR4}, 1 μM WT or mutant Mdh2-6xHis and 20 μM ubiquitin were mixed. After quenching, Mdh2-6xHis and its ubiquitylated versions were visualized by immunoblotting with anti-6xHis primary antibody and HRP-conjugated anti-mouse secondary antibody.

To quantitatively compare recognition of phage display-identified sequences and degrons of natural GID substrates by yGid4, we employed competitive ubiquitylation assays (Figure 4(F)). Unlabeled peptide inhibitors comprising the analyzed sequences were titrated to compete off binding of Mdh2-FAM to GID^{SR4}, thus attenuating its ubiquitylation. Reactions were started by addition of 20 μM ubiquitin to the mixture of 0.2 μM E1 Uba1, 1 μM E2 Ubc8-6xHis, 0.5 μM E3 GID^{Ant}, 1 μM yGid4 (Δ1-115), 0.25 μM Mdh2-FAM and various concentrations of peptide competitors. After 3 min, the reactions were quenched so that their velocities were still in the linear range. The fractions of ubiquitylated Mdh2 in the presence of an inhibitor were divided by that for Mdh2 alone and plotted against peptide concentration. Fitting of the data to [inhibitor] vs. response model in GraphPad Prism yielded IC50 values.

To qualitatively compare degrons of Fbp1 and Mdh2 in the context of full-length substrates (Figure 6(A)), we performed activity assay with WT and degron-swapped versions (Fbp1^{Mdh2 degron} and Mdh2^{Fbp1 degron}) of the substrates by mixing 0.2 μM E1 Uba1, 1 μM E2 Ubc8-6xHis, 1 μM E3 GID^{Ant}, 2 μM yGid4 (Δ1-115), 0.5 μM WT or mutant version of Fbp1-FAM or Mdh2-FAM and 20 μM ubiquitin. Similarly, we tested if the N-terminal FDITGFSW motif can promote *in vitro* ubiquitylation of Fbp1. The reactions contained 0.2 μM E1 Uba1, 1 μM E2 Ubc8-6xHis, 0.1 μM GID^{SR4} or Chelator-GID^{SR4}, 1 μM of WT or mutant Fbp1 and 20 μM ubiquitin.

Kinetic parameters for ubiquitylation of WT and degron-swapped versions of Fbp1 and Mdh2 were determined as described previously.³⁸ Briefly, to determine Michaelis-Menten constant (K_m), we titrated E3 (GID^{SR4} or Chelator-GID^{SR4}) at constant substrate concentration kept below K_m (0.5 and 0.1 μM for reactions with GID^{SR4} and Chelator-GID^{SR4}, respectively; Figures 5(A), (B) and S4(E)). The reaction time was optimized so that the velocity of all reactions was in the linear range. The fraction of ubiquitylated substrate was calculated and plotted as a function of E3 concentration in GraphPad Prism and fit to Michaelis-Menten equation to determine K_m . To calculate k_{cat} , time course assays were performed with the ratios of [E3]: K_m and [substrate]: K_m kept the same for all substrates and E3 versions (2.7 and 0.4, respectively; Figure 5(C)). The rates of the reactions were calculated by linear regression in GraphPad Prism from plots of fraction of ubiquitylated substrates vs. reaction time (Figure S4(D)) and converted into initial velocity using the following equation: $V_0 = rate \cdot [substrate]$.

Then, V_{max} was estimated using a modified form of the Michaelis-Menten equation:

$$V_{max} = \frac{V_0 \cdot (K_m + [substrate])}{[substrate]}$$

To obtain k_{cat} values, V_{max} was divided by the E3 concentration: $k_{cat} = \frac{V_{max}}{[E3]}$.

Yeast strain construction and growth conditions

The yeast strains used in this study are specified in the Reagents table. All the yeast strains were constructed as derivatives of BY4741 using standard genetic techniques and were verified using PCR, DNA sequencing and immunoblotting to confirm protein expression.

In vivo yeast substrate degradation assays

In order to test the effect of degron identity on glucose-induced degradation of GID substrates, we monitored turnover of WT and degron-exchanged versions of Mdh2 and Fbp1, using the promoter reference technique.⁴⁶ Initially, WT and ΔGid7 yeast strains were transformed with a plasmid harboring the open reading frame of either Fbp1-3xFLAG, Mdh2-3xFLAG or their mutant versions (Fbp1^{Mdh2 degron}-3xFLAG and Mdh2^{Fbp1 degron}-3xFLAG) and the control protein DHFR-3xHA, both

expressed from identical promoters. Cells were then grown in SD-glucose medium to OD⁶⁰⁰ of 1.0 followed by carbon starvation in SE medium (0.17% yeast nitrogen base, 0.5% ammonium sulfate, 2% ethanol, amino acid mix) for 19 h. Next, yeasts at the equivalent of 1 OD₆₀₀ were transferred to SD-glucose medium containing 0.5 mM tetracycline resulting in translation inhibition induced by its binding to specific RNA-aptamers within ORFs of the examined and control proteins. At the indicated time points, 1 mL of cells were harvested and pellets were flash frozen in liquid nitrogen. Cell lysis was performed by thawing and resuspending the pellets in 800 μ L 0.2 M NaOH, followed by 20 min incubation on ice and subsequent centrifugation at 11,200xg for 1 min at 4 °C. The supernatant was removed and pellets were resuspended in 50 μ L HU buffer (8 M Urea, 5% SDS, 1 mM EDTA, 100 mM DTT, 200 mM Tris pH 6.8, protease inhibitor, bromophenol blue), heated at 70 °C for 10 min and then centrifuged again for 5 min at 11,200xg and at 4 °C. The substrates and the control protein DHFR were visualized by immunoblotting with, respectively, anti-FLAG or anti-HA primary and DyLight fluorophore conjugated secondary antibodies, and imaged using a Typhoon scanner (GE Healthcare). Quantification was done using the ImageStudioLite software (LI-COR). For the final graphs, the substrate signal was first normalized relative to the DHFR signal and then to the time point zero (before glucose replenishment). Three biological replicates were performed for all the assays.

A similar experiment was done to test if the novel high-affinity yGid4-binding sequences can confer glucose-induced instability onto Fbp1. To enable N-terminal exposure of sequences with N-terminal bulky hydrophobic residues, all Fbp1 versions (FDITGFSW-Fbp1(Δ 1-9)-3xFLAG, LDVSWFEW-Fbp1(Δ 1-9)-3xFLAG, a positive control IGLW-Fbp1(Δ 1-5)-3xFLAG³⁹ and Fbp1-3xFLAG) were expressed as N-terminal fusions to ubiquitin as described previously.^{39,49} The cleavage of the ubiquitin fusion was confirmed by immunoblotting with anti-FLAG antibodies. The experiment was performed as described above.

X-ray crystallography

All crystallization trials were carried out in the MPIB Crystallization facility. All crystals were obtained by vapor diffusion experiment in sitting drops at room temperature. The diffraction datasets were recorded at X10SA beam line, Swiss Light Source (SLS) in Villigen, Switzerland.

Crystals of hGid4 (Δ 1-99) (without a peptide) were obtained at a concentration of 10 mg/ml using 18% PEG 3350, 0.2 M ammonium nitrate and 0.1 M Bis-Tris buffer at pH 7. Crystals were cryoprotected in 20% ethylene glycol and flash-frozen in liquid nitrogen for data collection.

For hGid4 (Δ 1-120, Δ 294-300) crystals containing FDVSWFM peptide, 9.2 mg/mL of hGid4 was mixed

with 600 μ M FDVSWFM peptide and incubated for 1 h on ice before setting up trays. Crystals were obtained using 1.1 M Sodium malonate, 0.3% Jeffamine ED-2001 pH 7 and 0.1 M HEPES pH 7 and cryoprotected using mix of 20% glycerol and 20% ethylene glycol.

Similarly, for yGid10 (Δ 1-64, Δ 285-292) crystals with the peptide FWLPANLW, the protein was concentrated to 10 mg/mL and mixed with the peptide to obtain final protein and peptide concentrations of 262 μ M and 760 μ M, respectively (\sim 3-fold molar excess of the peptide). Crystals were obtained using 0.1 M MES pH 6.9 and cryoprotected using 20% ethylene glycol.

All the diffraction data were indexed, integrated, and scaled using XDS package. Phasing was performed through molecular replacement using the previous structure of hGid4 (PDB ID: **6CDC**, in the case of hGid4 with and without a peptide) or cryo EM structure of yGid4 (extracted from PDB ID: **7NS3**, in the case of peptide-bound yGid10) using PHASER module integrated into PHENIX software suite.^{95–97} Model building was done using Coot,^{93,94} and further refinements were carried out with phenix.refine. Details of X-ray diffraction data collection and refinement statistics are listed in [Table S1](#).

Data availability

The accession codes for the PDB models are available in RCSB as follows: human Gid4 bound to a Gly/N-peptide, PDB ID: **7Q4Y**; human Gid4 bound to a Phe/N-peptide, PDB ID: **7Q50**; yeast Gid10 bound to a Phe/N-peptide, PDB ID: **7Q51**.

All the unprocessed image data have been deposited to Mendeley Data: <http://dx.doi.org/10.17632/nz5mch8k2w.1>.

CRedit authorship contribution statement

Jakub Chrustowicz: Conceptualization, Methodology, Investigation, Resources. **Dawafuti Sherpa:** Conceptualization, Methodology, Investigation, Resources. **Joan Teyra:** Methodology, Investigation, Resources. **Mun Siong Loke:** Investigation, Resources. **Grzegorz M. Popowicz:** Methodology, Investigation. **Jerome Basquin:** Methodology, Investigation. **Michael Sattler:** Methodology, Supervision, Funding acquisition. **J. Rajan Prabu:** Methodology. **Sachdev S. Sidhu:** Conceptualization, Methodology, Investigation, Supervision, Funding acquisition. **Brenda A. Schulman:** Conceptualization, Methodology, Supervision, Funding acquisition.

Acknowledgments

We thank G. Chen and A. Pavlenco for construction of N-terminal peptide phage-displayed

library; A. Varshavsky for promoter reference plasmids; S. Uebel and S. Pettera for peptide synthesis; K. Valer-Saldana and S. Pleyer for assistance with protein crystallization; J. Rech for the preparation of peptide spot arrays; Paul Scherrer Institut, Villigen, Switzerland for provision of synchrotron radiation beamtime at beamlines PXII and X10SA of the SLS; G. Kleiger for guidance regarding kinetics; I. Paron for technical assistance with mass spectrometry; O. Karayel and T. Vu for bioinformatic analysis of hGid4 interactors; S.v. Gronau for maintenance of insect cells and the Schulman lab for advice and support.

The project was funded by the Deutsche Forschungsgemeinschaft (DFG) SFB1035 (B.A.S. and M.S.), and Leibniz Prize SCHU 3196/1 (B.A. S.). Work in the Schulman lab is supported by the Max Planck Society.

Declaration of Competing Interest

B.A.S. is an honorary professor at Technical University of Munich, Germany and adjunct faculty at St. Jude Children's Research Hospital, Memphis, TN, USA, is on the scientific advisory boards of Interline Therapeutics and BioTheryX, and is co-inventor of intellectual property related to DCN1 small molecule inhibitors licensed to Cinsano.

Appendix A. Supplementary data

Supplementary data to this article can be found online at <https://doi.org/10.1016/j.jmb.2021.167347>.

Received 31 August 2021;

Accepted 2 November 2021;

Available online 9 November 2021

Keywords:

N-degron pathway;

Phage display;

Ubiquitin;

Protein–protein interaction;

Structural biology

† These authors contributed equally.

References

- Varshavsky, A., (2019). N-degron and C-degron pathways of protein degradation. *Proc. Natl. Acad. Sci. USA* **116**, 358–366.
- Bachmair, A., Varshavsky, A., (1989). The degradation signal in a short-lived protein. *Cell* **56**, 1019–1032.
- Bachmair, A., Finley, D., Varshavsky, A., (1986). In vivo half-life of a protein is a function of its amino-terminal residue. *Science* **234**, 179–186.
- Tasaki, T., Mulder, L.C., Iwamatsu, A., Lee, M.J., Davydov, I.V., Varshavsky, A., et al., (2005). A family of mammalian E3 ubiquitin ligases that contain the UBR box motif and recognize N-degrons. *Mol. Cell Biol.* **25**, 7120–7136.
- Tasaki, T., Kwon, Y.T., (2007). The mammalian N-end rule pathway: new insights into its components and physiological roles. *Trends Biochem. Sci.* **32**, 520–528.
- Chen, S.J., Wu, X., Wadas, B., Oh, J.H., Varshavsky, A., (2017). An N-end rule pathway that recognizes proline and destroys gluconeogenic enzymes. *Science* **355**.
- Hammerle, M., Bauer, J., Rose, M., Szallies, A., Thumm, M., Dusterhus, S., et al., (1998). Proteins of newly isolated mutants and the amino-terminal proline are essential for ubiquitin-proteasome-catalyzed catabolite degradation of fructose-1,6-bisphosphatase of *Saccharomyces cerevisiae*. *J. Biol. Chem.* **273**, 25000–25005.
- Timms, R.T., Zhang, Z., Rhee, D.Y., Harper, J.W., Koren, I., Elledge, S.J., (2019). A glycine-specific N-degron pathway mediates the quality control of protein N-myristoylation. *Science* **365**.
- Varshavsky, A., (2011). The N-end rule pathway and regulation by proteolysis. *Protein Sci.* **20**, 1298–1345.
- Dong, C., Zhang, H., Li, L., Tempel, W., Lopnau, P., Min, J., (2018). Molecular basis of GID4-mediated recognition of degrons for the Pro/N-end rule pathway. *Nature Chem. Biol.* **14**, 466–473.
- Yan, X., Li, Y., Wang, G., Zhou, Z., Song, G., Feng, Q., et al., (2021). Molecular basis for recognition of Gly/N-degrons by CRL2(ZYG11B) and CRL2(ZER1). *Mol. Cell*.
- Driessen, H.P., de Jong, W.W., Tesser, G.I., Bloemendal, H., (1985). The mechanism of N-terminal acetylation of proteins. *CRC Crit. Rev. Biochem.* **18**, 281–325.
- Hwang, C.S., Shemorry, A., Varshavsky, A., (2010). N-terminal acetylation of cellular proteins creates specific degradation signals. *Science* **327**, 973–977.
- Polevoda, B., Arnesen, T., Sherman, F., (2009). A synopsis of eukaryotic N-alpha-terminal acetyltransferases: nomenclature, subunits and substrates. *BMC Proc.* **3** (Suppl 6), S2.
- Shemorry, A., Hwang, C.S., Varshavsky, A., (2013). Control of protein quality and stoichiometries by N-terminal acetylation and the N-end rule pathway. *Mol. Cell* **50**, 540–551.
- Wolf, D.H., (2004). From lysosome to proteasome: the power of yeast in the dissection of proteinase function in cellular regulation and waste disposal. *Cell Mol. Life Sci.* **61**, 1601–1614.
- Santt, O., Pfirrmann, T., Braun, B., Juretschke, J., Kimmig, P., Scheel, H., et al., (2008). The yeast GID complex, a novel ubiquitin ligase (E3) involved in the regulation of carbohydrate metabolism. *Mol. Biol. Cell.* **19**, 3323–3333.
- Braun, B., Pfirrmann, T., Menssen, R., Hofmann, K., Scheel, H., Wolf, D.H., (2011). Gid9, a second RING finger protein contributes to the ubiquitin ligase activity of the Gid complex required for catabolite degradation. *FEBS Letters* **585**, 3856–3861.
- Menssen, R., Schweiggert, J., Schreiner, J., Kusevic, D., Reuther, J., Braun, B., et al., (2012). Exploring the topology of the Gid complex, the E3 ubiquitin ligase involved in catabolite-induced degradation of gluconeogenic enzymes. *J. Biol. Chem.* **287**, 25602–25614.
- Regelmann, J., Schule, T., Josupeit, F.S., Horak, J., Rose, M., Entian, K.D., et al., (2003). Catabolite degradation of fructose-1,6-bisphosphatase in the yeast *Saccharomyces cerevisiae*: a genome-wide screen identifies eight novel GID genes and indicates the existence of two degradation pathways. *Mol. Biol. Cell.* **14**, 1652–1663.

21. Kobayashi, N., Yang, J., Ueda, A., Suzuki, T., Tomaru, K., Takeno, M., et al., (2007). RanBPM, Muskelin, p48EMLP, p44CTLH, and the armadillo-repeat proteins ARMC8alpha and ARMC8beta are components of the CTLH complex. *Gene* **396**, 236–247.
22. Boldt, K., van Reeuwijk, J., Lu, Q., Koutroumpas, K., Nguyen, T.M., Texier, Y., et al., (2016). An organelle-specific protein landscape identifies novel diseases and molecular mechanisms. *Nature Commun.* **7**, 11491.
23. Cao, W.X., Kabelitz, S., Gupta, M., Yeung, E., Lin, S., Rammelt, C., et al., (2020). Precise Temporal Regulation of Post-transcriptional Repressors Is Required for an Orderly Drosophila Maternal-to-Zygotic Transition. *Cell Rep.* **31**, 107783
24. Lampert, F., Stafa, D., Goga, A., Soste, M.V., Gilberto, S., Olieric, N., et al., (2018). The multi-subunit GID/CTLH E3 ubiquitin ligase promotes cell proliferation and targets the transcription factor Hbp1 for degradation. *Elife* **7**
25. Liu, H., Ding, J., Kohnlein, K., Urban, N., Ori, A., Villavicencio-Lorini, P., et al., (2020). The GID ubiquitin ligase complex is a regulator of AMPK activity and organismal lifespan. *Autophagy* **16**, 1618–1634.
26. Liu, H., Pfirrmann, T., (2019). The Gid-complex: an emerging player in the ubiquitin ligase league. *Biol. Chem.* **400**, 1429–1441.
27. Zavortink, M., Rutt, L.N., Dzitoyeva, S., Henriksen, J.C., Barrington, C., Bilodeau, D.Y., et al., (2020). The E2 Marie Kondo and the CTLH E3 ligase clear deposited RNA binding proteins during the maternal-to-zygotic transition. *Elife* **9**
28. Soni, S., Bala, S., Gwynn, B., Sahr, K.E., Peters, L.L., Hanspal, M., (2006). Absence of erythroblast macrophage protein (Emp) leads to failure of erythroblast nuclear extrusion. *J. Biol. Chem.* **281**, 20181–20189.
29. Zhen, R., Moo, C., Zhao, Z., Chen, M., Feng, H., Zheng, X., et al., (2020). Wdr26 regulates nuclear condensation in developing erythroblasts. *Blood* **135**, 208–219.
30. Pfirrmann, T., Villavicencio-Lorini, P., Subudhi, A.K., Menssen, R., Wolf, D.H., Hollemann, T., (2015). RMND5 from *Xenopus laevis* is an E3 ubiquitin-ligase and functions in early embryonic forebrain development. *PLoS One* **10**, e0120342
31. Maitland, M.E.R., Kuljanin, M., Wang, X., Lajoie, G.A., Schild-Poulter, C., (2021). Proteomic analysis of ubiquitination substrates reveals a CTLH E3 ligase complex-dependent regulation of glycolysis. *FASEB J.* **35**, e21825
32. Yuan, S., Zhu, H., Gou, H., Fu, W., Liu, L., Chen, T., et al., (2012). A ubiquitin ligase of symbiosis receptor kinase involved in nodule organogenesis. *Plant Physiol.* **160**, 106–117.
33. Menssen, R., Bui, K., Wolf, D.H., (2018). Regulation of the Gid ubiquitin ligase recognition subunit Gid4. *FEBS Letters* **592**, 3286–3294.
34. Qiao, S., Langlois, C.R., Chrustowicz, J., Sherpa, D., Karayel, O., Hansen, F.M., et al., (2020). Interconversion between Anticipatory and Active GID E3 Ubiquitin Ligase Conformations via Metabolically Driven Substrate Receptor Assembly. *Mol. Cell* **77** 150–63 e9.
35. Melnykov, A., Chen, S.J., Varshavsky, A., (2019). Gid10 as an alternative N-recognin of the Pro/N-degron pathway. *Proc. Natl. Acad. Sci. USA* **116**, 15914–15923.
36. Langlois CR, Beier V, Karayel O, Chrustowicz J, Sherpa D, Mann M, et al. A GID E3 ligase assembly ubiquitinates an Rsp5 E3 adaptor and regulates plasma membrane transporters. bioRxiv [Preprint].
37. Kong, K.E., Fischer, B., Meurer, M., Kats, I., Li, Z., Ruhle, F., et al., (2021). Timer-based proteomic profiling of the ubiquitin-proteasome system reveals a substrate receptor of the GID ubiquitin ligase. *Mol. Cell* **81** 2460–76 e11.
38. Sherpa, D., Chrustowicz, J., Qiao, S., Langlois, C.R., Hehl, L.A., Gottemukkala, K.V., et al., (2021). GID E3 ligase supramolecular chelate assembly configures multipronged ubiquitin targeting of an oligomeric metabolic enzyme. *Mol. Cell* **81** 2445–59 e13.
39. Dong, C., Chen, S.J., Melnykov, A., Weirich, S., Sun, K., Jeltsch, A., et al., (2020). Recognition of nonproline N-terminal residues by the Pro/N-degron pathway. *Proc. Natl. Acad. Sci. USA* **117**, 14158–14167.
40. Peters, E.A., Schatz, P.J., Johnson, S.S., Dower, W.J., (1994). Membrane insertion defects caused by positive charges in the early mature region of protein pIII of filamentous phage fd can be corrected by priA suppressors. *J. Bacteriol.* **176**, 4296–4305.
41. Rodi, D.J., Soares, A.S., Makowski, L., (2002). Quantitative assessment of peptide sequence diversity in M13 combinatorial peptide phage display libraries. *J. Mol. Biol.* **322**, 1039–1052.
42. Nilsson, I., von Heijne, G., (1992). A signal peptide with a proline next to the cleavage site inhibits leader peptidase when present in a sec-independent protein. *FEBS Letters* **299**, 243–246.
43. Pluckthun, A., Knowles, J.R., (1987). The consequences of stepwise deletions from the signal-processing site of beta-lactamase. *J. Biol. Chem.* **262**, 3951–3957.
44. Tonikian, R., Zhang, Y., Boone, C., Sidhu, S.S., (2007). Identifying specificity profiles for peptide recognition modules from phage-displayed peptide libraries. *Nature Protoc.* **2**, 1368–1386.
45. Shin, J.S., Park, S.H., Kim, L., Heo, J., Song, H.K., (2021). Crystal structure of yeast Gid10 in complex with Pro/N-degron. *Biochem. Biophys. Res. Commun.* **582**, 86–92.
46. Oh, J.H., Chen, S.J., Varshavsky, A., (2017). A reference-based protein degradation assay without global translation inhibitors. *J. Biol. Chem.* **292**, 21457–21465.
47. Sherman, F., Stewart, J.W., Tsunasawa, S., (1985). Methionine or not methionine at the beginning of a protein. *Bioessays* **3**, 27–31.
48. Aksnes, H., Drazic, A., Marie, M., Arnesen, T., (2016). First Things First: Vital Protein Marks by N-Terminal Acetyltransferases. *Trends Biochem. Sci.* **41**, 746–760.
49. Varshavsky, A., (2005). Ubiquitin fusion technique and related methods. *Methods Enzymol.* **399**, 777–799.
50. Barbin, L., Eisele, F., Santt, O., Wolf, D.H., (2010). The Cdc48-Ufd1-Npl4 complex is central in ubiquitin-proteasome triggered catabolite degradation of fructose-1,6-bisphosphatase. *Biochem. Biophys. Res. Commun.* **394**, 335–341.
51. Choi, W.S., Jeong, B.C., Joo, Y.J., Lee, M.R., Kim, J., Eck, M.J., et al., (2010). Structural basis for the recognition of N-end rule substrates by the UBR box of ubiquitin ligases. *Nature Struct. Mol. Biol.* **17**, 1175–1181.
52. Kim, L., Heo, J., Kwon, D.H., Shin, J.S., Jang, S.H., Park, Z.Y., et al., (2021). Structural basis for the N-degron specificity of CipS1 from *Arabidopsis thaliana*. *Protein Sci.* **30**, 700–708.
53. Matta-Camacho, E., Kozlov, G., Li, F.F., Gehring, K., (2010). Structural basis of substrate recognition and

- specificity in the N-end rule pathway. *Nature Struct. Mol. Biol.* **17**, 1182–1187.
54. Pan, M., Zheng, Q., Wang, T., Liang, L., Mao, J., Zuo, C., et al. (2021). Structural Insights Into the Initiation and Elongation of Ubiquitination by Ubr1. *BioRxiv [Preprint]*.
55. Roman-Hernandez, G., Grant, R.A., Sauer, R.T., Baker, T. A., (2009). Molecular basis of substrate selection by the N-end rule adaptor protein ClpS. *Proc. Natl. Acad. Sci. USA* **106**, 8888–8893.
56. Schuenemann, V.J., Kralik, S.M., Albrecht, R., Spall, S.K., Truscott, K.N., Dougan, D.A., et al., (2009). Structural basis of N-end rule substrate recognition in *Escherichia coli* by the ClpAP adaptor protein ClpS. *EMBO Rep.* **10**, 508–514.
57. Wang, K.H., Roman-Hernandez, G., Grant, R.A., Sauer, R.T., Baker, T.A., (2008). The molecular basis of N-end rule recognition. *Mol. Cell* **32**, 406–414.
58. Li, Y., Jin, K., Bunker, E., Zhang, X., Luo, X., Liu, X., et al., (2018). Structural basis of the phosphorylation-independent recognition of cyclin D1 by the SCF (FBXO31) ubiquitin ligase. *Proc. Natl. Acad. Sci. USA* **115**, 319–324.
59. Rusnac, D.V., Lin, H.C., Canzani, D., Tien, K.X., Hinds, T. R., Tsue, A.F., et al., (2018). Recognition of the Diglycine C-End Degron by CRL2(KLHDC2) Ubiquitin Ligase. *Mol. Cell.* **72** 813–22 e4.
60. Chen, X., Liao, S., Makaros, Y., Guo, Q., Zhu, Z., Krizelman, R., et al., (2021). Molecular basis for arginine C-terminal degron recognition by Cul2(FEM1) E3 ligase. *Nature Chem. Biol.* **17**, 254–262.
61. Zhao, S., Ru, W., Chen, X., Liao, S., Zhu, Z., Zhang, J., et al., (2021). Structural insights into SMCR8 C-degron recognition by FEM1B. *Biochem. Biophys. Res. Commun.* **557**, 236–239.
62. Sriram, S.M., Kwon, Y.T., (2010). The molecular principles of N-end rule recognition. *Nature Struct. Mol. Biol.* **17**, 1164–1165.
63. Tasaki, T., Zakrzewska, A., Dudgeon, D.D., Jiang, Y., Lazo, J.S., Kwon, Y.T., (2009). The substrate recognition domains of the N-end rule pathway. *J. Biol. Chem.* **284**, 1884–1895.
64. Tasaki, T., Sriram, S.M., Park, K.S., Kwon, Y.T., (2012). The N-end rule pathway. *Annu. Rev. Biochem.* **81**, 261–289.
65. Manford, A.G., Rodriguez-Perez, F., Shih, K.Y., Shi, Z., Berdan, C.A., Choe, M., et al., (2020). A cellular mechanism to detect and alleviate reductive stress. *Cell* **183** 46–61 e21.
66. Piatkov, K.I., Colnaghi, L., Bekes, M., Varshavsky, A., Huang, T.T., (2012). The auto-generated fragment of the Usp1 deubiquitylase is a physiological substrate of the N-end rule pathway. *Mol. Cell* **48**, 926–933.
67. Rao, H., Uhlmann, F., Nasmyth, K., Varshavsky, A., (2001). Degradation of a cohesin subunit by the N-end rule pathway is essential for chromosome stability. *Nature* **410**, 955–959.
68. Ditzel, M., Wilson, R., Tenev, T., Zachariou, A., Paul, A., Deas, E., et al., (2003). Degradation of DIAP1 by the N-end rule pathway is essential for regulating apoptosis. *Nature Cell Biol.* **5**, 467–473.
69. Piatkov, K.I., Oh, J.H., Liu, Y., Varshavsky, A., (2014). Calpain-generated natural protein fragments as short-lived substrates of the N-end rule pathway. *Proc. Natl. Acad. Sci. USA* **111**, E817–E826.
70. Jin, S.M., Lazarou, M., Wang, C., Kane, L.A., Narendra, D. P., Youle, R.J., (2010). Mitochondrial membrane potential regulates PINK1 import and proteolytic destabilization by PARL. *J. Cell Biol.* **191**, 933–942.
71. Yamano, K., Youle, R.J., (2013). PINK1 is degraded through the N-end rule pathway. *Autophagy* **9**, 1758–1769.
72. Chen, S.J., Kim, L., Song, H.K., Varshavsky, A., (2021). Aminopeptidases trim Xaa-Pro proteins, initiating their degradation by the Pro/N-degron pathway. *Proc. Natl. Acad. Sci. USA* **118**.
73. Oughtred, R., Rust, J., Chang, C., Breitkreutz, B.J., Stark, C., Willems, A., et al., (2021). The BioGRID database: A comprehensive biomedical resource of curated protein, genetic, and chemical interactions. *Protein Sci.* **30**, 187–200.
74. Gonda, D.K., Bachmair, A., Wunning, I., Tobias, J.W., Lane, W.S., Varshavsky, A., (1989). Universality and structure of the N-end rule. *J. Biol. Chem.* **264**, 16700–16712.
75. Tobias, J.W., Shrader, T.E., Rocap, G., Varshavsky, A., (1991). The N-end rule in bacteria. *Science* **254**, 1374–1377.
76. Dougan, D.A., Truscott, K.N., Zeth, K., (2010). The bacterial N-end rule pathway: expect the unexpected. *Mol. Microbiol.* **76**, 545–558.
77. Szoradi, T., Schaeff, K., Garcia-Rivera, E.M., Itzhak, D.N., Schmidt, R.M., Bircham, P.W., et al., (2018). SHRED Is a Regulatory Cascade that Reprograms Ubr1 Substrate Specificity for Enhanced Protein Quality Control during Stress. *Mol. Cell.* **70** 1025–37 e5.
78. Botham, A., Coyaud, E., Nirmalanandhan, V.S., Gronda, M., Hurren, R., Maclean, N., et al., (2019). Global Interactome Mapping of Mitochondrial Intermembrane Space Proteases Identifies a Novel Function for HTRA2. *Proteomics* **19**, e1900139
79. Huttlin, E.L., Ting, L., Bruckner, R.J., Gebreab, F., Gygi, M.P., Szpyt, J., et al., (2015). The BioPlex Network: A Systematic Exploration of the Human Interactome. *Cell* **162**, 425–440.
80. Huttlin, E.L., Bruckner, R.J., Paulo, J.A., Cannon, J.R., Ting, L., Baltier, K., et al., (2017). Architecture of the human interactome defines protein communities and disease networks. *Nature* **545**, 505–509.
81. Clausen, T., Kaiser, M., Huber, R., Ehrmann, M., (2011). HTRA proteases: regulated proteolysis in protein quality control. *Nature Rev. Mol. Cell Biol.* **12**, 152–162.
82. Vande Walle, L., Lamkanfi, M., Vandenabeele, P., (2008). The mitochondrial serine protease HtrA2/Omi: an overview. *Cell Death Differ.* **15**, 453–460.
83. Davis, M., Hatzubai, A., Andersen, J.S., Ben-Shushan, E., Fisher, G.Z., Yaron, A., et al., (2002). Pseudosubstrate regulation of the SCF(beta-TrCP) ubiquitin ligase by hnRNP-U. *Genes Dev.* **16**, 439–451.
84. Welcker, M., Larimore, E.A., Frappier, L., Clurman, B.E., (2011). Nucleolar targeting of the fbw7 ubiquitin ligase by a pseudosubstrate and glycogen synthase kinase 3. *Mol. Cell Biol.* **31**, 1214–1224.
85. Cappell, S.D., Mark, K.G., Garbett, D., Pack, L.R., Rape, M., Meyer, T., (2018). EMI1 switches from being a substrate to an inhibitor of APC/C(CDH1) to start the cell cycle. *Nature* **558**, 313–317.
86. Manford, A.G., Mena, E.L., Shih, K.Y., Gee, C.L., McMinimy, R., Martinez-Gonzalez, B., et al., (2021).

- Structural basis and regulation of the reductive stress response. *Cell* **184** 5375–90 e16.
87. Miller, J.J., Summers, M.K., Hansen, D.V., Nachury, M.V., Lehman, N.L., Loktev, A., et al., (2006). Emi1 stably binds and inhibits the anaphase-promoting complex/cyclosome as a pseudosubstrate inhibitor. *Genes Dev.* **20**, 2410–2420.
 88. Mohamed, W.I., Park, S.L., Rabl, J., Leitner, A., Boehringer, D., Peter, M., (2021). The human GID complex engages two independent modules for substrate recruitment. *EMBO Rep.*
 89. Chen, I., Dorr, B.M., Liu, D.R., (2011). A general strategy for the evolution of bond-forming enzymes using yeast display. *Proc. Natl. Acad. Sci. USA* **108**, 11399–11404.
 90. Kelley, L.A., Mezulis, S., Yates, C.M., Wass, M.N., Sternberg, M.J., (2015). The Phyre2 web portal for protein modeling, prediction and analysis. *Nat Protoc.* **10**, 845–858.
 91. Pettersen, E.F., Goddard, T.D., Huang, C.C., Couch, G.S., Greenblatt, D.M., Meng, E.C., et al., (2004). UCSF Chimera—a visualization system for exploratory research and analysis. *J. Comput. Chem.* **25**, 1605–1612.
 92. Goddard, T.D., Huang, C.C., Meng, E.C., Pettersen, E.F., Couch, G.S., Morris, J.H., et al., (2018). UCSF ChimeraX: Meeting modern challenges in visualization and analysis. *Protein Sci.* **27**, 14–25.
 93. Emsley, P., Cowtan, K., (2004). Coot: model-building tools for molecular graphics. *Acta Crystallogr. D Biol. Crystallogr.* **60**, 2126–2132.
 94. Emsley, P., Lohkamp, B., Scott, W.G., Cowtan, K., (2010). Features and development of Coot. *Acta Crystallogr. D Biol. Crystallogr.* **66**, 486–501.
 95. Adams, P.D., Afonine, P.V., Bunkoczi, G., Chen, V.B., Davis, I.W., Echols, N., et al., (2010). PHENIX: a comprehensive Python-based system for macromolecular structure solution. *Acta Crystallogr. D Biol. Crystallogr.* **66**, 213–221.
 96. Afonine, P.V., Klaholz, B.P., Moriarty, N.W., Poon, B.K., Sobolev, O.V., Terwilliger, T.C., et al., (2018). New tools for the analysis and validation of cryo-EM maps and atomic models. *Acta Crystallogr. D Struct. Biol.* **74**, 814–840.
 97. DiMaio, F., Echols, N., Headd, J.J., Terwilliger, T.C., Adams, P.D., Baker, D., (2013). Improved low-resolution crystallographic refinement with Phenix and Rosetta. *Nature Methods* **10**, 1102–1104.
 98. Schindelin, J., Arganda-Carreras, I., Frise, E., Kaynig, V., Longair, M., Pietzsch, T., et al., (2012). Fiji: an open-source platform for biological-image analysis. *Nature Methods* **9**, 676–682.
 99. Gibson, D.G., Young, L., Chuang, R.Y., Venter, J.C., Hutchison 3rd, C.A., Smith, H.O., (2009). Enzymatic assembly of DNA molecules up to several hundred kilobases. *Nature Methods* **6**, 343–345.
 100. Weissmann, F., Petzold, G., VanderLinden, R., Huis In't Veld, P.J., Brown, N.G., Lampert, F., et al., (2016). biGBac enables rapid gene assembly for the expression of large multisubunit protein complexes. *Proc. Natl. Acad. Sci. USA* **113**, E2564–9.
 101. Lobanov, M.Y., Furlitova, E.I., Bogatyreva, N.S., Roytberg, M.A., Galzitskaya, O.V., (2010). Library of disordered patterns in 3D protein structures. *PLoS Comput. Biol.* **6**, e1000958
 102. Kaiser, S.E., Riley, B.E., Shaler, T.A., Trevino, R.S., Becker, C.H., Schulman, H., et al., (2011). Protein standard absolute quantification (PSAQ) method for the measurement of cellular ubiquitin pools. *Nature Methods* **8**, 691.
 103. Chen, G., Gorelik, L., Simon, K.J., Pavlenco, A., Cheung, A., Brickelmaier, M., et al., (2015). Synthetic antibodies and peptides recognizing progressive multifocal leukoencephalopathy-specific point mutations in polyomavirus JC capsid viral protein 1. *MAbs* **7**, 681–692.
 104. Deshayes, K., Schaffer, M.L., Skelton, N.J., Nakamura, G. R., Kadkhodayan, S., Sidhu, S.S., (2002). Rapid identification of small binding motifs with high-throughput phage display: discovery of peptidic antagonists of IGF-1 function. *Chem. Biol.* **9**, 495–505.

3. Discussion

Here, in our studies, we answered numerous long-standing questions in the field by investigating the mechanistic principles of yeast GID and human CTLH E3 ligases. First, we have discovered that *Gid7* orthologs are assembly factors of GID and CTLH E3 ligases that allow transformation of the minimal catalytically active GID E3 ligase complex, named GID^{SR4}, into a supramolecular “Chelator-GID^{SR4}” complex (named so due to its chelator-like resemblance). Second, we have uncovered a multipronged substrate targeting mechanism by the supramolecular Chelator-GID^{SR4} E3 ligase assembly. Third, we have shown how a singular GID E3 ligase recognizes multiple substrates through the incorporation of stress-specific interchangeable substrate receptors that have pliable degron binding pockets. Fourth, we now know that similar structural and mechanistic features are conserved in human CTLH, suggesting potentially an analogous concept of substrate regulation in human.

The concept of a single E3 ligase utilizing interchangeable substrate receptors to target a multitude of substrates has long been demonstrated by the CRL E3 ligase family [57]. Now, a similar concept is arising for the GID/CTLH E3 ligase with its swappable substrate receptors and other additional assembly factors. In yeast, GID^{SR#} (where # specifies the number for each substrate receptor) acts as the minimal active E3 ligase assembly that binds various substrate degrons and simultaneously facilitates conformational activation of the Ubc8~Ub intermediate for ubiquitin transfer on to substrates [74]. *In vivo* the GID^{SR4} complex can degrade the gluconeogenic substrates *Mdh2*, *Icl1* and *Pck1*, but not *Fbp1*, which requires *Gid7* for its glucose-induced degradation [111]. The mechanistic insights determined from our cryo EM and biochemical experiments now explain how the previously uncharacterized *Gid7* initiates a 20-protein (roughly 1.3 MDa) giant assembly of the GID complex, named Chelator-GID^{SR4}, which is specifically tailored for ubiquitin targeting of the tetrameric structure of *Fbp1*.

The Chelator-GID^{SR4} assembly provides several advantages in targeting a tetrameric *Fbp1*. First, degron-binding pockets from two opposing *Gid4* substrate receptors serves for avid substrate recruitment by facilitating concurrent binding of the degrons from two *Fbp1* protomers in the same tetramer. However, there are two additional unoccupied terminal degrons from remaining protomers and we speculate that *Fbp1*-binding to Chelator-GID^{SR4} can potentially switch between the protomers to ubiquitylate all possible lysine sites in each protomer. Second, the Ubc8~Ub intermediates are activated by two opposing *Gid2*-*Gid9* catalytic domains, thus allowing efficient simultaneous ubiquitylation of multiple protomers of *Fbp1*. It is likely that such a dual ubiquitin targeting mechanism is capable of adequately ubiquitylating the substrate in one binding event for subsequent proteolytic steps. It will be interesting to visualize how such a ubiquitin transfer from two opposing catalytic sites is mediated. Third, the ubiquitylation of *Fbp1* has potential effect on metabolic activity of *Fbp1* itself. *Fbp1* is a metabolic enzyme with an allosteric AMP binding site and F-1,6-BP binding site. So far, we have observed an effect on AMP inhibition upon *Fbp1* ubiquitylation or mutation of target lysines in *Fbp1*. It is possible that *in vivo*, ubiquitylation could deem the enzyme *Fbp1* catalytically inactive. Alternatively, only *Fbp1* tetramers that have been catalytically inactivated through a different mechanism may be targets of ubiquitylation. At the moment, we can only speculate that ubiquitylation of *Fbp1* has some impact on its own activity. Many metabolic enzymes are oligomeric in nature and function strictly to regulate a specific process in a complex cellular pathway. There is definitely more to explore on such E3 ligase

systems that specifically act on different metabolic enzymes and regulate individual steps of the metabolic pathways.

In addition to demonstrating the ability of yeast GID E3 ligase to form distinct higher order assemblies we also elucidated some of the structural and mechanistic features of the human CTLH complex. CTLH^{SR4}, like GID^{SR4}, can act as a minimal active E3 and ubiquitylate model peptide substrates. Moreover, the human Gid7 orthologs, WDR26 and MKLN1, facilitate distinct supramolecular assemblies together with the core CTLH components [86, 111]. Taking into account other studies of human CTLH, we speculate that each of these assemblies may have distinct functions and/or distinct target substrates, as implied by varying phenotypic alterations upon their individual mutations. Moreover, WDR26 has been proposed as a substrate receptor for the transcription factor Hbp1 [77, 86]. Similarly, MKLN1 contains domains that likely bind different proteins and molecules such as phospholipids, galactose and collagen [112], making it also a potential CTLH substrate receptor candidate. Apart from canonical CTLH subunits, we show that CTLH interactor YPEL5 binds WDR26 [111]. However, whether it is simply some additional subunit or even plays some regulatory function in CTLH regulation is yet to be explored. Recently we have also shown that homologous CTLH subunits like RANBP9 and RANBP10 can also form distinct RANBP9-CTLH or RANBP10-CTLH complexes that are dependent on differentiation stages of erythroid cells [113], providing further evidences for expanding CTLH assembly and regulation. The specific domain architecture of WDR26 and MKLN1 may also allow for the assembly of distinct higher-order CTLH complexes comprising either WDR26 or MKLN1 or both to target substrates in diverse biological pathways. We have also recently seen increasing evidences of diverse E3-E3 oligomeric assemblies from other studies [58-60] and we can anticipate that this might be just the tip of an iceberg, which opens up new ways for understanding E3 ligase mediated regulation through higher-order oligomeric assemblies.

Using a combination of phage display, binding assays and X-ray crystallography, we further demonstrated that the GID/CTLH substrate receptors, such as human/yeast Gid4 and yeast Gid10, have pliable substrate binding pockets with loops that adopt different conformations to complement the bound degron or peptide sequences [80-82, 84]. We also identified novel non-Pro/N-peptides with bulky hydrophobic residues that can bind Gid4 and Gid10 with higher affinities compared to natural substrate degrons. This opens up new possibilities for finding physiological substrates of GID or CTLH that perhaps possess non-proline degrons, although bulky hydrophobic residues at the N-termini are likely to be generated only via proteolytic cleavages. Furthermore, such strong peptide binders of GID substrate receptors can be leveraged as potential therapeutic targets in the future. Indeed, Pfizer has already developed an exemplary molecule, named PFI-7, that binds human Gid4 with a binding affinity of 80 nM, potentially for designing novel PROTAC handles to target proteins of interest via the CTLH E3 ligase. There are still challenges that persist for development of therapeutic molecules for human CTLH. Unlike in yeast and Drosophila where we know the precise regulatory trigger for GID/CTLH mediated substrate regulation [65, 67, 68, 73, 74, 80, 85, 109], in human cells we have very little understanding of how, or under which stress or functional condition CTLH regulation is triggered. So far, this has remained the major bottleneck in understanding its substrate regulation. Moreover, we still lack clear evidence for the proposed physiological substrates of this complex. However, there is prospect for a high-affinity molecule, like the one developed by Pfizer, to be repurposed as a tool to identify the GID/CTLH substrates under different cellular conditions.

To sum up, we now understand that there is not a single yeast GID or human CTLH complex, rather a collection of diverse multiprotein assemblies (in case of yeast GID, specific stress and nutrient-responsive assemblies), each of which could have individual roles in regulating distinct substrates in multiple biological pathways. Thus, the multifaceted nature of GID/CTLH allows for both interchangeable substrate receptors that are capable of conforming to diverse degron sequences, and supramolecular assemblies that are capable of targeting specific oligomeric substrates. We expect that these mechanistic principles of yeast GID and human CTLH are evolutionarily conserved in other organisms, allowing GID and CTLH complexes to serve as a common regulatory switch.

4. Methods

4.1. Cloning and plasmids preparation

The individual genes of yeast GID subunits and the gluconeogenic substrates were originally amplified from *S. cerevisiae* BY4742 genomic DNA. The individual genes for human CTLH subunits were obtained from in-house human cDNA library, except for hGid4 and WDR26, which were synthesized as codon-optimized versions for bacterial expression and insect cell expression system respectively (GeneArt gene synthesis, Thermo Fischer Scientific).

Majority of the proteins that were expressed singly were cloned into pGEX or pRSF vectors with N-terminal GST or C-terminal 6XHis tags, with or without a TEV cleavage site. The constructs were cloned into respective vectors using Gibson assembly protocol (Gibson et al. 2009) except in case of mutagenesis, where the QuikChange Site-Directed Mutagenesis protocol (Stratagene) was used. After PCR, Dpn1 digestion was done at 37°C overnight followed by PCR purification except for mutagenesis where we skipped the PCR purification step. DNA transformations were done in DH5 α cells and DNA was isolated using miniprep kit (Qiagen) and verified using sequencing (Eurofins). For protein expression, the constructs were further transformed into BL21(DE3) pRIL cells.

For the constructs in insect cells, the genes were initially cloned into pLIB vectors and verified by sequencing. In order to combine the GID and CTLH subunits into a single expression system, they were further cloned into a single baculoviral expression vector using biGBac assembly technique (Weissmann et al., 2016). For all the insect cell expression, the constructs were transformed using DH10EMBacY cells and bacmids were generated.

4.2. Protein expression and purification for biochemistry and structural studies

All the GID and CTLH complexes used in the biochemical assays and cryo EM were expressed in insect cells. Insect cells (Sf9) are transfected with prepared bacmids and baculovirus variants were propagated from P1 till P3 stages, followed by final step of expression in Hi5 cells using suspension media (EX-CELL 420 Serum-Free Medium) at 27°C.

Insect cells were harvested by spinning at 450 g for 15 mins, and the pellets were resuspended in a lysis buffer containing 50 mM Hepes pH 7.5, 200 mM NaCl, 5 mM DTT, 10 μ g/ml leupeptin, 20 μ g/ml aprotinin, 2 mM benzamidine, EDTA-free protease inhibitor tablet (1 tablet per 50 ml of the buffer) and 1 mM PMSF.

The recombinant GID/CTLH complexes affinity purification was carried out by using twin-Strep tag fused at the Gid8/TWA1 C-terminus, except for RanBP9/TWA1/ARMC8/Gid4/WDR26/YPEL5 subcomplex, for which the tag was fused to the ARMC8 N-terminus. Further purification was performed by anion exchange chromatography and size exclusion chromatography (SEC). As a final buffer for SEC either 25 mM Hepes pH 7.5, 200 mM NaCl and 5 mM (Buffer A) or 1 mM DTT (Buffer B) was taken depending whether it was used for cryo EM and biochemical assays, respectively. For GID complexes for the cryo

EM, bacterially purified Gid4 (Δ 1-116) or Gid7 were added before SEC. Also, for the human CTLH complexes used for cryo EM, hGid4 (Δ 1-99) was added before SEC.

All the bacterial expression was done in *E. coli* BL21(DE3)RIL cells. Cells were harvested by spinning at full speed (5000 rpm) for 15 mins and pellets were resuspended in the lysis buffer before further purification. WT ubiquitin was purified via glacial acetic acid method [114], followed by gravity S column ion exchange chromatography and SEC. Different Ub variants as well as WT Ub used for the ubiquitin chain type determination assay were expressed as GST-3C fusions were purified by glutathione affinity chromatography, followed by incubation with HRV-3C protease for 3 hours at room temperature and a SEC at the end. The mutant and WT versions of Gid7, yeast and human and yeast Gid4 were expressed as GST-TEV fusions and were purified by glutathione affinity chromatography, followed by overnight TEV cleavage at 4°C using tobacco etch virus (TEV) protease. Further purification was carried out with SEC followed by a pass-back over glutathione affinity resin to get rid of the remaining uncleaved GST-fusion protein and free GST. Yeast and human E2s Ubc8 and Ube2H, Fbp1 WT and mutants, Mdh2 were expressed as C-terminal 6xHis-tagged versions and purified using nickel affinity chromatography, followed by anion exchange and SEC.

4.3. Purification of endogenous yeast GID for cryo EM

For obtaining the endogenous complex for cryo EM, yeast strain with Gid7 and Gid5 C-terminally tagged at their endogenous loci with an HA and 3xFLAG tag respectively, was taken. 3 liters of yeast were grown at 30°C first in YPD medium for 8 hours followed by resuspension in YPE medium (1% yeast extract, 2% peptone, 2% ethanol) to OD₆₀₀ of 1.0. Cells were grown further for 19 hours and harvested at OD₆₀₀ of 18.0. The cells were pelleted by spinning at 5000 rpm for 10 mins. The pellet was resuspended in the lysis buffer containing 50 mM HEPES pH 7.5, 150 mM NaCl, 1 mM CaCl₂, 0.2 M sorbitol, complete protease inhibitor tablets and frozen in liquid nitrogen in the form of small bead-like droplets. The frozen yeast pellets were lysed using a cryo-mill (SPEX Sample Prep-6875 Freezer/Mill) and the yeast powder thus obtained was kept at -80°C. For the complex purification, frozen yeast powder was thawed by rolling in the cold room for an hour and subjected to homogenization using Dounce homogenizer. The lysate was then centrifuged at 35,000 rpm for 10 minutes and the supernatant was incubated with ANTI-FLAG M2 affinity resin for an hour. The resins were then washed several times before protein elution using 3xFLAG peptide. The eluted complex was run on SDS-PAGE and further concentrated to 1 mg/ml for cryo EM purposes.

4.4. Sortase mediated fluorescent labeling of substrates

For the fluorescent tagging of substrates Fbp1, Mdh2 and Pck1, constructs containing additional LPETGG motif at the C-terminus prior to the 6xHis tag were designed. The fluorescent labelling was performed using a sortase A-mediated reaction, which catalysed fusion of fluorescein to the C-terminus of Fbp1. The reaction was proceeded by adding 50 μ M of Fbp1 C-terminally tagged with a sortag (LPETGG), 250 μ M of a fluorescent peptide (GGGGGFYVK-FAM) and 50 μ M of sortase A and a buffer comprising 50 mM Tris-HCl pH 8, 150 mM NaCl and 10 mM CaCl₂ and incubating the mix for 30 min at room temperature. The

reaction mixture was consecutively passed-back through the Ni-NTA sepharose resin to get rid of unreacted substrates and further purified using SEC.

All other labelled and unlabeled peptides used in the biochemical assays were synthesized in the MPIB Biochemistry Core Facility by Stephan Ubel or Stefan Pettera.

4.5. ^{15}N labelling of hGid4 for NMR

For the NMR experiments that were done to access binding of different Pro/N- peptides, hGid4(Δ 1-115) was expressed with N-terminal 6xHis tag in the presence of ^{15}N containing media. 50 ml of the preculture was spun at 3000 rpm for 20 mins followed by resuspension of the pellet in 1 litre of 1x M9 cell growth medium containing 2 g glucose, 5 mg/ml thiamine chloride, 1 M MgSO_4 , 1 M CaCl_2 , 1g $^{15}\text{NH}_4\text{Cl}$, trace elements and antibiotics. The cultures were then grown at 37°C and 200 rpm until the OD_{600} of 0.5-0.8 to was reached. The temperature was then reduced to 23°C and kept for an hour before inducing with 0.6 M IPTG followed by continuous growth overnight at 23°C, 200 rpm. For the protein purification affinity chromatography was done using nickel-resins followed by SEC in buffer containing 25 mM phosphate buffer pH 7.8, 150 mM NaCl and 1 mM DTT which was suitable for NMR puporses.

4.6. *In vitro* biochemical assays with yeast GID complex

The *in vitro* ubiquitylation assays were also performed using labelled substrate or by using western blotting for His tag. The *in vitro* activity assays were performed at room temperature in a buffer containing 25 mM Hepes pH 7.5, 150 mM NaCl, 5 mM ATP and 10 mM MgCl_2 . To ensure that all the reaction mixtures contained equal concentrations of WT and mutant versions of Gid4 and Gid7, these components of the GID complex were added exogenously for most assays. All the reactions were quenched at indicated timepoints by mixing with SDS-PAGE loading buffer. Ubiquitylation of fluorescent substrates was visualized by a fluorescent scan of SDS-PAGE gel using the Amersham Typhoon imager (GE Healthcare) and western blots were visualized using Amersham Imager 600 (GE Healthcare).

4.6.1. Multi-turnover ubiquitylation assays

The multi-turnover ubiquitylation assays to assess the effect of Gid7 and Gid4 were performed by using either the labelled full-length and peptide versions of Fbp1, or labelled full-length Mdh2 or Pck1. The assay mix consisted of 0.2 μM Uba1, 1 μM Ubc8, 0.5 μM GID^{Ant} , 0 or 1 μM Gid4, 0 or 2 μM Gid7, 1 μM full-length Fbp1-FAM/Mdh2-FAM/Pck1-FAM or a fluorescently labelled model peptide substrate and 20 μM Ub. The fluorescently labelled model peptide substrate was designed such that the N-terminus contained the Fbp1 degron PTLV followed by a linker with a single lysine placed at position 23. The lysine placement was done based on the distance between Gid4 and the RING domain measured in the structure of GID^{SR4} . Furthermore, to test whether the effect of ubiquitylation in case of Gid7 added exogenously versus Gid7 expressed with the other complex subunits multi-turnover assay was done under the same conditions as mention earlier using labelled full length Fbp1.

4.6.2. Ubiquitin discharge assay

The intrinsic activity of GID E3 in the presence and absence of *Gid7* was measured in a substrate-independent pulse-chase assay, where the discharge of preassembled Ubc8~Ub to free lysine was followed. In the pulse reaction, Ubc8 was loaded with Ub by mixing 0.5 μM Uba1, 10 μM Ubc8 and 30 μM Ub and incubating for 15 mins. The reaction was quenched by addition of 50 mM EDTA and incubation on ice for 5 minutes. During the chase reaction, the loaded Ubc8~Ub was mixed with an equal volume of another reaction mix containing 1 μM GID^{SR4} complex, 0 or 2 μM *Gid7* (WT or (Δ 1-284) mutant) and 25 mM lysine pH 8.0. The reaction was carried out at room temperature and was quenched at different timepoints in non-reducing SDS loading buffer.

4.6.3. Competition assay

A ubiquitylation assay with competing full-length protein or peptide was devised to verify the avid binding of Fbp1 to Chelator-GID^{SR4}. The assay was performed using multi-turnover format where the reaction mixture was prepared with 0.2 μM Uba1, 1 μM Ubc8, 0.5 μM E3 GID^{SR4}, 0 or 2 μM *Gid7* (WT or its (Δ 1-284) mutant), 0.5 μM of fluorescently labelled full-length tetrameric Fbp1 or a monomeric model peptide containing Fbp1 degron, 20 μM of a competing unlabeled substrate (full length Fbp1-6xHis or a 10-residue peptide containing Fbp1 N-terminal sequence) and 20 μM Ub. The reaction was carried out at room temperature and was quenched at different timepoints in SDS loading buffer.

4.6.4. Assay for target lysine site determination

In order to determine the preferred target lysines in Fbp1 using di-Gly proteomic approach, a ubiquitylation assay was performed in bulk and submitted for analysis. The goal was to capture the initial ubiquitylation events, therefore a single-turnover pulse-chase assay was done using a significantly higher concentration of the substrate compared to Ubc8~Ub. First, 1 μM Ubc8 was loaded with 30 μM lysine-less ubiquitin and 0.5 μM Uba1 for 15 minutes at room temperature followed by quenching using 50 mM EDTA. During the chase, the charged Ubc8~Ub was mixed with an equal volume of a second mix containing 1 μM GID^{Ant}, 2 μM *Gid7*, 2 μM *Gid4* and 4 μM Fbp1. The reaction was incubated in room temperature for 1 minute and quenched by adding 10 mM DTT, which was removed by desalting prior to using it for mass spectrometry experiments. Further mass spectrometry experiments and analysis were done by Fynn Hansen in the Mann Department.

4.6.5. Determination of Michealis-Menten kinetics for Fbp1 ubiquitylation by GID E3

The Michaelis-Menten constant K_m for Fbp1 ubiquitylation by GID E3 was determined by multi-turnover assays, where the E3 concentration was titrated and the substrate levels were kept constant below K_m . Different complexes - GID^{SR4}, GID^{SR4} mixed with *Gid7* as well as a purified Chelator-GID^{SR4} (GID^{SR4} co-expressed with *Gid7*) were used for the assay. For the assay with GID^{SR4}, 0.2 μM Uba1, 1 μM Ubc8, 0.25-8 μM GID^{SR4}, 0.5 μM Fbp1-FAM and 20 μM Ub, were mixed and reaction was quenched after 8 minutes. Similarly, for GID^{SR4} exogenously mixed with *Gid7* sample, reaction mix containing 0.2 μM Uba1, 1 μM Ubc8, 0.025-0.8 μM GID^{SR4} mixed with a 2-fold excess of *Gid7*, 0.1 μM Fbp1-FAM and 20 μM Ub were quenched after 3

minutes. In the case of Chelator-GID^{SR4}, the reaction mixes containing 0.2 μM Uba1, 1 μM Ubc8, 0.03-1 μM Chelator-GID^{SR4}, 0.1 μM Fbp1-FAM and 20 μM Ub were quenched after 2 minutes. Reactions were quenched at timepoints in which the initial velocities of all reactions were well within the linear range, which was determined separately by running time courses for these reactions with highest E3 concentration for each case. The reaction was run on SDS-PAGE and quantified using ImageQuant (GE healthcare; version 8.2). Initial velocities were calculated by taking the fraction of Fbp1 that had been modified by one or more ubiquitin and dividing by time. Initial velocities were then plotted as a function of E3 concentration in GraphPad Prism and fitted to the Michaelis-Menten equation using non-linear curve fitting. All reactions were performed in duplicates.

For the k_{cat} measurement, initial velocities were measured for both GID^{SR4} and Chelator-GID^{SR4} by performing a time course assay while keeping ratios of both E3 to K_m and substrate to K_m the same for each E3 complex (2.7 and 0.4, respectively). The fraction of ubiquitylated Fbp1 was determined as mentioned above and plotted in GraphPad Prism as a function of time and the rate of the reaction was estimated by linear regression. Having calculated the rate, initial velocities V_0 were calculated using the following equation: $V_0 = rate \cdot [S]$. V_{max} was then estimated using a modified form of the Michaelis-Menten equation: $V_{max} = \frac{V_0 \cdot (K_m + S)}{S}$, where $S = \frac{K_m}{2.5}$ because the substrate concentration was 2.5 times lower than K_m . To obtain k_{cat} values, V_{max} was divided by the E3 concentration: $k_{cat} = \frac{V_{max}}{[E3]}$.

All the kinetic experiments were designed with the guidance from Gary Kleiger.

4.7. Size exclusion chromatography for characterization of GID complex assembly

To determine the shift in size of the complex upon addition of Gid7, SEC analysis was done by running 200 μl of 10 μM Gid7 alone, GID^{SR4} alone and both together (mixed in 1:1 ratio) onto a Superose 6 column (GE Healthcare) equilibrated with 25 mM Hepes 7.5, 150 mM NaCl and 5 mM DTT. Individual SEC fractions were run on SDS-PAGE for further analysis.

4.8. Size exclusion chromatography-Multi angle light scattering (SEC-MALS)

The oligomeric state of Fbp1 and Gid7 were determined by performing SEC-MALS. For each run, 100 μl of samples at 1 mg/mL were loaded onto Superdex 200 column equilibrated with a buffer containing 25 mM Hepes pH 7.5, 150 mM NaCl and 5 mM DTT. SEC-MALS was conducted in the MPIB Biochemistry Core Facility with the help of Monica Zobawa.

4.9. Fbp1 enzyme activity assay

Fbp1 enzyme activity was conducted to test if the ubiquitylation or mutation of the target lysines had an effect on the enzymatic activity of the Fbp1 itself. For this EnzChek™ Phosphate Assay Kit (ThermoFisher Scientific) was used. This is a colorimetric assay that quantifies inorganic phosphate (P_i) released from fructose-1,6-bisphosphate by Fbp1 through enzymatic conversion of 2-amino-6-mercapto-7-methyl-purine riboside (MESG) to ribose 1-

phosphate and 2-amino-6-mercapto-7-methylpurine by purine nucleoside phosphorylase (PNP) leading to a shift in maximum absorbance from 330 nm for MESG to 360 nm for the final reaction product (2-amino-6-mercapto-7-methylpurine) which is then measured as a readout.

The fully ubiquitylated Fbp1 was made by performing an overnight multiturnover ubiquitylation reaction at room temperature consisting of 0.2 μM Uba1, 1 μM Ubc8, 0.5 μM GID^{Ant}, 1 μM Gid4, 2 μM Gid7, 10 μM Fbp1-V5-2xS and 100 μM 6xHis-3c-Ub. The reaction mix was further subjected to SEC (Superose 6 column) to separate different components of the assay and only the fractions corresponding to the ubiquitylated Fbp1 were pooled together. This was then subjected to nickel affinity purification to pull on only ubiquitin-bound Fbp1. After throughout wash, the bound ubiquitylated Fbp1 was eluted and visualized by SDS-PAGE.

Fbp1 activity assays were performed at room temperature and using either WT, target lysine mutant (K32A/K35A/K280A/K281A) or fully ubiquitylated Fbp1. First, MESG, PNP and 20x reaction buffer, 0.5 mM fructose-1,6-bisphosphate substrate and 0.6 mM AMP (for the Fbp1 inhibition assay) were pre-mixed and incubated for 5 min. Then, the reaction was initiated by addition of 53 nM of different versions of Fbp1, and the reaction progress was followed by measuring a time-course of absorbance at 360 nm using CLARIOStar Plus microplate reader (BMG LABTECH) in a UV-transparent 96-well plate. For the analysis, the values of A_{360} obtained for the buffer-only control were deducted from all the experimental measurements and plots were made using GraphPad Prism.

4.10. Fluorescence polarization (FP) assays

For the FP experiments performed to measure binding affinity, 2-fold dilution series of hGid4 ($\Delta 1-115$) was prepared in the FP buffer containing 25 mM Tris pH 8.0, 150 mM NaCl, 0.5 mM DTT and 20 nM of fluorescent PGLWKS-FAM and simultaneously a separate mix with non-binding GGGGRHDS(P)GLDS(P)MKDEE-FAM control peptide was also prepared. The mixed samples were equilibrated at room temperature for 5 mins and transferred to Greiner 384-well flat bottom black plates. The polarization values were measured in CLARIOstar microplate reader (BMG LABTECH) using the excitation at 482 nm and emission at 530 nm. The data were then fit to one site-binding model in GraphPad Prism to determine K_D value.

For further comparison of the binding of several unlabeled ligands to hGid4, we performed competitive FP measurements. Based on the FP plot from the above experiment, we took the hGid4 concentration with ~60% saturation of the FP signal (6.8 μM hGid4). Then we performed 2-fold dilution series of unlabeled competitors in FP buffer mixed with hGid4 and the fluorescent peptide from above. The measurements were taken after a few min incubation. The data were plotted relative to the FP signal in the absence of an inhibitor as a function of log (ligand concentration) and analyzed with log (inhibitor) vs. response model to determine IC50 values. To determine relative inhibitory strength of the ligands, the determined IC50 values were divided by that of PGLWKS.

4.11. Peptide spot array binding assay

First, the array of peptides derived from the PGLWKS sequence with all 20 amino acid substituted at different positions either position 1, 2 and 3 together or position 4 and position 5 separately were synthesized on a membrane in the MPIB biochemistry core facility with the help of Jochen Rech following the previously established protocols (Hilpert et al., 2007). For the spot array binding assay, the membrane blot was first blocked with 3% milk in TBST buffer (20 mM Tris, 150 mM NaCl and 0.1% Tween 20) for 1 hour at room temperature. Then the membrane was incubated with the human Gid4 (Δ 1-99) was diluted to 10 μ g/ml in the buffer containing 150 mM NaCl, 25 mM HEPES pH 7.5, 0.5 mM EDTA pH 8.0, 10% glycerol, 0.1% Tween 20, 2% milk and 1 mM DTT overnight at 4°C with gentle shaking. Next day the membrane was washed with TBST buffer 3 times, incubated with primary anti-hGid4 sheep monoclonal antibody (1:500) for 3 hours with gentle shaking, followed by multiple washing steps with TBST and 1 hour incubation with secondary HRP-conjugated anti-sheep (1:5000) antibody. The membranes were again washed multiple times with TBST and the membrane was analyzed by chemiluminescence in Amersham Imager 800 (GE Healthcare).

4.12. Isothermal titration calorimetry (ITC) binding assays

In order to measure the binding affinity of different peptides to hGid4 (Δ 1-115) and yGid10 (Δ 1-56) ITC was performed. All peptides were first dissolved in the SEC buffer used for purification of substrate receptors containing 25 mM HEPES pH 7.5, 150 mM NaCl and 0.5 mM TCEP and their concentration was measured by absorbance at 280 nm. For this purpose, a single tryptophan residue was appended at peptides' C-termini to facilitate determination of peptide concentration using absorbance at 280 nm if not present in the sequence. All the experiments were carried out in the MicroCal PEAQ-ITC instrument (Malvern Pananalytica) at 25°C by titrating peptides to either hGid4 or yGid10. Peptides were titrated using the following conditions: 19 x 2 μ l injections, with 4 s injection time and 150 s equilibration time between the injections. The reference power was set to 10 μ cal/s. Several rounds of optimization of the concentration of the peptides and substrate receptors were done according to the ITC plot and the estimated K_D values. The final raw ITC data were analyzed using One Set of Sites binding model (Malvern Pananalytica) to determine K_D and stoichiometry of the binding events (n) and the plots were prepared in GraphPad Prism.

4.13. Yeast substrate degradation assays

All the original yeast strains used for the purpose was obtained from either Christine, Viola or Laura. In order to test the effect of dependency of Pck1 degradation on Gid7 and Gid4, degradation assay was performed using the promoter reference technique adapted from the Varshavsky lab. The respective yeast strains either WT, Δ Gid4 or Δ Gid7 were transformed with a plasmid harboring the open reading frame of Pck1 and the control protein DHFR, both expressed from identical promoters. The same promoter reference technique was also applied to test the effect of glucose-induced degradation of Fbp1 and its lysine mutants, and degron swapped versions of GID substrates Mdh2 and Fbp1. For the first experiment only WT yeast strains were transformed with a plasmid harboring the open reading frames of Fbp1-3xFLAG or the lysine mutant versions (K280R/K281R, K32R/K35R, K32R/K35R/K28R/K281R) and the control protein DHFR-3xHA, and for the degron swap experiment, WT and Δ Gid7 yeast strains

were transformed with a plasmid harboring the open reading frame of either Fbp1-3xFLAG or Mdh2-3xFLAG or their mutant versions with degron swaps (Fbp1^{Mdh2 degron}-3xFLAG and Mdh2^{Fbp1 degron}-3xFLAG) and the control protein DHFR-3xHA, both expressed from identical promoters.

Moreover, another degradation assay was performed to test the effect of the novel high-affinity yGid4-binding sequences on glucose-induced instability onto Fbp1. Since all these sequences were N-terminal bulky hydrophobic residues, to ensure their exposure they were made as N-terminal fusions to ubiquitin. For this, all Fbp1 versions (FDITGFSW-Fbp1(Δ 1-9)-3xFLAG, LDVSWFEW-Fbp1(Δ 1-9)-3xFLAG, a positive control IGLW-Fbp1(Δ 1-5)-3xFLAG [83] and Fbp1-3xFLAG) were expressed as N-terminal fusions to ubiquitin[83, 115].

The same growth conditions at 30°C were used for all the degradation assays. First, cells were grown in SD-glucose medium to OD₆₀₀ of 1.0 (8 hours) which was followed by carbon starvation in SE medium (0.17% yeast nitrogen base, 0.5% ammonium sulfate, 2% ethanol, amino acid mix) for 19 hours. Then the yeast at the equivalent of 1 OD₆₀₀ was transferred to SD-glucose medium containing 0.5 mM tetracycline and timepoints were taken in between the growth. Addition of tetracycline resulted in translation inhibition upon binding of tetracycline to specific RNA-aptamers within ORFs of the examined and control proteins. Depending on the experiment, at individual timepoints 1 mL of cells were harvested and pellets were flash frozen in liquid nitrogen. For the cell lysis, the frozen pellets were thawed and resuspended in 800 μ L 0.2 M NaOH, followed by 20 min incubation on ice and subsequent centrifugation at 11,200xg for 1 minute at 4°C. After the removal of the supernatant, pellets were resuspended in 50 μ L HU buffer (8 M Urea, 5% SDS, 1 mM EDTA, 100 mM DTT, 200 mM Tris pH 6.8, protease inhibitor, bromophenol blue), heated at 70°C for 10 minutes and then centrifuged again for 5 minutes at 11,200xg and at 4°C. The samples were then loaded on to the SDS-PAGE, and the substrates and the control protein DHFR were visualized by immunoblotting. For the antibodies, anti-FLAG or anti-HA primary antibodies were used together with DyLight fluorophore conjugated secondary antibodies, and imaged using a Typhoon scanner (GE Healthcare). All the quantification was done using the ImageStudioLite software (LI-COR). For the final graphs, the substrate signal was first normalized relative to the DHFR signal and then to the time point zero (time point at the end of glucose starvation was considered time point zero). For all the assays, three biological replicates were performed.

4.14. Cryo EM sample preparation and data collection

All the cryo EM grids were prepared using Vitrobot Mark IV (Thermo Fisher Scientific) and using Quantifoil holey carbon grids (R1.2/1.3 200 mesh). First, the grids were glow-discharged, and then loaded onto the Vitrobot. For each grid, 3.5 μ l of the purified protein at 0.3-0.5 mg/ml was applied. Grids were then blotted with Whatman no. 1 filter paper using blot time of 3 s and blot force of 3 followed by vitrification by plunging freezing in liquid ethane.

All the cryo EM data were first screened on a Talos Arctica or Glacios transmission electron microscope operated at 200 kV, equipped with a Falcon III or K2 direct electron detector, respectively. After each screening session, overnight data was collected and data was processed using Relion to check the sample and grid quality. Automated data collection was

carried out using EPU software (for Arctica) or using Serial EM (for Glacios). For the high-resolution data acquisition, data was collected on a FEI Titan Krios microscope that operated at 300 kV, equipped with a post-column GIF and a K3 Summit direct electron detector. Automated data collection was done using SerialEM [116]. Data collection for the Titan Krios were carried out with the help of cryo EM facility managers Daniel Bollschweiler and Tillman Schäfer.

4.14.1. Cryo EM data processing

For the low-resolution data collections from Arctica or Glacios TEM, all the cryo EM data processing was done using Relion (Fernandez-Leiro and Scheres, 2017; Scheres, 2012; Zivanov et al., 2018). First, the frames were motion-corrected with dose weighting using MotionCorr2 and the contrast transfer function estimation was done using Gctf. Particles were auto picked using a low-resolution template in Gautomatch. For Krios datasets, first all the movies were pre-processed with Focus [117] during the data collection upto the particle picking step. Rest of the processing was carried out using Relion [118-120]. Several rounds of 2D and 3D classifications were done followed by 3D auto refinement without and with a mask. In order to further improve the map quality, further 3D classification without particle alignment, followed by focused refinement were done post 3D refinement. All the final maps were post-processed by automatic B-factor weighting and high-resolution noise substitution. The estimated resolutions of all reconstructions are based on the gold-standard Fourier Shell Correlation (FSC) at 0.143 criterion.

For the high-resolution map of the SRS module, a focused 3D classification without particle alignment was performed with a mask over GID^{SR4} after the 3D refinement. This was followed by focused refinement by masking out the Cat module. For the high-resolution maps of the Cat and SA modules, first the particle number was doubled by creating masks for each half of the complex, followed by signal subtraction and joining of the particles. The resulting particles were aligned by auto-refinement. This was followed by focused 3D classification without particle alignment with masks for only Cat and SA modules. The best set of particles were CTF refined followed by final auto-refinement. All the final maps were post-processed by automatic B-factor weighting and high-resolution noise substitution. The estimated resolutions of all reconstructions are based on the gold-standard Fourier Shell Correlation (FSC) at 0.143 criterion.

4.14.2. Model building and refinement

All the models were manually build using Coot and all structural analysis was carried out using Chimera, ChimeraX and Pymol-v2.3.4. For the structure of the SRS module in Chelator-GID^{SR4}, atomic coordinates of GID^{SR4} from PDB: 6SWY was fitted to the obtained map and refined manually. The loops of Gid4 near the substrate binding pocket and the Fbp1 degron were built manually. For the Cat module everything was built manually and the geometry of the zinc coordination sites was allocated based on other RING domain structures available in PDB database. The models were iteratively built with many rounds of manual building in Coot and real space refinement in Phenix.

4.15. X-ray crystallography and data processing

For the Fbp1 crystallization, Fbp1-6xHis was purified and concentrated to 10 mg/ml and submitted to the MPIB Crystallization Facility for crystallization trials. Crystals for Fbp1 were obtained using a sitting drop vapor diffusion method at 4°C in the buffer composition of 16% PEG 3350, 0.2 M MgCl₂ and 0.1 M Bis-Tris pH 6. Crystals were cryoprotected using 20% ethylene glycol and flash frozen in liquid nitrogen before shipping for data collection. Similarly, hGid4 (Δ 1-99) was purified and concentrated to 10 mg/ml for the crystal trials. The crystals were obtained in the conditions with 18% PEG 3350 with 0.2 M ammonium nitrate and 0.1 M Bis-Tris buffer at pH 7 at room temperature. Crystals were cryoprotected in 20% ethylene glycol and flash frozen in liquid nitrogen before shipping for data collection.

For Fbp1 crystals, diffraction dataset was recorded at PXII beam line, Swiss Light Source (SLS) Villigen, Switzerland and for the hGid4 crystals dataset were recorded at X10SA beam line. All the crystal shipment and data collection were performed by Rajan J. Prabu and Jerome Basquin (MPIB crystal facility). Both the crystal dataset was indexed, integrated and scaled using XDS package and phasing was done by molecular replacement with PHASER within the PHENIX software suite, using PDB: 1FTA for Fbp1 and PDB ID: 6CDC for hGid4. This was followed by iterative rounds of manual model building in Coot and refinement using phenix.refine.

5. References

1. Mark, K.G. and M. Rape, *Ubiquitin-dependent regulation of transcription in development and disease*. EMBO Rep, 2021. **22**(4): p. e51078.
2. Filbeck, S., et al., *Ribosome-associated quality-control mechanisms from bacteria to humans*. Mol Cell, 2022. **82**(8): p. 1451-1466.
3. Reinle, K., A. Mogk, and B. Bukau, *The Diverse Functions of Small Heat Shock Proteins in the Proteostasis Network*. J Mol Biol, 2022. **434**(1): p. 167157.
4. Wang, L. and P. Walter, *Msp1/ATAD1 in Protein Quality Control and Regulation of Synaptic Activities*. Annu Rev Cell Dev Biol, 2020. **36**: p. 141-164.
5. Breckel, C.A. and M. Hochstrasser, *Ubiquitin Ligase Redundancy and Nuclear-Cytoplasmic Localization in Yeast Protein Quality Control*. Biomolecules, 2021. **11**(12).
6. Chino, H. and N. Mizushima, *ER-Phagy: Quality and Quantity Control of the Endoplasmic Reticulum by Autophagy*. Cold Spring Harb Perspect Biol, 2022.
7. Pla-Prats, C. and N.H. Thoma, *Quality control of protein complex assembly by the ubiquitin-proteasome system*. Trends Cell Biol, 2022. **32**(8): p. 696-706.
8. Sherpa, D., J. Chrustowicz, and B.A. Schulman, *How the ends signal the end: Regulation by E3 ubiquitin ligases recognizing protein termini*. Mol Cell, 2022. **82**(8): p. 1424-1438.
9. Levine, B. and G. Kroemer, *Biological Functions of Autophagy Genes: A Disease Perspective*. Cell, 2019. **176**(1-2): p. 11-42.
10. Ciechanover, A., Y. Hod, and A. Hershko, *A heat-stable polypeptide component of an ATP-dependent proteolytic system from reticulocytes*. Biochem Biophys Res Commun, 1978. **81**(4): p. 1100-5.
11. Etlinger, J.D. and A.L. Goldberg, *A soluble ATP-dependent proteolytic system responsible for the degradation of abnormal proteins in reticulocytes*. Proc Natl Acad Sci U S A, 1977. **74**(1): p. 54-8.
12. Hershko, A., A. Ciechanover, and I.A. Rose, *Resolution of the ATP-dependent proteolytic system from reticulocytes: a component that interacts with ATP*. Proc Natl Acad Sci U S A, 1979. **76**(7): p. 3107-10.
13. Hershko, A. and A. Ciechanover, *The ubiquitin system for protein degradation*. Annu Rev Biochem, 1992. **61**: p. 761-807.
14. Driscoll, J. and A.L. Goldberg, *The proteasome (multicatalytic protease) is a component of the 1500-kDa proteolytic complex which degrades ubiquitin-conjugated proteins*. J Biol Chem, 1990. **265**(9): p. 4789-92.
15. Hough, R., G. Pratt, and M. Rechsteiner, *Ubiquitin-lysozyme conjugates. Identification and characterization of an ATP-dependent protease from rabbit reticulocyte lysates*. J Biol Chem, 1986. **261**(5): p. 2400-8.
16. Bartel, B., I. Wunning, and A. Varshavsky, *The recognition component of the N-end rule pathway*. EMBO J, 1990. **9**(10): p. 3179-89.
17. Jentsch, S., J.P. McGrath, and A. Varshavsky, *The yeast DNA repair gene RAD6 encodes a ubiquitin-conjugating enzyme*. Nature, 1987. **329**(6135): p. 131-4.
18. McGrath, J.P., S. Jentsch, and A. Varshavsky, *UBA 1: an essential yeast gene encoding ubiquitin-activating enzyme*. EMBO J, 1991. **10**(1): p. 227-36.
19. Ozkaynak, E., et al., *The yeast ubiquitin genes: a family of natural gene fusions*. EMBO J, 1987. **6**(5): p. 1429-39.

20. Bachmair, A., D. Finley, and A. Varshavsky, *In vivo half-life of a protein is a function of its amino-terminal residue*. Science, 1986. **234**(4773): p. 179-86.
21. Hochstrasser, M., et al., *The short-lived MAT alpha 2 transcriptional regulator is ubiquitinated in vivo*. Proc Natl Acad Sci U S A, 1991. **88**(11): p. 4606-10.
22. Oh, E., D. Akopian, and M. Rape, *Principles of Ubiquitin-Dependent Signaling*. Annu Rev Cell Dev Biol, 2018. **34**: p. 137-162.
23. Wiborg, O., et al., *The human ubiquitin multigene family: some genes contain multiple directly repeated ubiquitin coding sequences*. EMBO J, 1985. **4**(3): p. 755-9.
24. Squir, D.R. and S. Virdee, *A new dawn beyond lysine ubiquitination*. Nat Chem Biol, 2022. **18**(8): p. 802-811.
25. Kwon, Y.T. and A. Ciechanover, *The Ubiquitin Code in the Ubiquitin-Proteasome System and Autophagy*. Trends Biochem Sci, 2017. **42**(11): p. 873-886.
26. Swatek, K.N. and D. Komander, *Ubiquitin modifications*. Cell Res, 2016. **26**(4): p. 399-422.
27. Huang, L., et al., *Structure of an E6AP-UbcH7 complex: insights into ubiquitination by the E2-E3 enzyme cascade*. Science, 1999. **286**(5443): p. 1321-6.
28. Lee, I. and H. Schindelin, *Structural insights into E1-catalyzed ubiquitin activation and transfer to conjugating enzymes*. Cell, 2008. **134**(2): p. 268-78.
29. Olsen, S.K. and C.D. Lima, *Structure of a ubiquitin E1-E2 complex: insights to E1-E2 thioester transfer*. Mol Cell, 2013. **49**(5): p. 884-96.
30. Scott, D.C., et al., *Structure of a RING E3 trapped in action reveals ligation mechanism for the ubiquitin-like protein NEDD8*. Cell, 2014. **157**(7): p. 1671-84.
31. Baek, K., et al., *NEDD8 nucleates a multivalent cullin-RING-UBE2D ubiquitin ligation assembly*. Nature, 2020. **578**(7795): p. 461-466.
32. Calabrese, M.F., et al., *A RING E3-substrate complex poised for ubiquitin-like protein transfer: structural insights into cullin-RING ligases*. Nat Struct Mol Biol, 2011. **18**(8): p. 947-9.
33. Hu, M., et al., *Structure and mechanisms of the proteasome-associated deubiquitinating enzyme USP14*. EMBO J, 2005. **24**(21): p. 3747-56.
34. Lee, B.H., et al., *USP14 deubiquitinates proteasome-bound substrates that are ubiquitinated at multiple sites*. Nature, 2016. **532**(7599): p. 398-401.
35. Sato, Y., et al., *Structural basis for specific cleavage of Lys 63-linked polyubiquitin chains*. Nature, 2008. **455**(7211): p. 358-62.
36. de la Pena, A.H., et al., *Substrate-engaged 26S proteasome structures reveal mechanisms for ATP-hydrolysis-driven translocation*. Science, 2018. **362**(6418).
37. Dong, Y., et al., *Cryo-EM structures and dynamics of substrate-engaged human 26S proteasome*. Nature, 2019. **565**(7737): p. 49-55.
38. Ji, Z., et al., *Translocation of polyubiquitinated protein substrates by the hexameric Cdc48 ATPase*. Mol Cell, 2022. **82**(3): p. 570-584 e8.
39. Twomey, E.C., et al., *Substrate processing by the Cdc48 ATPase complex is initiated by ubiquitin unfolding*. Science, 2019. **365**(6452).
40. Zhang, S., et al., *USP14-regulated allostery of the human proteasome by time-resolved cryo-EM*. Nature, 2022. **605**(7910): p. 567-574.
41. Zheng, N. and N. Shabek, *Ubiquitin Ligases: Structure, Function, and Regulation*. Annu Rev Biochem, 2017. **86**: p. 129-157.
42. Horn-Ghetko, D. and B.A. Schulman, *New classes of E3 ligases illuminated by chemical probes*. Curr Opin Struct Biol, 2022. **73**: p. 102341.

43. Metzger, M.B., et al., *RING-type E3 ligases: master manipulators of E2 ubiquitin-conjugating enzymes and ubiquitination*. *Biochim Biophys Acta*, 2014. **1843**(1): p. 47-60.
44. Dou, H., et al., *BIRC7-E2 ubiquitin conjugate structure reveals the mechanism of ubiquitin transfer by a RING dimer*. *Nat Struct Mol Biol*, 2012. **19**(9): p. 876-83.
45. Plechanovova, A., et al., *Structure of a RING E3 ligase and ubiquitin-loaded E2 primed for catalysis*. *Nature*, 2012. **489**(7414): p. 115-20.
46. Pruneda, J.N., et al., *Structure of an E3:E2~Ub complex reveals an allosteric mechanism shared among RING/U-box ligases*. *Mol Cell*, 2012. **47**(6): p. 933-42.
47. Buetow, L., et al., *Activation of a primed RING E3-E2-ubiquitin complex by non-covalent ubiquitin*. *Mol Cell*, 2015. **58**(2): p. 297-310.
48. Dou, H., et al., *Essentiality of a non-RING element in priming donor ubiquitin for catalysis by a monomeric E3*. *Nat Struct Mol Biol*, 2013. **20**(8): p. 982-986.
49. Metzger, M.B., et al., *A structurally unique E2-binding domain activates ubiquitination by the ERAD E2, Ubc7p, through multiple mechanisms*. *Mol Cell*, 2013. **50**(4): p. 516-27.
50. Brown, N.G., et al., *Dual RING E3 Architectures Regulate Multiubiquitination and Ubiquitin Chain Elongation by APC/C*. *Cell*, 2016. **165**(6): p. 1440-1453.
51. Kiss, L., et al., *A tri-ionic anchor mechanism drives Ube2N-specific recruitment and K63-chain ubiquitination in TRIM ligases*. *Nat Commun*, 2019. **10**(1): p. 4502.
52. Nakasone, M.A., et al., *Structure of UBE2K-Ub/E3/polyUb reveals mechanisms of K48-linked Ub chain extension*. *Nat Chem Biol*, 2022. **18**(4): p. 422-431.
53. Pan, M., et al., *Structural insights into Ubr1-mediated N-degron polyubiquitination*. *Nature*, 2021. **600**(7888): p. 334-338.
54. Kamadurai, H.B., et al., *Insights into ubiquitin transfer cascades from a structure of a UbcH5B approximately ubiquitin-HECT(NEDD4L) complex*. *Mol Cell*, 2009. **36**(6): p. 1095-102.
55. Hunkeler, M., et al., *Solenoid architecture of HUWE1 contributes to ligase activity and substrate recognition*. *Mol Cell*, 2021. **81**(17): p. 3468-3480 e7.
56. Walden, H. and K. Rittinger, *RBR ligase-mediated ubiquitin transfer: a tale with many twists and turns*. *Nat Struct Mol Biol*, 2018. **25**(6): p. 440-445.
57. Harper, J.W. and B.A. Schulman, *Cullin-RING Ubiquitin Ligase Regulatory Circuits: A Quarter Century Beyond the F-Box Hypothesis*. *Annu Rev Biochem*, 2021. **90**: p. 403-429.
58. Horn-Ghetko, D., et al., *Ubiquitin ligation to F-box protein targets by SCF-RBR E3-E3 super-assembly*. *Nature*, 2021. **590**(7847): p. 671-676.
59. Kostrhon, S., et al., *CUL5-ARIH2 E3-E3 ubiquitin ligase structure reveals cullin-specific NEDD8 activation*. *Nat Chem Biol*, 2021. **17**(10): p. 1075-1083.
60. Hopf, L.V.M., et al., *Structure of CRL7FBXW8 reveals coupling with CUL1-RBX1/ROC1 for multi-cullin-RING E3-catalyzed ubiquitin ligation*. *Nature Structural and Molecular Biology*, 2022.
61. Bachmair, A. and A. Varshavsky, *The degradation signal in a short-lived protein*. *Cell*, 1989. **56**(6): p. 1019-32.
62. Varshavsky, A., *N-degron and C-degron pathways of protein degradation*. *Proc Natl Acad Sci U S A*, 2019. **116**(2): p. 358-366.
63. Timms, R.T. and I. Koren, *Tying up loose ends: the N-degron and C-degron pathways of protein degradation*. *Biochem Soc Trans*, 2020. **48**(4): p. 1557-1567.

64. Chiang, H.L. and R. Schekman, *Regulated import and degradation of a cytosolic protein in the yeast vacuole*. *Nature*, 1991. **350**(6316): p. 313-8.
65. Regelman, J., et al., *Catabolite Degradation of Fructose-1,6-bisphosphatase in the Yeast Saccharomyces cerevisiae: A Genome-wide Screen Identifies Eight Novel GID Genes and Indicates the Existence of Two Degradation Pathways*. *Molecular Biology of the Cell*, 2003. **14**: p. 1652-1663.
66. Giardina, B.J., D. Dunton, and H.L. Chiang, *Vid28 protein is required for the association of vacuole import and degradation (Vid) vesicles with actin patches and the retention of Vid vesicle proteins in the intracellular fraction*. *J Biol Chem*, 2013. **288**(17): p. 11636-48.
67. Menssen, R., et al., *Exploring the topology of the Gid complex, the E3 ubiquitin ligase involved in catabolite-induced degradation of gluconeogenic enzymes*. *J Biol Chem*, 2012. **287**(30): p. 25602-14.
68. Santt, O., et al., *The Yeast GID Complex, a Novel Ubiquitin Ligase (E3) Involved in the Regulation of Carbohydrate Metabolism*. *Molecular Biology of the Cell*, 2008. **19**: p. 3323–3333.
69. Braun, B., et al., *Gid9, a second RING finger protein contributes to the ubiquitin ligase activity of the Gid complex required for catabolite degradation*. *FEBS Lett*, 2011. **585**(24): p. 3856-61.
70. Karayel, O., et al., *DIA-based systems biology approach unveils E3 ubiquitin ligase-dependent responses to a metabolic shift*. *Proc Natl Acad Sci U S A*, 2020. **117**(51): p. 32806-32815.
71. Kong, K.E., et al., *Timer-based proteomic profiling of the ubiquitin-proteasome system reveals a substrate receptor of the GID ubiquitin ligase*. *Mol Cell*, 2021. **81**(11): p. 2460-2476 e11.
72. Langlois, C.R., et al., *A GID E3 ligase assembly ubiquitinates an Rsp5 E3 adaptor and regulates plasma membrane transporters*. *bioRxiv*, 2021.
73. Melnykov, A., S.J. Chen, and A. Varshavsky, *Gid10 as an alternative N-recognin of the Pro/N-degron pathway*. *Proc Natl Acad Sci U S A*, 2019. **116**(32): p. 15914-15923.
74. Qiao, S., et al., *Interconversion between Anticipatory and Active GID E3 Ubiquitin Ligase Conformations via Metabolically Driven Substrate Receptor Assembly*. *Mol Cell*, 2020. **77**(1): p. 150-163 e9.
75. Francis, O., F. Han, and J.C. Adams, *Molecular phylogeny of a RING E3 ubiquitin ligase, conserved in eukaryotic cells and dominated by homologous components, the muskelin/RanBPM/CTLH complex*. *PLoS One*, 2013. **8**(10): p. e75217.
76. Kobayashi, N., et al., *RanBPM, Muskelin, p48EMLP, p44CTLH, and the armadillo-repeat proteins ARMC8alpha and ARMC8beta are components of the CTLH complex*. *Gene*, 2007. **396**(2): p. 236-47.
77. Lampert, F., et al., *The multi-subunit GID/CTLH E3 ubiquitin ligase promotes cell proliferation and targets the transcription factor Hbp1 for degradation*. *Elife*, 2018. **7**.
78. Maitland, M.E.R., et al., *Structural and Functional Insights into GID/CTLH E3 Ligase Complexes*. *Int J Mol Sci*, 2022. **23**(11).
79. Chen, S.J., et al., *An N-end rule pathway that recognizes proline and destroys gluconeogenic enzymes*. *Science*, 2017. **355**(6323).
80. Langlois, C.R., et al., *A GID E3 ligase assembly ubiquitinates an Rsp5 E3 adaptor and regulates plasma membrane transporters*. *EMBO Rep*, 2022. **23**(6): p. e53835.
81. Chrustowicz, J., et al., *Multifaceted N-degron recognition and ubiquitylation by GID/CTLH E3 ligases*. *J Mol Biol*, 2021: p. 167347.

82. Shin, J.S., et al., *Crystal structure of yeast Gid10 in complex with Pro/N-degron*. *Biochem Biophys Res Commun*, 2021. **582**: p. 86-92.
83. Dong, C., et al., *Recognition of nonproline N-terminal residues by the Pro/N-degron pathway*. *Proc Natl Acad Sci U S A*, 2020. **117**(25): p. 14158-14167.
84. Dong, C., et al., *Molecular basis of GID4-mediated recognition of degrons for the Pro/N-end rule pathway*. *Nat Chem Biol*, 2018. **14**(5): p. 466-473.
85. Zavortink, M., et al., *The E2 Marie Kondo and the CTLH E3 ligase clear deposited RNA binding proteins during the maternal-to-zygotic transition*. *eLife*, 2020.
86. Mohamed, W.I., et al., *The human GID complex engages two independent modules for substrate recruitment*. *EMBO Rep*, 2021. **22**(11): p. e52981.
87. Schüle, T., et al., *Ubc8p functions in catabolite degradation of fructose-1,6-bisphosphatase in yeast*. *The EMBO Journal*, 2000. **19**(10): p. 2161-2167.
88. Kaiser, P., et al., *A human ubiquitin-conjugating enzyme homologous to yeast UBC8*. *J Biol Chem*, 1994. **269**(12): p. 8797-802.
89. Maitland, M.E.R., et al., *The mammalian CTLH complex is an E3 ubiquitin ligase that targets its subunit muskelin for degradation*. *Sci Rep*, 2019. **9**(1): p. 9864.
90. Kiedziarska, A., et al., *Structural similarities and functional diversity of eukaryotic discoidin-like domains*. *Biochim Biophys Acta*, 2007. **1774**(9): p. 1069-78.
91. Hosono, K., et al., *YPEL5 protein of the YPEL gene family is involved in the cell cycle progression by interacting with two distinct proteins RanBPM and RanBP10*. *Genomics*, 2010. **96**(2): p. 102-11.
92. Qiao, S., et al., *Cryo-EM structures of Gid12-bound GID E3 reveal steric blockade as a mechanism inhibiting substrate ubiquitylation*. *Nat Commun*, 2022. **13**(1): p. 3041.
93. Mattiazzi Usaj, M., et al., *Systematic genetics and single-cell imaging reveal widespread morphological pleiotropy and cell-to-cell variability*. *Mol Syst Biol*, 2020. **16**(2): p. e9243.
94. Menssen, R., K. Bui, and D.H. Wolf, *Regulation of the Gid ubiquitin ligase recognition subunit Gid4*. *FEBS Lett*, 2018. **592**(19): p. 3286-3294.
95. Hung, G.C., et al., *Degradation of the gluconeogenic enzymes fructose-1,6-bisphosphatase and malate dehydrogenase is mediated by distinct proteolytic pathways and signaling events*. *J Biol Chem*, 2004. **279**(47): p. 49138-50.
96. Chen, S.J., et al., *Aminopeptidases trim Xaa-Pro proteins, initiating their degradation by the Pro/N-degron pathway*. *Proc Natl Acad Sci U S A*, 2021. **118**(43).
97. Barbin, L., et al., *The Cdc48-Ufd1-Npl4 complex is central in ubiquitin-proteasome triggered catabolite degradation of fructose-1,6-bisphosphatase*. *Biochem Biophys Res Commun*, 2010. **394**(2): p. 335-41.
98. Liu, H., et al., *The GID ubiquitin ligase complex is a regulator of AMPK activity and organismal lifespan*. *Autophagy*, 2020. **16**(9): p. 1618-1634.
99. Zhen, R., et al., *Wdr26 regulates nuclear condensation in developing erythroblasts*. *Blood*, 2020. **135**.
100. Palavicini, J.P., et al., *RanBP9 Plays a Critical Role in Neonatal Brain Development in Mice*. *PLoS One*, 2013. **8**(6): p. e66908.
101. Pfirrmann, T., et al., *RMND5 from Xenopus laevis is an E3 ubiquitin-ligase and functions in early embryonic forebrain development*. *PLoS One*, 2015. **10**(3): p. e0120342.
102. Skraban, C.M., et al., *WDR26 Haploinsufficiency Causes a Recognizable Syndrome of Intellectual Disability, Seizures, Abnormal Gait, and Distinctive Facial Features*. *Am J Hum Genet*, 2017. **101**(1): p. 139-148.

103. Soni, S., et al., *Absence of erythroblast macrophage protein (Emp) leads to failure of erythroblast nuclear extrusion*. J Biol Chem, 2006. **281**(29): p. 20181-9.
104. Wei, Q., et al., *Maea expressed by macrophages, but not erythroblasts, maintains postnatal murine bone marrow erythroblastic islands*. Blood, 2019. **133**(11): p. 1222-1232.
105. Salemi, L.M., et al., *Cell signalling pathway regulation by RanBPM: molecular insights and disease implications*. Open Biol, 2017. **7**(6).
106. Umeda, M., H. Nishitani, and T. Nishimoto, *A novel nuclear protein, Twa1, and Muskelein comprise a complex with RanBPM*. Gene, 2003. **303**: p. 47-54.
107. Goto, T., et al., *WDR26 is a new partner of Axin1 in the canonical Wnt signaling pathway*. FEBS Lett, 2016. **590**(9): p. 1291-303.
108. Lu, Y., et al., *Twa1/Gid8 is a beta-catenin nuclear retention factor in Wnt signaling and colorectal tumorigenesis*. Cell Res, 2017. **27**(12): p. 1422-1440.
109. Cao, W.X., et al., *Precise Temporal Regulation of Post-transcriptional Repressors Is Required for an Orderly Drosophila Maternal-to-Zygotic Transition*. Cell Rep, 2020. **31**(12): p. 107783.
110. Yuan, S., et al., *A ubiquitin ligase of symbiosis receptor kinase involved in nodule organogenesis*. Plant Physiol, 2012. **160**(1): p. 106-17.
111. Sherpa, D., et al., *GID E3 ligase supramolecular chelate assembly configures multipronged ubiquitin targeting of an oligomeric metabolic enzyme*. Mol Cell, 2021. **81**(11): p. 2445-2459 e13.
112. Delto, C.F., et al., *The LisH motif of muskelein is crucial for oligomerization and governs intracellular localization*. Structure, 2015. **23**(2): p. 364-73.
113. Sherpa, D., et al., *Differential UBE2H-CTLH E2-E3 ubiquitylation modules regulate erythroid maturation*. eLife, 2022.
114. Kaiser, S.E., et al., *Protein standard absolute quantification (PSAQ) method for the measurement of cellular ubiquitin pools*. Nature Methods, 2011. **8**: p. 691.
115. Varshavsky, A., *Ubiquitin fusion technique and related methods*. Methods Enzymol, 2005. **399**: p. 777-99.
116. Mastronarde, D., *SerialEM: A Program for Automated Tilt Series Acquisition on Tecnai Microscopes Using Prediction of Specimen Position*. Microscopy and Microanalysis, 2003. **9**(S02): p. 1182-1183.
117. Biyani, N., et al., *Focus: The interface between data collection and data processing in cryo-EM*. J Struct Biol, 2017. **198**(2): p. 124-133.
118. Fernandez-Leiro, R. and S.H.W. Scheres, *A pipeline approach to single-particle processing in RELION*. Acta Crystallogr D Struct Biol, 2017. **73**(Pt 6): p. 496-502.
119. Scheres, S.H., *RELION: implementation of a Bayesian approach to cryo-EM structure determination*. J Struct Biol, 2012. **180**(3): p. 519-30.
120. Zivanov, J., et al., *New tools for automated high-resolution cryo-EM structure determination in RELION-3*. Elife, 2018. **7**.

“In the loving memory of my dearest papa and Furba-Tashi.”